TÉCNICO LISBOA

Effect of Cerenkov Polarization in the Cosmic Rays charge reconstruction

Charge reconstruction with RICH/AMS-02 data

Bruno Eduardo Cruz Santos
(Licenciado)

Dissertação para obter o grau de Mestre em

Engenharia Física Tecnológica

Júri

Presidente: Prof. Doutora Maria Teresa Haderer de la Pena Stadler
Orientador: Prof. Doutor Fernando José de Carvalho Barão
Vogal: Doutora Maria Luísa Ferreira da Gama Velho Arruda
Vogal: Prof. Doutor João Carlos Carvalho de Sá Seixas

Novembro 2013

Anyone who has never made a mistake has never tried anything new.

Albert Einstein

Acknowledgments

Abstract

The RICH detector is part of the cosmic-ray Alpha Magnetic Spectometer (AMS) experiment that is installed in the International Space Station since May 2011. It is composed of a radiator material on the top of the detector and a matrix of pixelized photomultipliers coupled to light guides on the bottom. The light tightness of the detector is provided by surrounding conical mirror. A charged particle crossing the radiator will radiate a number of cerenkov photons proportional to the particle charge squared. The RICH detector is aiming to measure with very high accuracy both the velocity (roughly one per mil for singly charged particles) and the charge of particles up to the iron nuclei. The charge measurement accuracy depends strongly on systematic effects that grow with the element charge squared. In order to have a good nuclei identification up to iron, all factors contributing to evaluate the radiated signal have to be identified and taken into account. The Cherenkov electromagnetic radiation is of polarized nature. The photon path from radiation point to detection includes three interfaces: the radiator-air, the mirror-air and the ligh-guide. The transmission efficiency depends on the photon polarization. Therefore, the effect of the polarization has to evaluated for both radiator materials, aerogel and sodium fluoride and compared to the currently one implemented in the charge reconstruction algorithms developped by the LIP group. The correction has to be implemented in the charge reconstruction efficiency used on data reconstruction and its implication on the charge measurement accuracy will be evaluated with AMS nuclei reconstructed data.

Keywords

Charge reconstruction, AMS-02, RICH, Cherenkov photon polarization.

Resumo

O detector RICH faz parte da experiência de raios cósmicos AMS que está instalada na ISS desde Maio de 2011. É, por sua vez, constituído por um material radiator no topo e uma de PMT pixelizados acoplados a guias de luz no fundo. O constrangimento da luz no detector resulta dum espelho cónico que o circunda. Uma partícula carregada que atravessa o radiator vai radiar um número de fotões proporcional ao quadrado da carga. Por sua vez, um dos principais objectivos do detector RICH é medir com alta precisão a velocidade (sensivelmente 1/1000 por cada partícula carregada) e a carga das partículas até ao núcleos de ferro. A precisão na medição está fortemente correlacionada com os efeitos sistemáticos que crescem com o quadrado da carga. Portanto, de forma a obter uma boa identificação de carga até ao ferro, será necessário avaliar o sinal deixado pela partícula e inditificar a mesma de acordo com a medida obtida. A radiação de Cherenkov é uma onda electromagnética naturalmente polarizada. Na sua propagação pelo detector, cada fotão de Cherenkov atravessa três interfaces antes de ser detectado: radiador/ar, espelho/ar e guias de luz. A eficiência de transmissão dependerá da polarização. Deste modo, o efeito da polarização tem de ser avaliado para ambos os tipos de radiator (NaF/aerogel) e comparar com o factor resultante da actual implementação do algorítmo de reconstrução de carga desenvolvido pelo grupo do LIP. Portanto, a correção será implementado nos dados da reconstrução e estudado a a implicação na medição de carga com os dados reconstruídos de AMS.

Palavras Chave

Reconstrução de carga, AMS-02, RICH, Polarização de Cherenkov.

Contents

List of Figures

List of Tables

Abbreviations

CR Cosmic Rays

CK Cherenkov

AMS Alpha Magnetic Spectrometer

ISS International Space Station

RICH Ring Imaging Cherenkov

PMT Photomultiplier tube

ECAL Electromagnetic Calorimeter

LG Light-guide

LIP Laboratório de Instrumentação e Física de Partículas

List of Symbols

1

Introduction

Contents

1.1 Motivation

The study of CR began approximately in 1900, as a result of the observation of ionisation in gases contained in closed vessels. In order to find some evidences, balloon flights were undertaken. Such studies, lead by Victor Hess in 1912, allowed to discover that, instead of decreasing, the ionization of the air strongly increases with altitude.
This marked the discovery of CR, for which Hess received the Nobel Prize in 1936.
In the following thirty years, cosmic ray research concentrated on the high-energy properties of cosmic radiation. CR were the predecessors of the accelerators as the source of high energy particles.
As a result, CR provided a unique tool to study the most energetic particles in the Universe. For instance, the muon (1947), the positron (1932) and particles cointaining strange quarks were first discovered in cosmic-ray induced reactions[2].
However, the growing interest in particle accelarators, since the middle of twentieth century, lead CR scientists to direct their attention to accelarator labs.

Figure 1.1: International Space Station.

However, during the last decade an intensive experimental program has been es-

tablished and will keep on taking place in forthcoming years motivated by the study of issues like the origin of dark matter, CR propagation through the galaxy and the study of elementary nuclei (e.g. B, C, He).
The interest in CR is beyond the simple knowledge of experimental particle physics, since this is a threefold field that also embraces astrophysics and theoretical physics. In fact, the energy range acceptance of balloon-borne and satellite experiments is comparable to that reached by the most recent accelerators. For example, the LHC is reaching energies of 650GeV, while the big CR ground detectors are measuring particles within energy above 10^{11}GeV.

1.2 Thesis Outline

In the first part of this thesis the AMS-02 RICH detector efficiency and the charge reconstruction method are described. The second part is devoted to the characterization of a new effect in the RICH charge reconstruction: CK polarization.

2

Cosmic-Ray detection with AMS-02

Contents

2.1 Introduction to Cosmic-Rays

CR are evaluated by the integral intensity *I*, which regards the number of particles with energy over *E* crossing an unit area per unit time and unit solid angle. Hence its units are $[I] = cm^{-2}s^{-1}sr^{-1}$.
The cosmic ray spectrum can be described by

$$I(E) = \frac{dN}{dE} \propto E^{-\alpha} \tag{2.1}$$

in the energy range from a few *GeV* to 100 *TeV*.
Figure 2.1 shows *I(E)* regarding several important elements. It also follows immediately that the main component component of CR are protons ($\sim 90\%$), with additionally around 10 % of helium and smaller admixture of heavier elements. In addition, this figure allows to consider a few GeV power-laws to describe CR spectra. Therefore the total cosmic ray spectrum is given by

$$I(E) \sim 1.8E^{-\alpha}\frac{particles}{cm^2 ssr GeV} \tag{2.2}$$

where around 10^{15} eV (the *knee*), the slope range goes from $\alpha \simeq 2.7$ to $\alpha \simeq 3.0$.
Figure 2.1 shows cosmic ray spectrum combined with the power-law form function. In further detail, it regards several experiments according to the energy range as follows:

- *LEAP*: $10^9 \leq E \leq 10^{11}$ eV
- *PROTON*: $10^{12} \leq E \leq 10^{14}$ eV
- *Akeno*: $10^{15} \leq E \leq 10^{17}$ eV
- *HiRes*: $10^{18} \leq E \leq 10^{20}$ eV

Conclusively, CR experiments are divided by two main categories (see figure 2.2),

- Air-shower detection : $10^{14} \leq E \leq 10^{18}$eV/nucleon;
- Low and intermediate energy detection: $E \leq 10^{13}$ eV/nucleon (e.g. AMS-02).

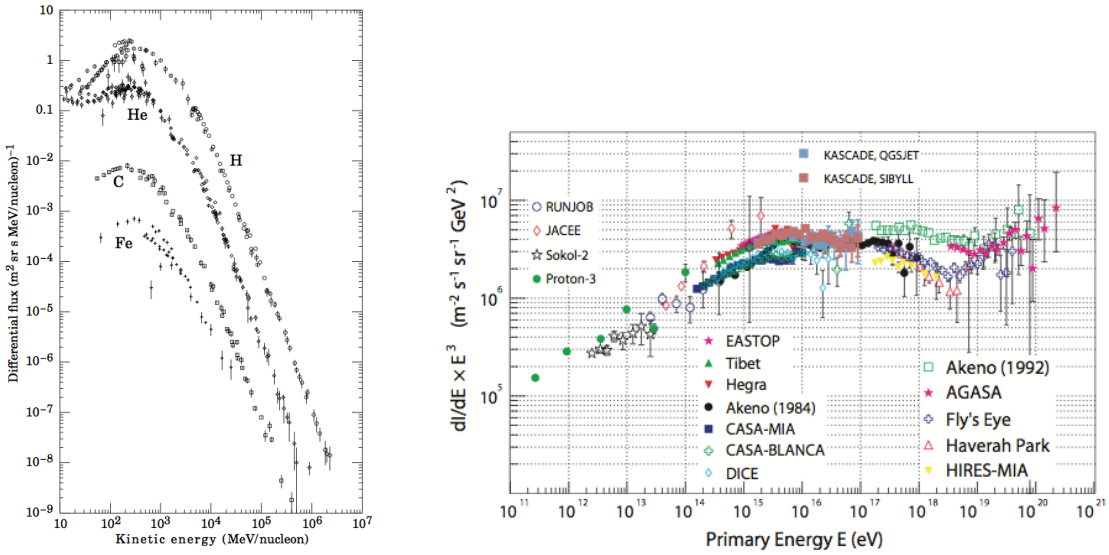

(a) **(b)**

Figure 2.1: a) Cosmic rays intensity for several elements. b) The cosmic ray spectrum *I(E)* as function of kinetic energy *E*, compiled using results from the LEAP, PROTON, Akeno, and HiRes experiments[4].

2.2 AMS-02: detector principles and scientific goals

In the previous section 2.1 it was described different experiments according to the energy range detection. Although, in this thesis the main focus will be AMS-02 *, meaning that the energy spectra will be from* $\sim GeV$ *to* $\sim TeV$*. Hence, in this section will include the following topics:*

- *Scientific goals;*
- *Detector principles.*

2.2.1 AMS-02 Scientific Goals

The AMS-02 experiment aims to accomplish the following physics goals:

- Detection of charged cosmic-ray particles within a rigidity region between $\sim$0.5 GeV and $\sim$2 TeV and photons with energies up to a few hundred GeV;
- Search for heavy antinuclei (Z$\geq$2), if eventually discovered would be an evidence of cosmological antimatter;
- Evaluation of possible dark matter signatures in cosmic ray spectra, using indirect signals such as annihilation products of neutralino.

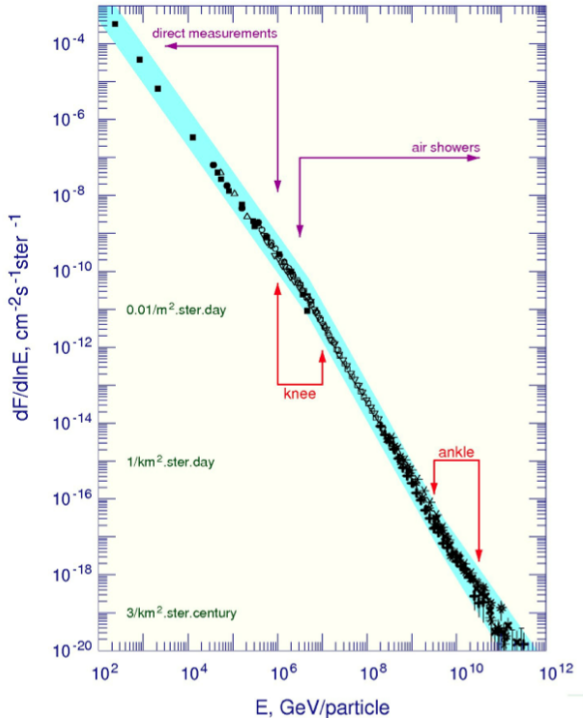

Figure 2.2: Cosmic Ray Energy Spectrum[4].

2.2.2 Detector Description

The AMS-02 detector is the first large magnetic spectrometer in space, and it is able to measure, with high accuracy, the cosmic ray flux above the Earth's atmosphere. Adding to this, AMS-02 has an unprecedented precision in detection and identification of cosmic rays coupled with state-of-art particle identification techniques. The spectrometer is composed of several subdetectors[8]:

- a Transition Radiation Detector (TRD)
- a Time-of-Flight (TOF) detector
- a Silicon Tracker
- a set of Anticoincidence Counters (ACC)
- a Ring Imaging Cherenkov (RICH) detector
- an Electromagnetic Calorimeter (ECAL).

The permanent magnet

TheAMS-02 is a cylinder with a diameter of 1m and a height of 1m, made of 6000 Neodimium-Iron-Boron blocks. It creates a magnetic field of 0.15 T (bending power

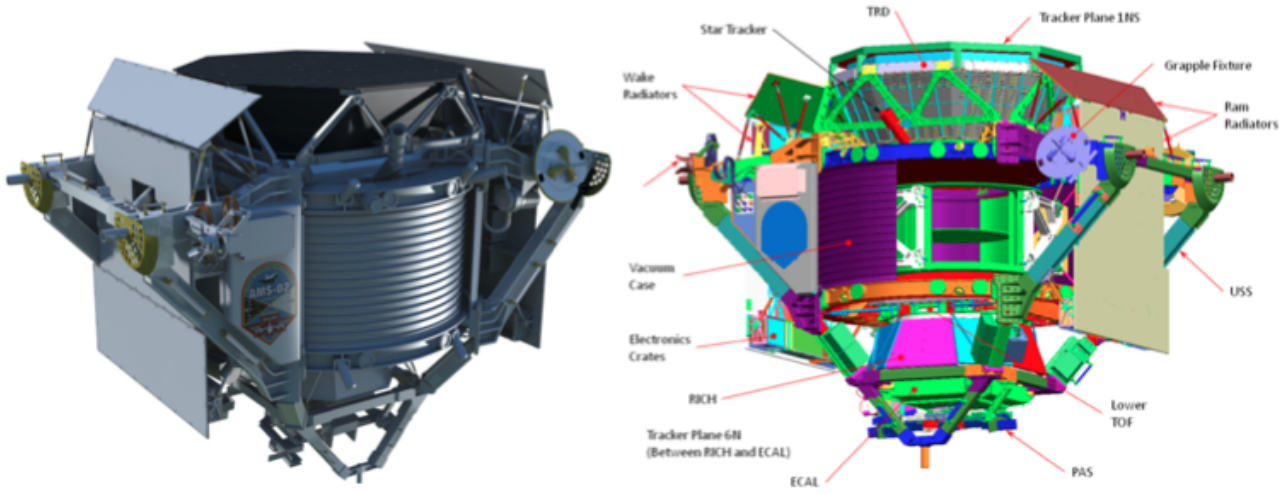

Figure 2.3: The AMS-02 detector.

is
BL^2 =0.15 Tm^2), uniform along the x axis, and with negligible dipole moment.

Transition Radiation Detector (TRD)

The TRD is the first sub-detector that most particles face when entering in AMS-02 detector. The basic working principle of TRD consists in radiation emission when charged particles cross the boundary between two media with different dielectric constants: ϵ_1, ϵ_2.
In particular, TRD detects electromagnetic radiation in the X-ray energy region (1-50 KeV). Transition radiation is proportional to the relativistic γ-factor (γ =E/m) and it has a typical thereshold of $\gamma \sim 500$, ensuring that light particles such as positrons have a much higher probability of emitting transition radiation than heavy particles such as protons.
As a result, the TRD allows a separation between low and high mass particles (for a proton with momentum range of 10-300 GeV, the rejection factor is $10^2 - 10^3$).
Although the emission probability at a single interface is very small ($\sim 10^{-2}$), this can be enhanced by a multilayer structure, which implies multiple transitions.
The AMS-02 TRD consits of 328 modules made of a fleece radiator 20mm thick and straw tube proportional wire chambers filled with a Xe/CO_2 (80%:20%) mixture.

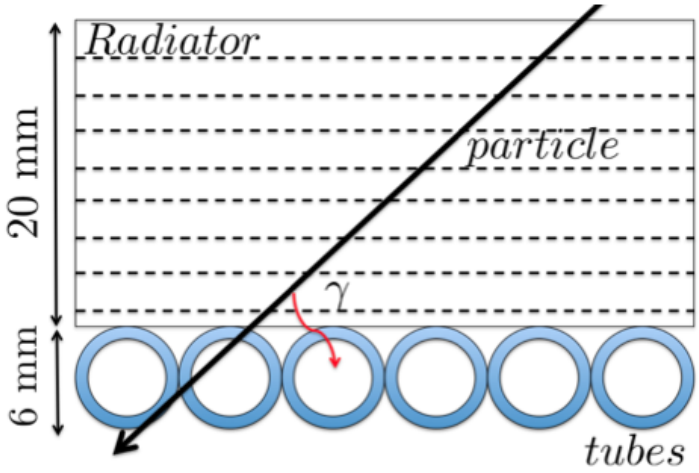

Figure 2.4: TRD module.

Time-of-Flight (TOF)

The TOF system is the subdetector that provides the fast trigger for charged particles, developing an efficient distinction between upward and downward particles through the measurement of particle velocity β ($\sigma_\beta = 3\%$ for protons) and absolute charge estimate up to $Z \simeq 20$.
The TOF system consists of four planes with 8, 8, 10, 8 plastic scintillator counters each.The planes are roughly circular with 12 cm wide scintillator paddles, one pair of planes above the magnet called the upper TOF and the other below the magnet TOF, called the lower TOF. The quality of measurements is increased by having perpendicular paddle orientations in both pairs of planes.

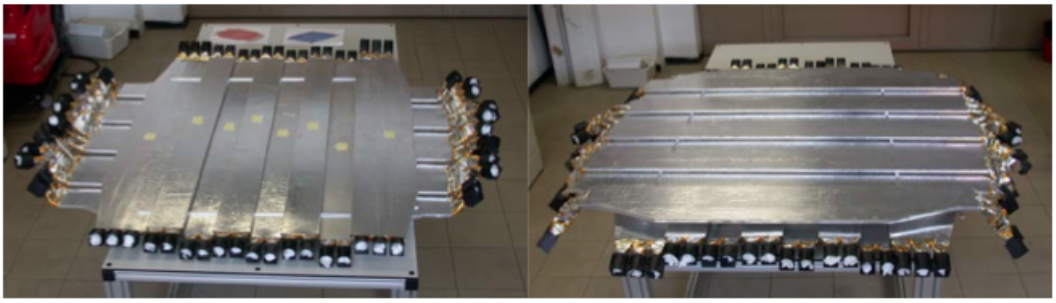

Figure 2.5: TOF planes.

Silicon Tracker

The Silicon Tracker is the AMS-02 detector designed to make measurements of particle positions with a precision of $\sim$10μm along the bending plane (*yOz*) and $\sim$30μm on the transverse direction. The evaluation of the particle trajectory inside

magnetic cavity is a key point to calculate the particle rigidity with a precision of 2% at few GV (the maximal detectable rigidity is around 3 TV). The silicon tracker is also capable of measuring the charge of particles up to $Z \simeq 26$.
The tracking system is composed of 9 layers: 1 above the TRD, 1 above the ECAL, and other set of 7 in the central region (inner tracker). The layers are made of $\sim$ 2500 double-sided silicon microstrip sensors arranged on 192 ladders.

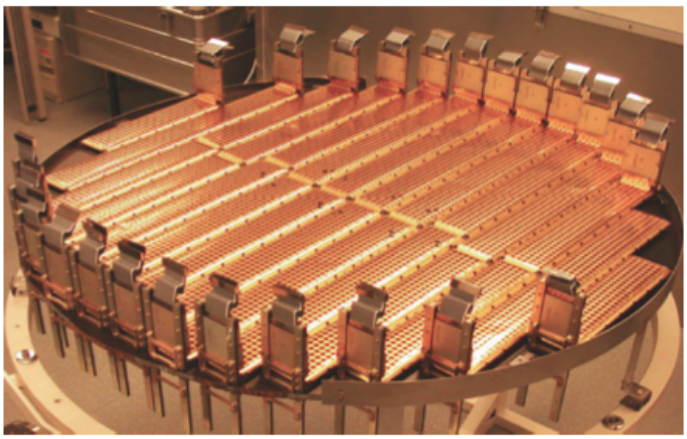

Figure 2.6: Tracker plane.

The Anti-Coincidence Counters (ACC)

The AMS-02 ACC are made of scintillators, surrounding the silicon tracker and fitted tightly inside the inner bore of the detector's magnet. The ACC detects particles that enter the tracker laterally, beyond the AMS acceptance, which may create misleading signals in the event reconstruction.

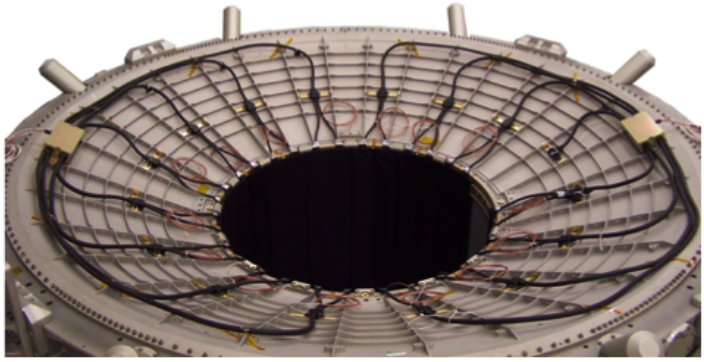

Figure 2.7: ACC top view.

The Ring Imaging Cherenkov detector (RICH)

The RICH is a proximity focusing device which is responsible for accurately measuring the velocity of charged particles that cross its radiator. The RICH/AMS-02 has

a dual configuration, a centred square of sodium fluoride (NaF) surround by aerogel tiles. When a charged particle wit a velocity greater than the light velocity in the medium, it emits a CK cone. The aperture of the cone (θ_c) depends on the velocity (β) and on the refractive index of the material. By collecting the signal of emitted photons, it is possible to evaluate the charge of the particle.
The RICH system also includes a conical mirror, light guides (LG) and a photon detection matrix composed of 680 PMTs.
A more detailed description of this subdetector is given in the next section.

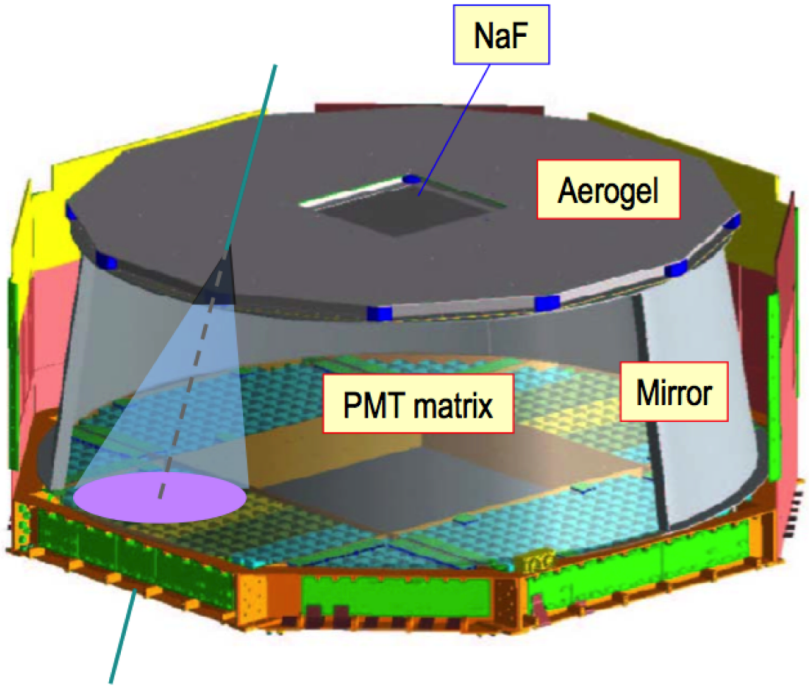

Figure 2.8: Sketch of the AMS-02 RICH: the radiator layer is placed on top of the conical mirror; below it the PMT matrix with the support structure is visible.

The Electromagnetic Calorimeter (ECAL)

The ECAL, located at the bottom of the AMS-02 detector, is a fine grained lead-scintillating fiber sampling calorimeter, with an active area of 648$\times$648 mm^2 and a thickness of 166.5 mm. It provides an accurate 3-D imaging of the longitudinal and lateral shower development. In addition, it works as a powerful tool to discriminate hadrons from electrons and positrons, since the profile of showers developed inside the detector is completely different.
Another key feature of ECAL is the capability of detecting gamma-rays, either by measuring the interaction of the photon inside the detector, or through the identification of particle-antiparticle pairs produced in the matter preceding it.

The AMICA Star Tracker

The Astro Mapper for Instrument Check of Attitude (AMICA) is composed by a pair of small optical telescopes instaled near the Silicon Tracker structure. Its main purpose is the measurement of detector orientation, allowing the identification of γ-ray sources.

2.3 RICH detector

*The **R**ing **I**maging **Ch**erenkov detector is based on photon emission by a charge particle (so-called Cherenkov effect). Thus RICH is able to measure cosmic-ray velocity β and charge Z. Furthermore, it is obtained a β measurement precision of 0.1% for $Z = 1$ and improving with the number of collected photoelectrons until the saturation limit (~ 0.01 $\%$).*
The RICH main goal is performing a cosmic ray charge separation at least up to the iron element ($Z = 26$).
In addition, the RICH will also provide the rejection of albedo particles, since they are not expected to generate a response from the counter.
In this section, the following topics will be approached:

- *CK radiation;*
- *RICH setup.*

2.3.1 Cherenkov radiation

When charged particles crossing a medium $n > 1$ with a velocity (*v*) beyond the speed of light in that medium (v_l=c/n, where *c* is the light speed in vacuum), they emit *CK radiation*. CK photons are produced uniformly (if *n* is constant) along the path and they are emitted at a fixed angle θ_c, considering the particle momentum direction as the reference axis. In addition, there is an azimuthal symmetry in CK radiation emission.
The *CK angle* θ_c is given by the following formula[3]:

$$\cos(\theta_c) = \frac{1}{n\beta} \tag{2.3}$$

Since the refractive index *n* is constant, the maximum CK angle value is reached for ultrarelativistic particles (i.e $\beta \simeq 1$)

$$\theta_c^{max} = acos\left(\frac{1}{n}\right) \tag{2.4}$$

On the opposite side, the lowest value for velocity is constraint by the condition $\cos(\theta_c) = 1$, which means that

$$\beta_{th} = \frac{1}{n} \tag{2.5}$$

where β_{th} is the threshold speed. Consequently, for different refractive indices there are different *thereshold* velocities and thereshold momenta as well as different maximum emission angles.

CK radiation effect spans a frequency range (ω) that includes the various Fourier

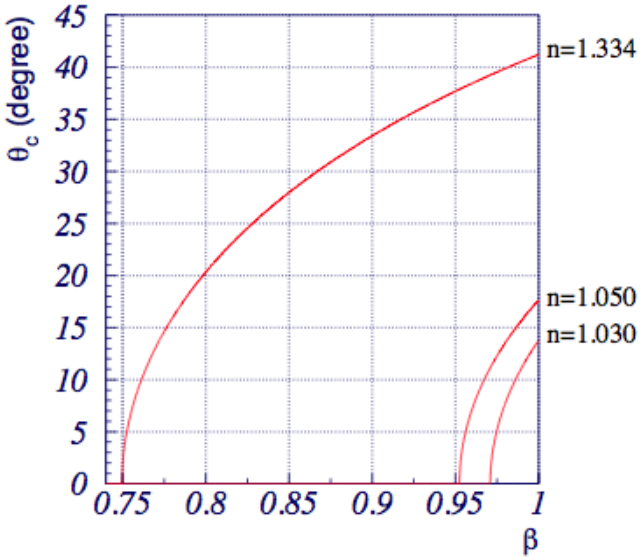

Figure 2.9: Dependence of the emission angle θ_c with the particle velocity (β) for two materials: aerogel($n = 1.050/1.030$) and NaF ($n = 1.334$).

components of the electromagnetic pulses ($\vec{k}$) emitted by polarized medium dipoles. This coherent light emission, with a cone shape, has a polarization vector in the plane defined by the charged particle direction and photon direction.

The energy transported by CK radiation *E* per unit of length *dx* and range frequency ($d\omega$) for a particle of charge Ze was calculated by Frank and Tamm, taking the form:

$$\frac{d^2E}{dxd\omega} = \frac{Z^2\alpha\hbar}{c}\left(1 - \frac{1}{\beta^2 n^2(\omega)}\right) = \frac{Z^2\alpha\hbar}{c}\omega\sin^2(\theta_c) \tag{2.6}$$

where $\alpha = \frac{e^2}{4\pi\epsilon_0 c} = 1/137.04$ is the fine structure constant. Due to chromatic dispersion of the optical medium, *n* is a function of the radiation frequency ω. The radiated energy grows proportionally to the frequency and the square of the electric charge.

For the purpose of a qualitative discussion about energy loss by CK effect, the Bethe-Bloch equation can be approximate given by

$$\frac{dE}{dx} \simeq \rho(2MeVcm^2/g)\frac{Z^2}{\beta^2} \tag{2.7}$$

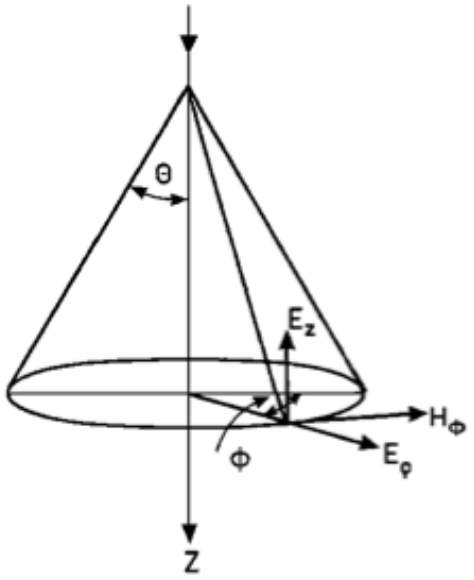

Figure 2.10: CK light polarization vectors. The electric field vector $\vec{E}$ lies in the plane defined by the particle direction and the photon direction[3].

For instance, for electrons with energy over 100 keV, velocity is close to the velocity of light ($\beta \simeq 1$), resulting in an energy loss by ionization about $2MeV/cm$ multiplied by density of the medium. On the other hand, the same particle loses about 5×10^{-4} MeV ($n = 1.334$) by CK effect (in the spectral range $\lambda = 400 - 700$ nm). This shows that there is a small amount of energy carried by CK radiation compared with other energy losses such as ionization.
The description of CK phenomena in the RICH has a strong dependence on the number of radiated CK photons used in the charge reconstruction, since the energy carried by each photon is

$$E_\gamma = \hbar\omega \tag{2.8}$$

it happens that the total number of radiated photons, N_γ^{rad}, is closely related with the total radiated energy, *E*, directly from the following expression

$$E = N_\gamma^{rad} E_\gamma \implies dE = dN_\gamma^{rad} E_\gamma \tag{2.9}$$

Introducing the expression (1.4) back into (1.7), the number of radiated photons per unit of length and range of frequency is described by:

$$\frac{d^2 N_\gamma^{rad}}{dx d\omega} = \frac{Z^2\alpha}{c}\left(1 - \frac{1}{\beta^2 n^2(\omega)}\right) \tag{2.10}$$

On other hand, the number of radiated photons per unit of length and energy is given by

$$\frac{d^2N_\gamma^{rad}}{dxdE_\gamma} = \overbrace{\frac{2\pi\alpha}{hc}}^{C} Z^2\left(1-\frac{1}{\beta^2n^2}\right) \tag{2.11}$$

Indeed, the expression (1.9) shows that light yield increases with radiator thickness (L), the squared particle charge (Z^2), the particle velocity (β) and the refractive index of the medium (*n*). The constant term *C* is $\sim 370cm^{-1}eV^{-1}$, which allows to write:

$$\frac{d^2N_\gamma^{rad}}{dxdE_\gamma} \simeq 370Z^2\left(1-\frac{1}{\beta^2n^2}\right)[cm^{-1}eV^{-1}] \tag{2.12}$$

The number of photons emitted per unit path and per unit energy interval is constant for a given charge *Z* and this quantity is a key feature in RICH detector design.
The total number of CK photons emitted in a radiator of thickness *L* is a result from (1.10) integration. Only a fraction number of photons is detected by the photodetectors, due to propagation from emission to detection point and to limited detector efficiency (quantum efficiency), that are accounted in overall efficiency (ϵ) evaluation. Hence, the number of photoelectrons per unit of length(cm) is

$$N_{p.e.} \simeq 370Z^2L < \sin^2(\theta) > \int \epsilon(E)dE = 370Z^2L < \sin^2(\theta) >< \epsilon > \Delta E \tag{2.13}$$

Conversely, the total number of radiated photons per unit of length in terms of the wavelength range is obtained using the following integration:

$$\frac{dN_\gamma^{rad}}{dx} = 2\pi\alpha Z^2\int_{\lambda_1}^{\lambda_2}\left(1-\frac{1}{\beta^2n^2(\lambda)}\right)\frac{d\lambda}{\lambda^2} \tag{2.14}$$

Consequently, the number of CK photons emitted per unit of wavelength interval $d\lambda$ is proportional to $d\lambda/\lambda^2$, which means that most of the photons are emitted in the UV region. In addition to this, the variation of $n(\lambda)$ is smooth in the same range,

$$\left\langle 1-\frac{1}{\beta^2n^2(\lambda)}\right\rangle =< 1-\cos^2(\theta_c) >=< \sin^2(\theta_c) > \tag{2.15}$$

The number of radiated photons per unit of length becomes

$$\frac{dN_\gamma^{rad}}{dx} = 2\pi\alpha Z^2 < \sin^2(\theta_c) > \left(\frac{1}{\lambda_1}-\frac{1}{\lambda_2}\right) \tag{2.16}$$

2.3.2 RICH setup

The RICH /AMS sub-detector is a proximity focusing device with a dual solid radiator configuration at the top made of 25 mm thick aerogel ($n = 1.050$) and 5 mm thick

sodium fluoride (NaF) tiles, whereas the latter is crossed by $\sim 11\%$ of the events. Moreover, the RICH has a high reflectivity mirror surrounding the whole set and a detection matrix with light guides and photomultiplier tubes (PMTs). The RICH has a truncated conical shape with a top radius of 60 cm, a bottom radius of 67 cm and a total expansion height of 47 cm. The total height of the detector is 60.5 cm.
The photodetector plane is made of an array of 680 PMTs, with a $64 \times 64\ cm^2$ central hole to minimize matter in front of electromagnetic calorimeter. In figure 2.12 a perspective and schematic view of the RICH detector with the corresponding dimensions is represented.
A charged particle crossing the dielectric material of the radiator with a velocity higher than the light speed in the medium emits a cone of CK photons. Afterwards, this light cone (the so called CK Cone) intersects the detection plane, drawing a ring as the one represented in figure 2.11.
The proximity focusing device is important due to the formation of a set of concentric Cherenkov rings resulting from the radiator thickness. Each CK ring corresponds to a different emission point located along the particle's path. This RICH focalisation system has a negligible error associated with emission point coordinates, since it has a small radiator thickness compared to the expansion height.

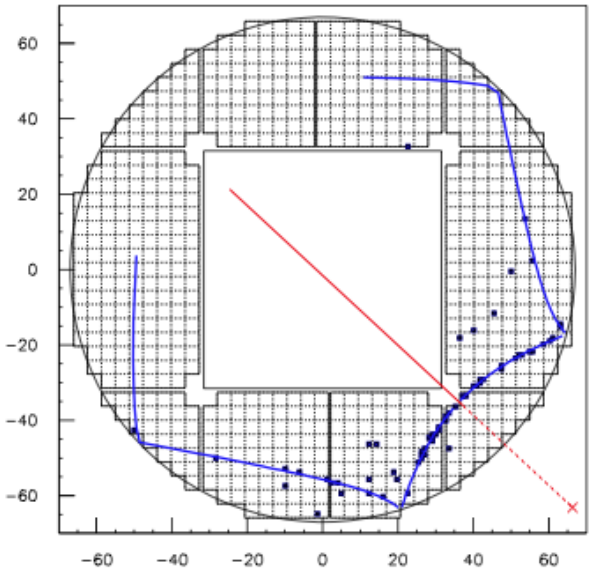

Figure 2.11: Beryllium event with $\beta \simeq 1$ generated in the NaF radiator and detected in the PMT matrix[3].

On other hand, there is an uncertainty on the CK angle, which is given by the sum in quadrature of all the possible sources of error.

The physical quantities required to find θ_c are:

- Particle direction (θ_p,ϕ_p)
- Photon detection coordinates on the photodetector surface
- Chromatic dispersion of the radiator

The particle direction is not measured by the RICH subdetector. Instead, the external tracker detector must provide the particle direction and impact point on the top of the radiator, thus precision of θ_p and ϕ_p depends on this detector's sensivity. On the other hand, photodetectors must have an accurate position measurement of CK ring, so that the global measurement is not compromised.
The last item, chromatic dispersion of the radiator, is an intrinsic source of uncertainty, since depends on detector properties:

$$\sigma(E) \propto \left(\frac{dn}{dE}\right)\Delta E \tag{2.17}$$

Consequently, this error can be reduced only by constraining the energy bandwidth, ΔE.

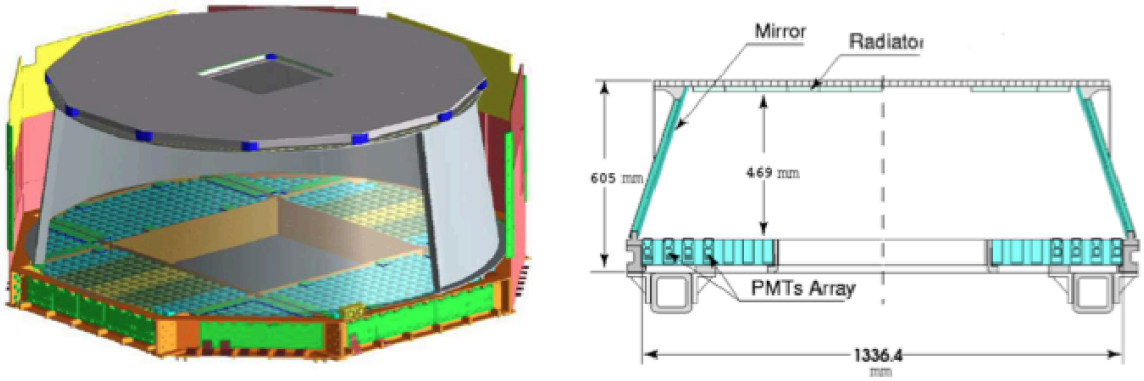

Figure 2.12: Perspective and side-view of the RICH detector[3].

2.3.2.A Radiator material

The radiator is a key component of any RICH detector, since the kinematic range and the velocity resolution strongly depend on its optical properties.
The chosen configuration for the AMS-02 RICH consists of a mixed radiator of silica aerogel and sodium fluoride (NaF). The set of radiator tiles (blocks of $11.4 \times 11.4 \times 2.5\ cm^3$ of aerogel and $8.5 \times 8.5 \times 0.5\ cm^3$ of NaF) covers the upper section of the

mirror, as shown in 2.13. The radiator blocks are supported by a plastic foil, covering a total surface of $\sim$11310 cm^2.

CK cones produced in the NaF radiator have a larger opening angle than those

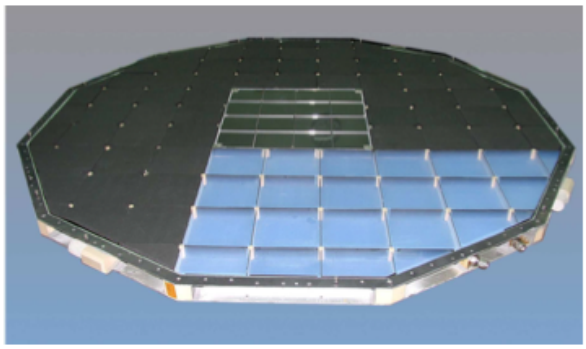

Figure 2.13: Radiator container with part of the tiles assembled[3].

produced in aerogel. Therefore this material is positioned in the central zone ($34 \times 34\ cm^2$), to enhance the reconstruction efficiency and to enlarge the kinematic range towards lower energies.

Sodium fluoride

Sodium fluoride is a crystal of refractive index 1.334, which means that the theresh-old for CK light emission is $\beta_{th} = 0.75$. Due to its high refractive index, the expected β resolution in the the AMS/RICH configuration is $\sigma(\beta) \simeq 3 \times 10^{-3}$, and has the ad-vantage of increase the kinematic range down to 1.1 GeV/c for protons/anti-protons. In addition, this crystal has two characteristics of great interest for CK detectores:

- The lowest refractive index of all common optical materials;
- High transparency to UV light.

Silica Aerogel

The material covering most of the acceptance of the AMS RICH radiator is a silica aerogel. Most gas radiators have refractive index lower than 1.0018 and liquid radiators have *n* higher than 1.27. Thus, the only material which can fill the gap between these values is silica aerogel, with a refractive index ranging from 1.004 to 1.1. The composition of aerogel is basically SiO_2 and air.
The relative amount of SiO_2 defines the final value of the refractive index. Hence, in order to get the desired refractive index it is only necessary to change its density

(ρ). The expression relating ρ (in g/cm^3) with the refractive index *n* of the resulting material is given by:

$$\rho = \frac{(n-1)}{0.28} \tag{2.18}$$

The aerogel radiator has optical properties such as granular structure (typically of

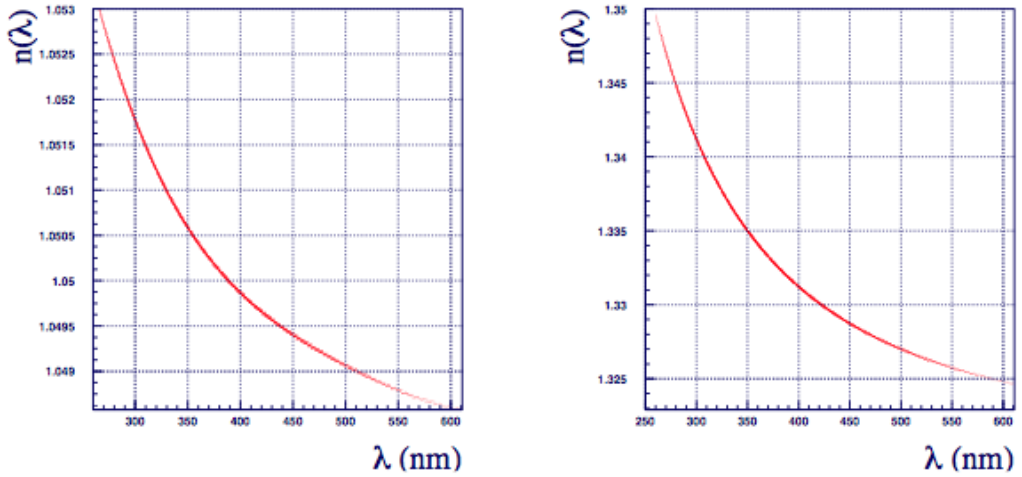

Figure 2.14: Chromatic dispersion, used in simulation, in the aerogel $n = 1.050$ radiator (left) and in the NaF radiator (right)[3].

few nanometres), which can disperse visible light through Rayleigh scattering phenomena. This is a drawback of aerogel for RICH detectors, since it leads to a loss in the directionality of part of the CK photons produced. The transmittance of an aerogel sample is described by,

$$t(\lambda) \propto Ae^{-\frac{xC}{\lambda^4}} \tag{2.19}$$

where λ is the wavelength of the photon, x is the path length of the photon inside the aerogel, *A* is a constant depending on the material and C[$\mu\ m^4$/cm] is a characteristic parameter of the material, the so-called *clarity*. Hence, the perfect conditions would be fulfilled for $A \sim 1$ and $C \sim 0$.
In the next chapters, a nominal refractive index $n = 1.05$ will be used, providing thereshold velocity $\beta_{th} = 0.95$ and the β resolution for $Z = 1$ particles of ~ 0.1 %.

2.3.2.B Mirror

The high-reflectivity mirror surrounding the whole RICH expansion volume is an important tool to increase this subdetector's acceptance. Since around 33% of the photons produced in the aerogel point outside the matrix, the mirror helps recovering the great majority of these photons.

The RICH mirror has a truncated conical shape and is generally described by the following properties:

- Height= 46.3 cm
- Top Radius = 60 cm
- Bottom radius = 67 cm
- Weight= 3.5 kg
- Mixed material composition : SiO_2 (300 nm); Al(100 nm)

The material composition of the mirror guarantees a high conductivity (σ), which ensures a high reflectivity as will be discussed in the next chapter. In addition, the reflectivity of mirror has a weak dependence on photon wavelength (figure 2.15), so it will be not considered in the further study of reflectivity.

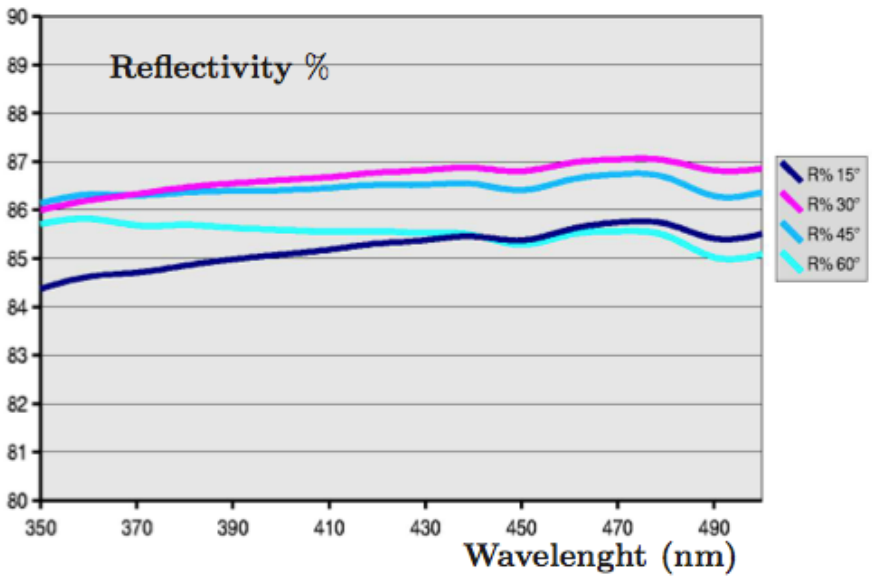

Figure 2.15: Dependence of mirror reflectance on photon wavelength[3].

On other hand, figure 2.16 show the fraction of the photons generated by a particle with $\beta \simeq 1$ that hits the PMT readout matrix after being reflected. In the NaF case, all events are at least partially reflected due to the large aperture of CK cone ($\theta_c \sim 41°$). Although, there will be some energy losses due to Cherenkov photon/mirror interaction, since it is not a perfect metal (more detailed explanation in chapter 5) .

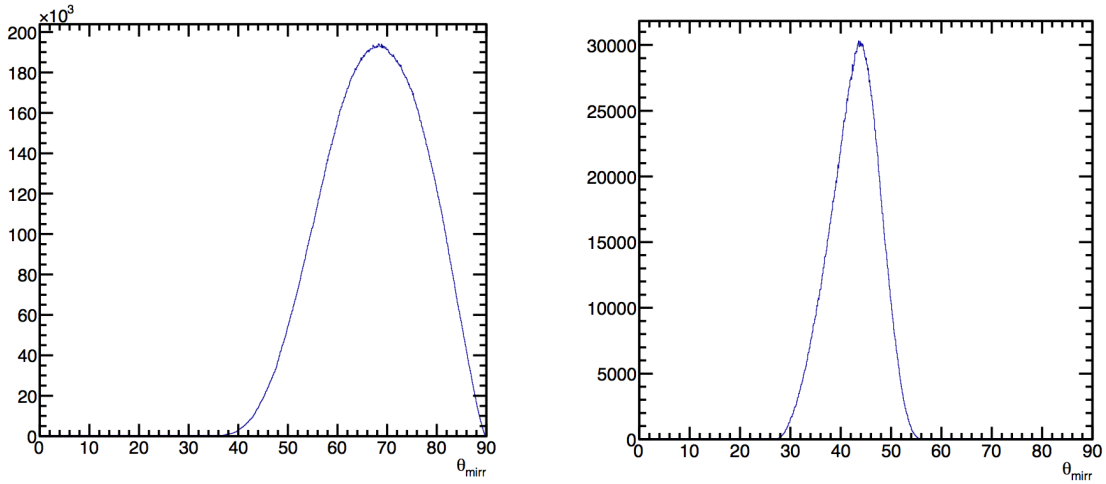

(a) **(b)**

Figure 2.16: Photon's incident angle at the mirror for aerogel (left) and NaF events (right).

2.3.2.C Light guides and detection cells

The matrix plane is composed of an array of adjacent light guides coupled to photomultipliers, so that the dead areas are minimized, and as a result increasing the photon collection efficiency. A LG unit is structured in a pyramidal polyhedron composed of 16 independent plastic tubes glued on a plastic plate. The tubes are made of an acrylic plastic free of UV absorbing additive with a refractive index of 1.49, close to the one of the PMT window ($n = 1.5$). The main purpose of these characteristics was to obtain a transmittance as high as possible over the wavelength range of the PMT detection (from $\sim$300 to 650 nm) .
A schematic insertion of the light guide with a PMT is shown in figure 2.18.

Despite the main goal of reducing the dead areas between adjacent PMTs, there are gaps of 3 mm even at the top of light guides due to the presenece of the shielding and the mechanical asssembly reasons.
Thereby, inside the LG the photons are conducted by internal reflections.The light guide unit is optically coupled to the active area of phototube cathode through a 1 mm flexible optical pad. In perspective, the light guide is generally described by the following properties:

- Total Height: 31 mm
- Total Volume: 13 cm^3
- Collection surface area: 34$\times$34 mm^2
- Readout pixel size: 8.5 mm

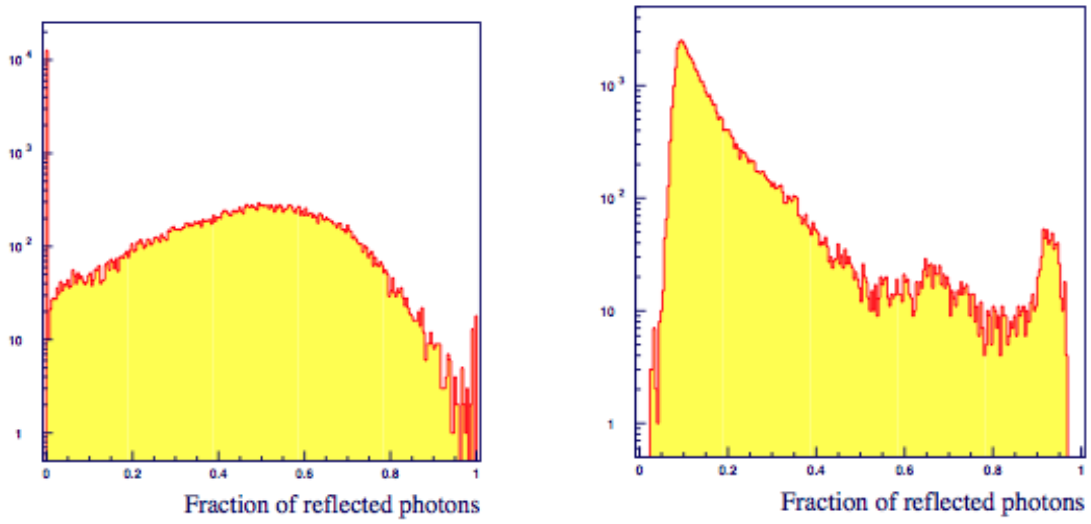

(a) **(b)**

Figure 2.17: Photon's incident angle at the mirror for aerogel (left) and NaF events (right).

The optimal dimensions have been determined so that photon collection efficiency could be maximized.

2.3.3 Photomultipliers

Light detection in the AMS-02 RICH is performed by an array of 680 Hamamatsu PMTs of model R7600-00-M16.[3] This phototube has been chosen due to its reduced size, fast response under low operational voltage (800 V), large anode uniformity and low sensivity to external magnetic fields. On the other hand, the specific needs of the RICH require a high photon efficiency and good spatial resolution to allow a precise reconstruction of the CK ring. Moreover, it has a good single photoelectron resolution and linearity in the response to perform the photon counting needed for charge measurement.

The photomultiplier selected is the 4×4 multianode R7600-00-M16 from Hamamatsu, with a sensitive zone of $4 \times 4\ mm^2$ and a pitch of 4.5 mm. According to figure 2.19, it has the spectral maximum response at approximately $\lambda = 420$ nm.

Regarding the spectrum of the wavelength spectrum of the radiated CK photons, taking into account the chromatic dispersion, $n(\lambda)$, the average quantum efficiency follows

$$< \epsilon_{Q.E.} >= \frac{\int_{\lambda_{min}}^{\lambda_{max}} \epsilon_{Q.E.} \frac{1}{\lambda^2} \left(1 - \frac{1}{\beta^2 n(\lambda)}\right)^2 d\lambda}{\int_{\lambda_{min}}^{\lambda_{max}} \frac{1}{\lambda^2} \left(1 - \frac{1}{\beta^2 n(\lambda)}\right)^2 d\lambda} \tag{2.20}$$

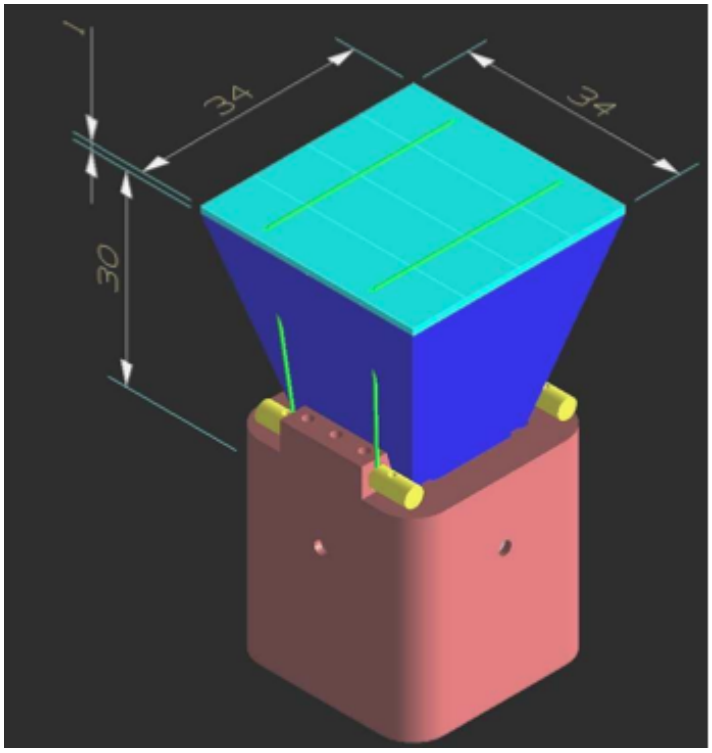

Figure 2.18: PMT housing plus light guide.

which gives for $\beta \simeq 1$ particles in aerogel a mean quantum efficiency $< \epsilon_{Q.E.} >= 0.1443$ and for sodium fluoride $< \epsilon_{Q.E.} >= 0.1444$[3].
When photons strike the photocatode window, a bunch of electrons is removed from the valence band through photoelectric effect. As a result, there is a emission of photoelectrons which will be collected and amplified by a chain of 12 dynodes with a total gain 10^6 for an applied voltage of 800 V. The single photo electron resolution is ~ 0.7 and the response is expected to be linear up to $\simeq 80$ p.e.
The RICH photomultipliers will operate with a high residual magnetic field at the PMT plane ($\sim 300\ G$), so they are protected by a magnetic shield.
The CK photons are then collected through plastic LG positioned on top of the PMTs and connected to the PMT window through a flexible optical pad of 0.5 mm thickness. Each LG has 16 individual guide pipes, one for each pixel.
In addition, the PMT matrix is composed of different modules:

- Square (with 143 cells);
- Triangular (with 27 cells).

As mentioned before there is a non-active area at the centre to insert the electromagnetic calorimeter (ECAL), which is square with a side length of 63 cm. The detailed description of the matrix is represented in the left-hand scheme of figure 2.20 .

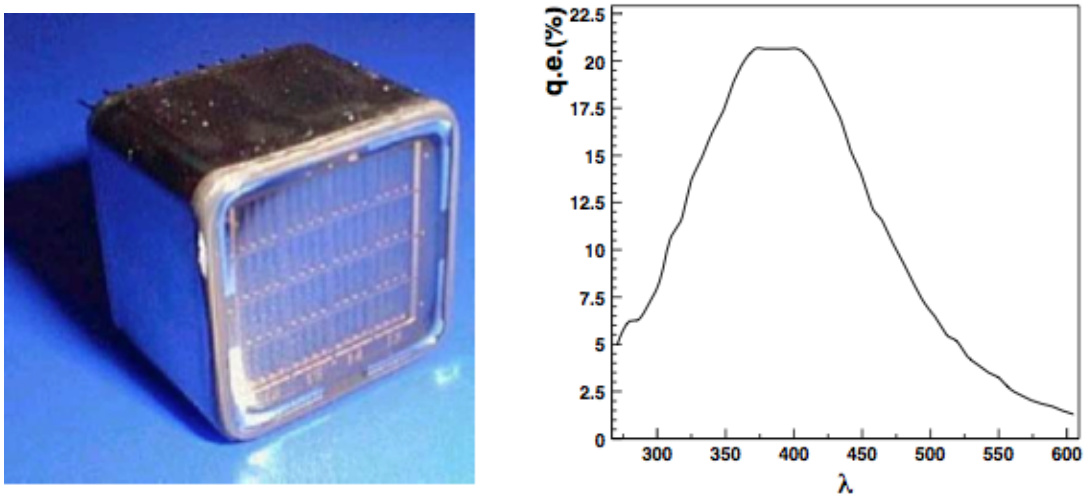

(a) **(b)**

Figure 2.19: a)The R7600-00-M16 Hamamatsu PMT. b)PMT quantum efficiency variation with the detected wavelength.

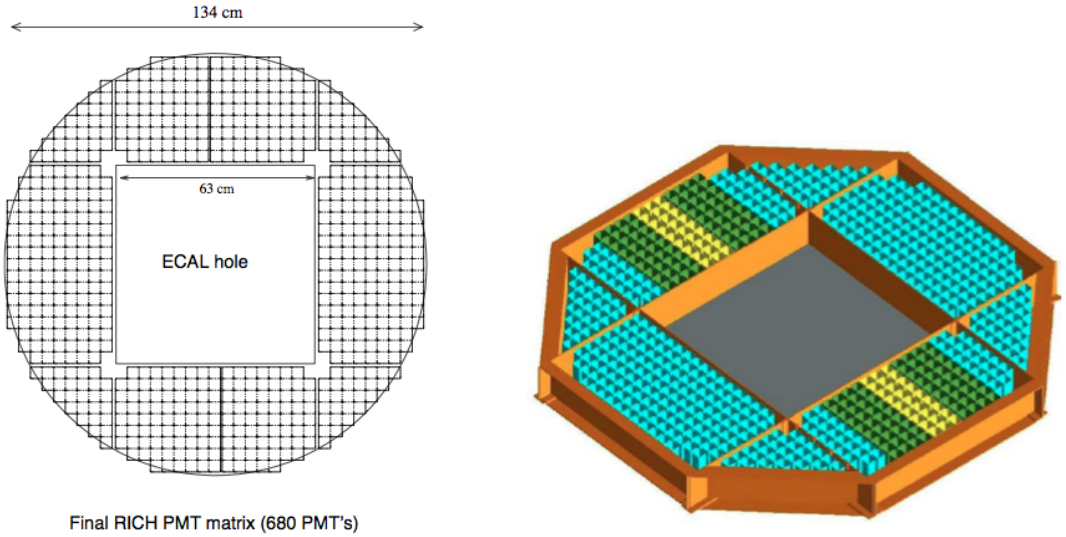

(a) **(b)**

Figure 2.20: a)Top view of the RICH PMT matrix (680 PMTs): detail of the matrix with the active parts and the inactive ones: ECAL hole, module gaps. b) Distribution of the shielding thickness depending on the magnetic field intensity: Yellow cells Thickness= 1.2 mm; Olive Thickness = 1.0 mm; Cyan cells Thickness = 0.8 mm.

3

Charge reconstruction in the RICH

Contents

3.1 Introduction

The Cherenkov photons generated in the RICH radiator are uniformly emitted along the length of the particle path L, inside the dielectric medium and their number per unit of energy depends on the particle's charge, Z, velocity, β, and on the refractive index, n, according to the expression[6]:

$$\frac{dN_\gamma}{dE} \propto Z^2 L\left(1 - \frac{1}{\beta^2 n^2}\right) = Z^2 L \sin^2(\theta_c) \tag{3.1}$$

Therefore, several steps must be taken to accomplish charge reconstruction:

- Cherenkov angle reconstruction (θ_c).
- Particle path length estimation, ΔL, which relies on the information of the particle direction ($\theta_{particle}$, $\phi_{particle}$) provided by the tracker.
- Photoelectron counting associated to the Cherenkov ring.
- Photon detection efficiency evaluation.

The number of photoelectrons (N_{pe}) which will be detected depend on:

- interactions with the radiator: absorption and Rayleigh scattering in the aerogel case (ϵ_{rad});
- photon ring acceptance: part of the photons is lost through the radiator's lateral and inner walls, due to total reflection in radiator-air transition, because of mirror absorption and because some photons fall into a non-active area (ϵ_{geo});
- light guide losses (ϵ_{lg});
- photomultiplier quantum efficiency (ϵ_{pmt}).

Thus, the number of photoelectrons can be simply given by

$$N_{pe} \propto \Delta L Z^2 sin^2\theta_c \tag{3.2}$$

where ΔL is the radiator length crossed by the charged particle and θ_c is the Cherenkov angle. Afterwards, the efficiency factors should be also included in the determination of the number of photoelectrons. Regarding expression , it follows then

$$N_{pe} \propto \Delta L Z^2 sin^2\theta_c \varepsilon^{rad} \varepsilon^{PMT} \varepsilon^{geo} \varepsilon^{LG} \tag{3.3}$$

The expression 3.3 can also be expressed in terms of the number of photons (N_0) emitted by a proton with the same velocity and with the same crossed radiator length, given by

$$N_{pe} = N_0 Z^2 \tag{3.4}$$

where $N_0 = \Delta L sin^2\theta_c \varepsilon^{ring}$ (ε^{ring} is total ring factor efficiency).
Therefore, the charge of the incident particle can be simply estimated by

$$Z^2 = \frac{N_{pe}}{N_0} \tag{3.5}$$

Thus, replacing expression (3.3) in (3.5), the charge can now be expressed as

$$Z = \frac{\beta^2 n^2 - 1}{\beta^2 n^2 - \beta^2} \frac{\cos(\theta)}{N_0} \frac{\sqrt{\sum_{k=1}^{N_{hits}} n_{pe}(k)}}{\varepsilon_{full}(event)} \tag{3.6}$$

The N_{pe} associated error follows from a quadratic expansion given by:

$$(\Delta N)^2 = (\Delta N^{stat})^2 + (\Delta N^{PMT})^2 + (\delta N^{sys})^2 \tag{3.7}$$

where (ΔN^{stat}) is the statistical uncertainty, $\Delta N^{stat} = \sqrt{N}$;$\Delta N^{PMT} = \sqrt{N}\sigma_{pe}$ is the PMT signal amplification's error; finally δN^{sys} is the systematic error whose origin will be addressed after all the algebraic manipulation.
On the other hand, the resulting charge error is given by

$$\Delta Z = \frac{1}{2ZN_0}\Delta_N \tag{3.8}$$

Replacing equation (3.5), it results then:

$$\Delta Z = \frac{1}{2\sqrt{N_0}} \frac{\Delta_N}{\sqrt{N}} \tag{3.9}$$

Inserting ΔN in expression 3.9, the following result comes after some algebraic manipulation:

$$\Delta Z = \frac{1}{2} \sqrt{\underbrace{\frac{1+\sigma_{pe}^2}{N_0}}_{statistical\ error} + \underbrace{Z^2\left(\frac{\delta N}{N}\right)^2}_{systematic\ error}} \tag{3.10}$$

Indeed, charge can also be written as function of Cherenkov radiator key parameters such as refractive index (*n*). In addition, since the charge study will rely on efficiency factors (resulting from Cherenkov photons in the detector), it would be also interesting to include them in charge reconstruction. As a result, the main topics in the next sections will be *efficiency factors* and *charge reconstruction uncertainties* resulting from expression (3.6).

3.2 Efficiency determination: 1-D approach

The 1-D approach is a charge determination method where the main geometry factor (detector acceptance) is described by azimuthal angle (φ) in the charged particle frame (see figure 3.1). This approximation can be performed since number Cherenkov photons is uniform along ϕ around particle direction [11].

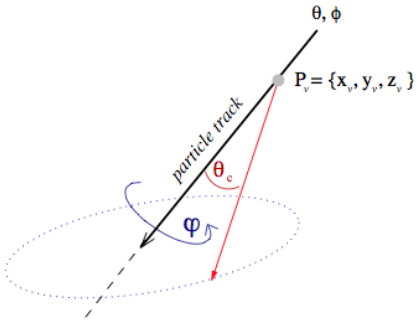

Figure 3.1: Description of the particle track and photon ring emission geometry. The particle trajectory depends on $\{x_v, y_v, z_v, \theta, \varphi\}$, while each photon is parameterized by θ_c and azimuthal angle φ [3].

It turns out that ring acceptance is the fraction of radiated photons. For instance, it will regard some geometry factors such as:

- the number of photons reaching the photomultiplier;
- ring pattern's topology (e.g. particle's impact point, direction and velocity; Cherenkov angle) and RICH geometry.

In addition, the RICH geometric acceptance will also include different photon loss factors given by:

- photons escaping through the radiator's lateral and inner walls (ϵ_{wall});
- losses in the conical mirror (the mirror's reflectivity is assumed to be $\sim 85\%$);
- reflection of Cherenkov photons at the radiator-air interface;
- photons falling in a non-active area of the detector plane (gaps in the PMTs, ECAL hole, dead PMTs or pixels).

Figure 3.2 shows a typical Cherenkov ring patterns generated in NaF (a) and Aerogel (b) radiators.

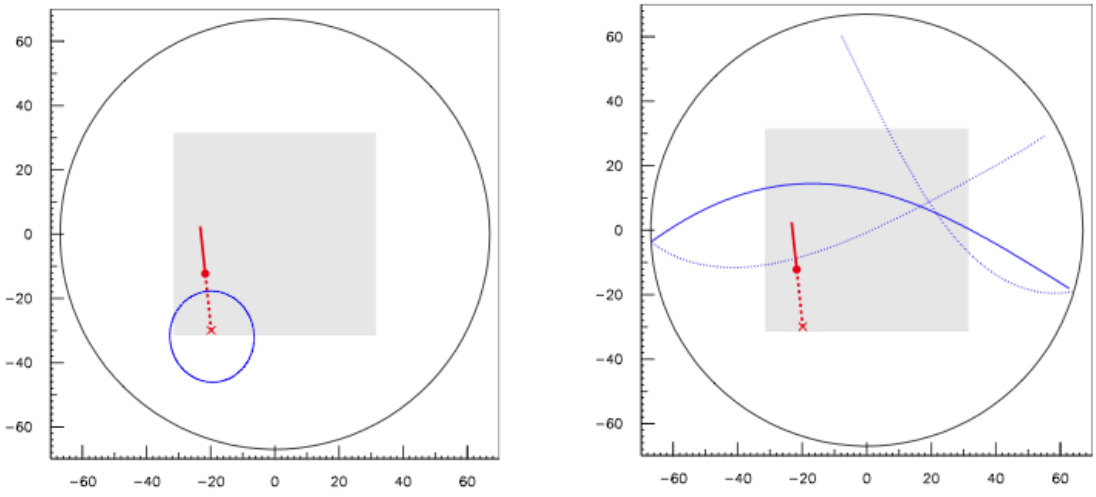

Figure 3.2: Two patterns for the same particle kinematics ($\beta = 0.9999$ and $\theta = 20^0$). The particle track projection is described by the dashed line. The symbols $\cdot$ and $\times$ indicate the positons at the radiator top level and at the detection matrix, respectively. a) Ring pattern for an aerogel ($n = 1.050$) event. b) Ring pattern for a NaF ($n = 1.334$) event [10]

The charged particle with $\beta \sim 1$ emits a very large cone - aperture of 41 ^{0}- when it crosses the NaF radiator and this is why there are almost always reflected photons. In fact, in NaF events an average of about 50% of the Cherenkov ring is reflected at the mirror.

Considering the same kinematic conditions, the aerogel radiator's distribution regarding the fraction of reflected photons has a larger standard deviation than NaF one. The Cherenkov angle is approximately $\sim 18^0$ for $\beta \sim 1$. Adding the previous ideas, it can be marked a correlation between the particle's direction (θ, ϕ) and impact point on radiator (x_v,y_v) (see figure 3.1) with Cherenkov cone detection (this will be discussed in chapter 5).

As a result, for a certain event, the global photon ring acceptance is obtained by adding the different fractions of detected photons. The fraction of photons hitting the PMT matrix directly (ϵ_{geo}^{Dir}) is added to the fraction of incident photons in the mirror (ϵ_{geo}^{Mir}) weighted by the mirror reflectivity (ρ). Therefore, the photon ring acceptance is given by:

$$\epsilon_{geo} = \epsilon_{geo}^{Dir} + \rho\epsilon_{geo}^{Mir} \tag{3.11}$$

In addition to this effect, there will be an effect that will also play a role in geometrical efficiency: the loss of photons in the ECAL hole (ϵ_{geo}^{hole}).

Considering that Cherenkov photons are emitted uniformly along azimuthal angle (φ)

around particle's reference frame, the values of ϵ_{geo}^{Dir},$\epsilon_{geo}^{Hol}$and ϵ_{geo}^{Mir} correspond to the extreme intersection points of the Cherenkov cone with the non-active regions of the detector, φ_h, together with the mirror, φ^m (see in figure 3.3).

$$\epsilon_{geo}^{Dir} = \frac{|\varphi_1^m - \varphi_1^h| + |\varphi_2^m - \varphi_2^h|}{2\pi} \tag{3.12}$$

$$\epsilon_{geo}^{Mir} = \frac{|\varphi_2^m - \varphi_1^m|}{2\pi} \tag{3.13}$$

$$\epsilon_{geo}^{Hol} = \frac{|\varphi_2^h - \varphi_1^h|}{2\pi} \tag{3.14}$$

For a more detailed explanation see thesis [3].

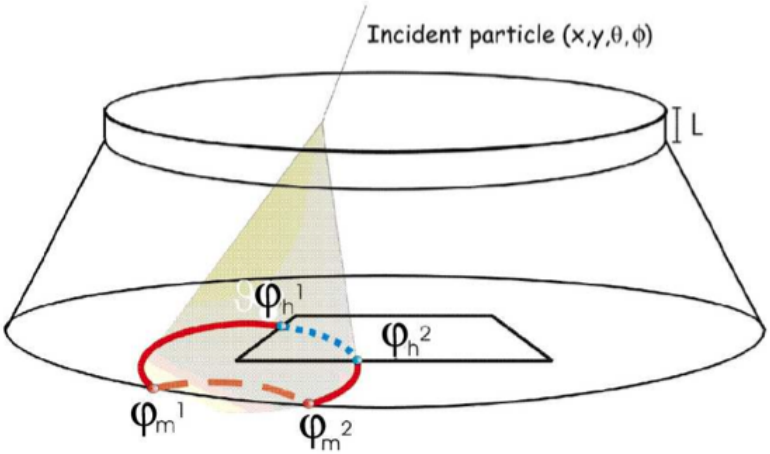

Figure 3.3: 3-dimensional view of photon pattern tracing in RICH detector.

3.2.1 Radiator wall efficency

Neither of the two RICH radiators is made of a single block. There are 92 aerogel tiles and 16 tiles for NaF. Aerogel tiles are separated by opaque poron walls. Hence, if a particle crosses the radiator near a tile edge, it could happen that part of its Cherenkov photons may be lost (since those photons hit the walls), or are not radiated at all, as shown in figure 3.4.

The study of this effect is based on the following motivation: the spread of Cherenkov light emission along the radiator's thickness. This effect partially explains the Cherenkov ring's non-zero width.

On the other hand, the Cherenkov photon emission point is described for the most purposes as approximately fixed, ignoring the vertical spread in the particle radiation emission process. In this case, however, since the effect in question is linked with radiator gaps, this approximation cannot be assumed, so a ring sampling was performed at 10 different points along the particle's trajectory in the radiator region.

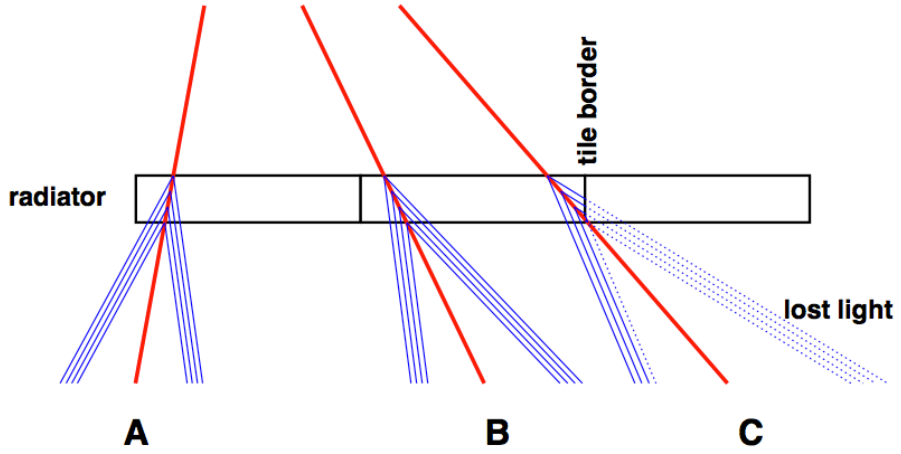

Figure 3.4: Effect of radiator walls on collected light. Cherenkov cones for particles A and B are not affected, but for particle C a significant fraction is blocked by the opaque poron wall between tiles.

Afterwards, an average result (fraction of points not impacting radiator walls, each point weighted according to the expected light loss from top to bottom due to Rayleigh scattering) is used to correct the global efficency.

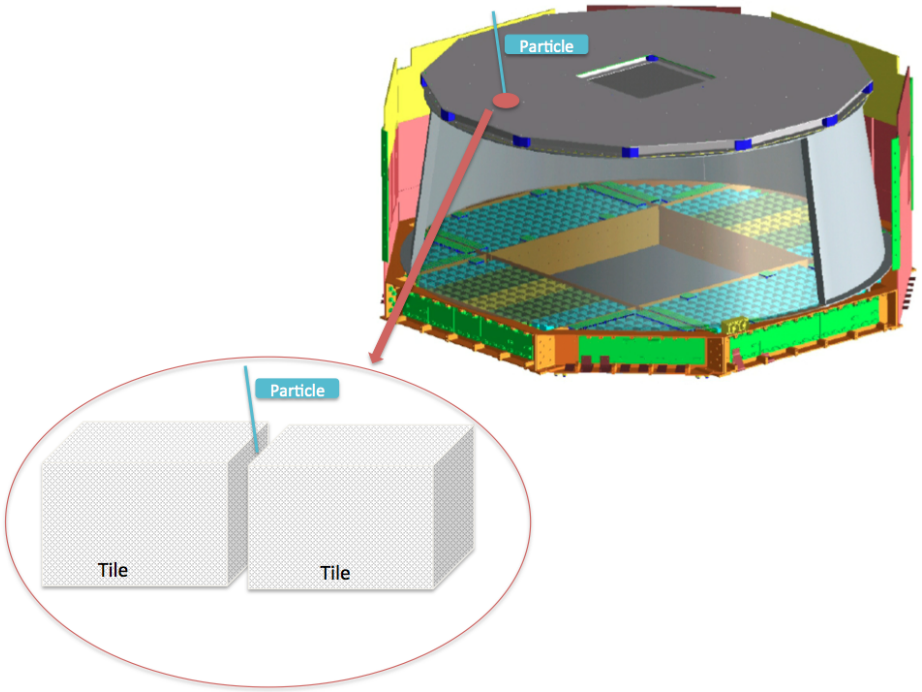

Figure 3.5: Charged particle crossing the edge of aerogel/NaF tiles.

3.2.2 Rayleigh scattering and radiator absorption

The main interactions of Cherenkov photons inside aerogel are due to Rayleigh scattering and absorption, while for the NaF radiator the only significant interaction that photons can suffer is absorption, although, it is negligible since the radiator thickness is very small compared to the absorption length. Considering that the absorption rate is two orders of magnitude below the scattering rate in the aerogel, then it can be neglected in a first approximation. However, there is another considerable effect resulting from transition of Cherenkov photons between radiator (dielectric) and air due to their polarization (it will be discussed further in chapter 5). Nevetheless, the interaction rate of photons inside the radiator is function of the two main variables that follows[3]:

- Distance crossed by the photons inside the radiator : $d_\gamma(\theta,\ \phi,\ \theta_c,\ z,\ \varphi)$;
- Interaction length: L_{int}.

The distance d_γ depends on particle direction ($\theta,\ \phi$), photon emission point (z) and photon azimuthal angle φ. Actually, the photon crossed distance can be simply written as $d_\gamma(z,\ \varphi)$ for each photon generated by the same particle. On the other hand, the interaction length depends on the wavelength of the photons, according to the following expression

$$L_{int} = \frac{\lambda}{C}[cm] \tag{3.15}$$

where *C* is the radiator's optical clarity in $\mu m^4 cm^{-1}$. For instance, the aerogel radiator has an interaction length given approximately by [13]

$$L_{int}(C) = \frac{0.0327}{C^{0.867}}[cm] \tag{3.16}$$

In order to find the radiator efficiency it is necessary to integrate the probability of a photon not to interact in the radiator, given by :

$$p_\gamma^{int} = e^{-\frac{d_\gamma(z,\varphi)}{L_{int}}} \tag{3.17}$$

Therefore, the fraction of photons suffering no radiator interaction (*radiator efficiency*) can be evaluated through the following expression:

$$\varepsilon_{rad} = \frac{1}{\Delta\varphi H_{rad}} \int_0^{H_{rad}} dz \int_{\varphi^i_{min}}^{\varphi^i_{max}} e^{-\frac{d_\gamma(z,\varphi)}{L_{int}}} d\varphi \tag{3.18}$$

where H_{rad} is the radiator thickness. For instance, for an aerogel radiator ($n = 1.050$), with a clarity coeficient $C = 0.0052 \mu m^4 cm^{-1}$ and a thickness $H_{rad} = 2.5\ cm$, the average ϵ_{rad} is about 65% (see figure 3.6). For more detailed derivation see [3].

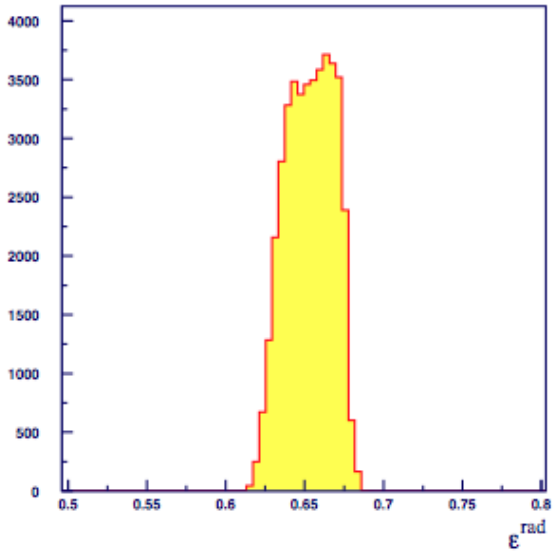

Figure 3.6: Distribution radiator efficiency event by event, ϵ_{rad}, for an aerogel radiator ($n = 1.050$), 2.5 cm thick, with a clarity coefficient $C = 0.0052 \mu m^4 cm^{-1}$[3].

3.2.3 Photomultiplier efficiency

The main PMT effect is described by quantum efficiency (ϵ_{PMT}). Ultimately, only a small fraction ($\epsilon_{PMT} \simeq 10\%$) of Cherenkov photons reaching the PMT window are detected. Generally, this efficiency is expected to be similar for all PMTs and photon trajectories. Therefore, it may be incorporated, at least in first approximation, as a global factor.

3.2.4 Light guide efficiency

The detection of Cherenkov photons at the LG surface faces two potential inefficiencies: photons may be reflected at surface or transmitted between adjacent light guide divisions. The LG effiency factor ϵ_{LG} depends on the incident angle of the photons at its top (θ_γ).Therefore, photon inclination and impact point will influence the probability of a photon being transmitted and reaching the PMT window. Figure 3.7 shows light guide efficiency as function of photon inclination, which was obtained from detailed simulations performed at LIP of photon propagation in the AMS pyramidal light guides, and is incorporated in the LIP charge reconstruction algorithm. Moreover, from figure 3.7 it can be estimated that the highest efficiency ($\sim 75\%$) occurs for perpendicular incidence (for Monte Carlo events), for photon inclinations not greater that 20^0 with respect to the interface normal. Then, it drops rapidly from $\sim 70\%$ at 20^0 to $\sim 50\%$ at 35^0.

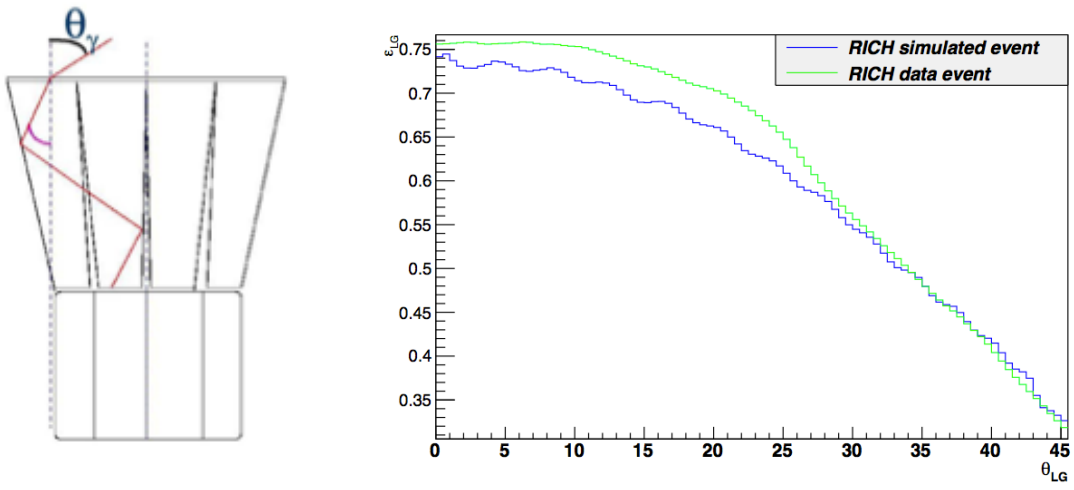

(a) **(b)**

Figure 3.7: a)Light guide scheme with the definition of the photon incident angle(θ_γ). b)Light guide efficiency as function of the incident angle at the top of the light guide for both RICH simulation and AMS data.

The efficiency is calculated event by event taking into account the probability of a given photon getting into the photomultiplier cathode since it entered the LG, and integrating it along the reconstructed photon pattern:

$$\epsilon_{LG} = \frac{1}{\Delta\varphi}\int_{\Delta\varphi} \epsilon_{LG}[\theta_\gamma(\theta,\theta_c,\varphi)]d\varphi \tag{3.19}$$

Therefore, according to the expression 3.19 light collection efficiency depends not only on *photon inclination* θ_γ, but also on the *photon's azimuthal angle* φ_γ. This shows a change in LG efficiency calculation, since there will be a correlation with the pair coordinates $(\theta_\gamma, \phi_\gamma)$ and the Cherenkov ring covering of the active LG surface, which will constrain the number of detected photons. In further detail, LG size is 34×34 mm and the LG pitch is 37×37 mm, the fraction of active area is $\left(\frac{34}{37}\right)^2 = 84.4\%$. Even though the region covered by LG gaps is small compared with the Cherenkov ring area, there are significant uncertainties on the fraction of photons falling in LG gaps. This means that the correspondent systematics should be minimized.
On the other hand, figure 3.7 heads to an intrinsic problem in LG efficiency resolution (comparing with RICH simulation), i.e., there is a granularity problem from considering the PMT as standard unit of detection. As a matter of fact, figure 3.9(b) marks clearly a variation in pixel signal within the same PMT. This allows to infer a variation of the signal according to the kind of pixel, since each one has a different collected signal, i.e., the number of detected photoelectrons changes with the pixel position within the PMT. Hence, LG efficiency ε_{LG} will also depend on pixel position in PMT (

x_{pixel}, y_{pixel}).

Following the official AMS pixel numbering (0-15), the division of pixels into types (see figure 3.8) may be established as:

- *Central pixels*: numbers 5, 6, 9, 10;
- *Side pixels*: 1, 2, 4, 7, 8, 11, 13, 14;
- *Corner pixels*: numbers 0, 3, 12, 15.

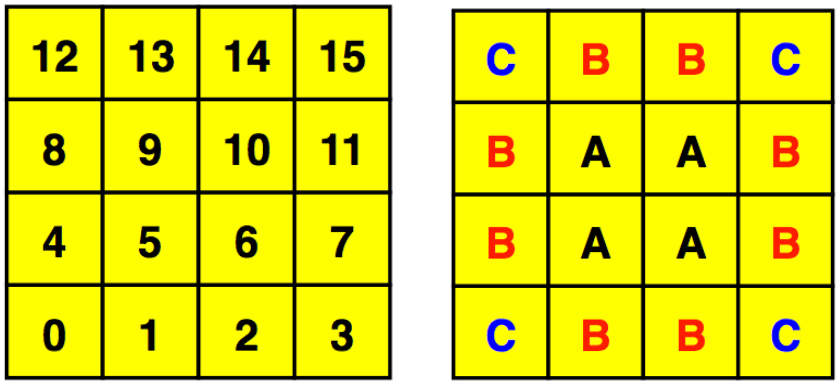

Figure 3.8: a) RICH pixel numbering scheme. b) Pixel classification as central (A), side (B) and corner (C) types.

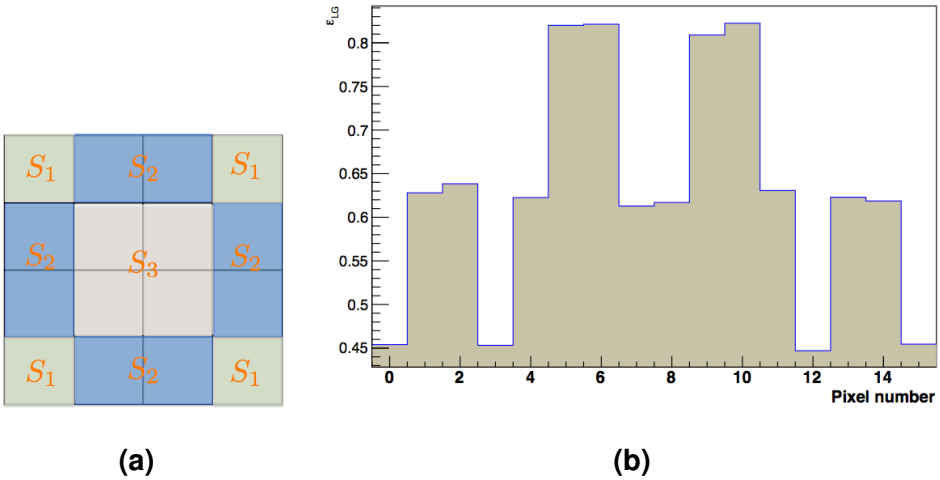

Figure 3.9: a) RICH pixel signal within a PMT. b) Quotient of the number of collected by the number of expected photoelectrons as function of pixel number (aerogel events).

Furthermore, it is well known that the observed Cherenkov ring patterns are not infinitely thin (*ring width*). Such condition comes both from detection limitations

and from variations in photon emission trajectory, which means an uncertainty in pixel/PMT detection. Ideally, a radiator with a thickness near zero would have a fixed emission point for all Cherenkov photons, but particles crossing the radiator will produce a superposition of slightly offset cones. This fact also points toward a new approach beyond the simple azimuthal sampling described in the beginning of this section.
Furthermore, figure 3.9 shows a larger collected signal (S_3) for central pixels than side pixels (S_1). From this fact follows that LG detection efficiency changes according to the pixel type. As a result, each pixel type should have a different weight to the Cherenkov ring detection efficiency.
In order to address that situation, a new computational model was implemented so that a 2-dimensional distribution weighted by the pixel importance could be included in the LIP algorithm. Hence, this new approach will regard the following three main principles:

- Ring characterization is based on sampling the ring at regular intervals;
- The ring is treated as a set of probabiblity distributions centered in each sampled point;
- Acceptances and efficiencies are calculated and store for each PMT or pixel touched by the ring. Global results may be obtained from the addition of all PMT/pixel contributions.

3.3 Efficiency determination: full ring width approach

3.3.1 Introduction

Ring sampling will depend on radiator properties, reconstructed Cherenkov cone and ring parameters. Regarding this, photon trajectories are calculated for a number of points at equally spaced intervals (see figure 3.11) in azimuthal angle (currently the number of points is 1000, so that they can be separated by shorter distances and therefore obtaining a better sampling).
Hence, the photon's trajectory is followed only if it reaches the matrix detection plane. The new charge reconstruction algorithm, is based on a new approach, *ring segmentation*, that describes the expected contribution to the Cherenkov ring signal coming from photons with a specific reflection status at a specific PMT/pixel.
The main goal of ring sampling and smearing calculations is evaluating the contribution of each PMT/pixel to the global detection efficiency. This results from listing the

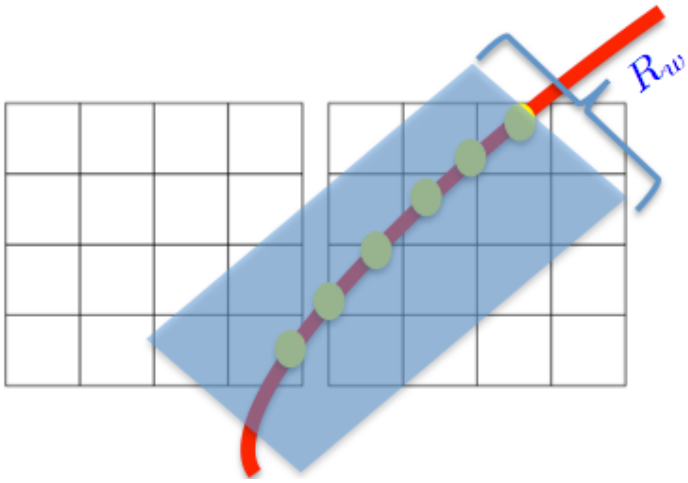

Figure 3.10: Description of Cherenkov ring (red line) width (R_w) within touched PMTs.

ring points and each point contribution to that specific PMT/pixel (in the next section, there will be a further description about each point's contribution).
The implementation of the segment-based approach allows the assignment of a photon direction to each ring segment.
In further detail, the photon direction stored in each segment is obtained by evaluating the sampled ring points as follows:

- Since all points assigned to a given segment have the same reflection status and are mapped near each other, their directions should be quite similar.
- Most of the photons tend to perform angles less than $\sim 50^{\circ}$ with the PMT matrix's normal, so an average is applied over the *x* and *y* components of each sampled point trajectory. Each trajectory is weighted by the fraction of each point's smeared distribution contributing to that specific segment. As a result, global *x* and *y* components are obtained (plus a downward z component chosen to keep vector length normalized at 1) representing the segment's average photon trajectory.
- The final result is stored as part of segment data in the form of two photon angles θ_γ and ϕ_γ.

3.3.2 Point smearingt 2-D

Point smearing is about including ring width uncertainty, leading to a more precise calculation of geometrical efficiencies such as the LG one.
Ring width is an effect that emerges from uncertainties in the measured impact point

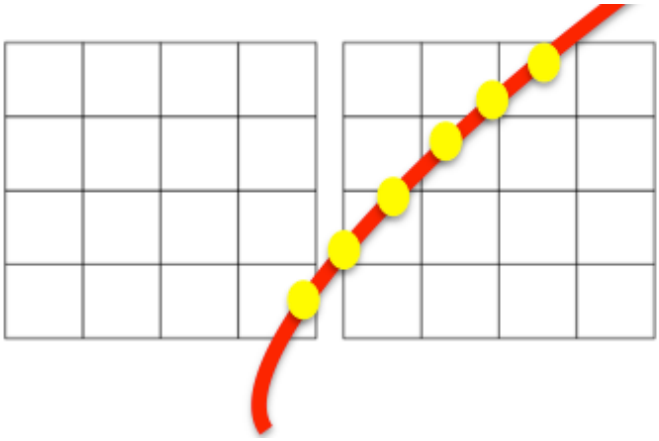

Figure 3.11: Ring discretization for a number of points at equally spaced intervals in azimuthal angle.

of each ring photon. These variations result from deviations of photon trajectories from an ideal Cherenkov cone (e.g. radiator chromacity or thickness), but also from limitations in the detection matrix (e.g. pixel/PMT size).
The ring width may be simulated using the set of points obtained from ring sampling. Hence, stating the reference point as the one resulting from the expected ring (central ring), these uncertainties will result from an isotropic perturbation in longitudinal and transversal components. Since over small distances ($\sim 1cm$) the ring is approximately a straight line, the longitudinal component does not change the ring width and the point remains on the ring. It follows easily that transverse component produces the uncertainty in the ring profile.
Under the assumption of isotropy, any pair of perpendicular spreads has the same magnitude. Point smearing is applied using the RICH detector's standard x-y axes (see figure 3.12).
The knowledge of reconstructed AMS rings means that an estimate of the ring's transverse spread is well known. This spread is incorporated in the likelihood function used for LIP's velocity reconstruction as a composition of two Gaussian distributions (see figure 3.12), i.e., a sum of two Gaussian contributions described as follows for both aerogel and NaF events:

- *Aerogel Event*:
  - $Width = 0.374$ cm (Contribution:76%);
  - $Width = 1.348$ cm (Contribution:24%).
- *NaF Event*:
  - $Width = 0.5424$ cm (Contribution:47.23%);

– $Width = 1.35$ cm (Contribution:52.77%).

For simplicity reasons, this charge reconstruction method will use a single Gaussian spread for each point with a width (along each axis) given by the first Gaussian value used in the likelihood function, i.e., 0.374 cm for aerogel events and 0.5424 cm for NaF events.

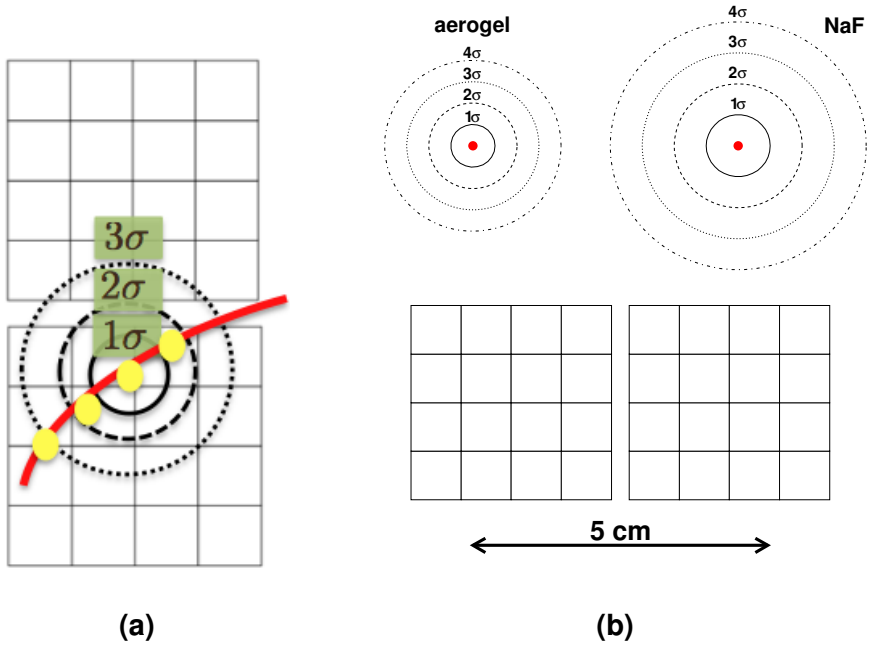

Figure 3.12: a) Ring point sampling and associated uncertainty due to ring width. b) Comparison of point smearing distances for aerogel ($\sigma = 0.374$cm) and NaF ($\sigma = 0.5424$cm) with the size of detection cells (3.4×3.4cm).

The main calculation of all efficiencies, apart from the geometrical one, is performed at the level of ring points. For instance, there are two key efficiencies which are strongly related with photon trajectory given by:

- the radiator inefficiency due to Rayleigh scattering in aerogel events is estimated from the photon inclination (θ_γ) and from the tile's optical clarity;
- photon losses at light guide detection are function of θ_γ and azimuthal angle φ_γ, when reaching the detection matrix plane.

As a result, the total efficiency and radiator efficiency are obtained for each sampled point.
However, as mentioned before, the RICH matrix granularity is given by a pixel/PMT grid. Therefore, the standard scope to describe efficiency should be an evaluation at the PMT or pixel level.

In further detail, each pixel will have a cluster of points (see figure 3.12) with different contributions (point smearing) to the total pixel efficiency, according to the 2-D Gaussian probability distribution ($P_{i\ j}$, where *i* is a Cherenkov ring point and *j* is the pixel number).
Nevertheless, the physical meaning results from summing all the point contributions for each pixel *j* as described in the following expression:

$$P_j = \frac{1}{N_0} \sum_i P_{i\ j} \tag{3.20}$$

where N_0 is ring total number of points.
The equation 3.20 evaluates the fraction of ring intergrated by each point *i*. In other words, ot describes the acceptance of point *i* belonging to a certain Cherenkov ring. The next leap would be the introduction of pixel efficiency together with the summation over all the ring points, described as follows:

$$\varepsilon_{ring} = \sum_j \underbrace{\varepsilon_j^{LG} \sum_i \frac{1}{N_0} P_{i\ j} (\varepsilon^{rad} R^{n_{reflec}})_i}_{\varepsilon_j} \tag{3.21}$$

where $R^{n_{reflec}}$ is the reflectance at mirror and ε_j is the pixel efficiency. From equation (3.21), ring efficiency can be simply given by the following expression:

$$\varepsilon_{ring} = \sum_j \varepsilon_j \tag{3.22}$$

Moreover, since point smearing is required to evaluate the integrated acceptance and efficiency in each PMT and pixel, it should follow the next two implementation steps:

- The integration region of Gaussian smearing is a square;
- The 2-D Gaussian smearing may be obtained as a product of two independent one-variable Gaussian smearings:

$$\begin{aligned} P(x = x_j, y = y_j) &= P(x = x_j) P(y = y_j); \\ i = \{1, 2, 3, ..., N_{seg}\}, j &= \{1, 2, 3, ..., N_{pixel}\} \end{aligned} \tag{3.23}$$

In geometrical terms, each PMT/pixel is defined by the conditions (see figure 3.13)

$$x_{1\ j} < x_j < x_{2\ j} \ \wedge \ y_{1\ j} < y_j < y_{2\ j} \tag{3.24}$$

where the coordinates are considered at the top of LGs and the indexes $\{i, j\}$ are self-explained in equation 3.23. In addition, each pixel have an average Cherenkov

photon direction, i.e., the mean value of the cartesian coordinates over all the Cherenkov photons falling in pixel *j*. Therefore, it follows a set of coordinates (in RICH frame) given by:

$$(x_j, y_j; \theta_j, \phi_j)$$

In order to simplify the notation, the following changes should be considered:

$$(x_j \equiv X, y_j \equiv Y; \theta_j \equiv \Theta, \phi_j \equiv \Phi)$$

As a result, the integrated probability over that PMT/pixel of a distribution centered at point *C* with coordinates (X_C, Y_C) is given by

$$P_C(X_1 < X < X_2, Y_1 < Y < Y_2) = P(X_1 < X < X_2)P(Y_1 < Y < Y_2) \tag{3.25}$$

Since each axis has a probability value corresponding to the integral of the Gaussian distribution *g* centered at the point coordinate and regarding the chosen standard in deviation (see figure 3.13), it follows that:

$$P_{x_C}(X_1 < X < X_2) = \int_{X_1}^{X_2} g(\mu = X_C, \sigma) \tag{3.26}$$

$$P_{Y_C}(Y_1 < Y < Y_2) = \int_{Y_1}^{Y_2} g(\mu = Y_C, \sigma) \tag{3.27}$$

The Gaussian integral in expression 3.3.2 can be written as

$$\int_{X_1}^{X_2} \frac{1}{\sqrt{2\pi}\sigma_x} e^{-\frac{1}{2}\left(\frac{X-X_C}{\sigma_x}\right)^2} dx \tag{3.28}$$

Applying a change of variable given by

$$k = \frac{1}{2}\left(\frac{X - X_C}{\sigma_x}\right)^2 \tag{3.29}$$

thus equation 3.28 can be expressed as [12]

$$\frac{1}{\sqrt{\pi}} \int_{\frac{X_2-X_0}{\sqrt{2}\sigma_x}}^{\frac{X_1-X_0}{\sqrt{2}\sigma_x}} e^{-k^2} \tag{3.30}$$

where it was considered that the differential dX comes from the following expression:

$$dX = dk\sigma_X\sqrt{2}$$

Using a similar procedure to *Y* feature, equations and can now be written in terms of the so-called error function $Erf(t)$ as follows:

$$P_{X_C}(X_1 < X < X_2) = \frac{1}{2}\left[Erf\left(\frac{X_2 - X_C}{\sigma\sqrt{2}}\right) - Er\ f\left(\frac{X_1 - X_C}{\sigma\sqrt{2}}\right)\right] \tag{3.31}$$

$$P_{Y_C}(Y_1 < Y < Y_2) = \frac{1}{2}\left[Erf\left(\frac{Y_2 - Y_C}{\sigma\sqrt{2}}\right) - Er\ f\left(\frac{Y_1 - Y_C}{\sigma\sqrt{2}}\right)\right] \tag{3.32}$$

whereas

$$Erf(t) = \frac{2}{\sqrt{\pi}} \int_0^t e^{-k^2} dk \tag{3.33}$$

Therefore, the fraction of the smeared distribution centered at *C* falling on that PMT/pixel is therefore

$$P_C(X_1 < X < X_2, Y_1 < Y < Y_2) = \\ = \frac{1}{4}\left[Erf\left(\frac{X_2 - X_C}{\sigma\sqrt{2}}\right) - Erf\left(\frac{X_1 - X_C}{\sigma\sqrt{2}}\right)\right]\left[Erf\left(\frac{Y_2 - Y_C}{\sigma\sqrt{2}}\right) - Erf\left(\frac{Y_1 - Y_C}{\sigma\sqrt{2}}\right)\right] \tag{3.34}$$

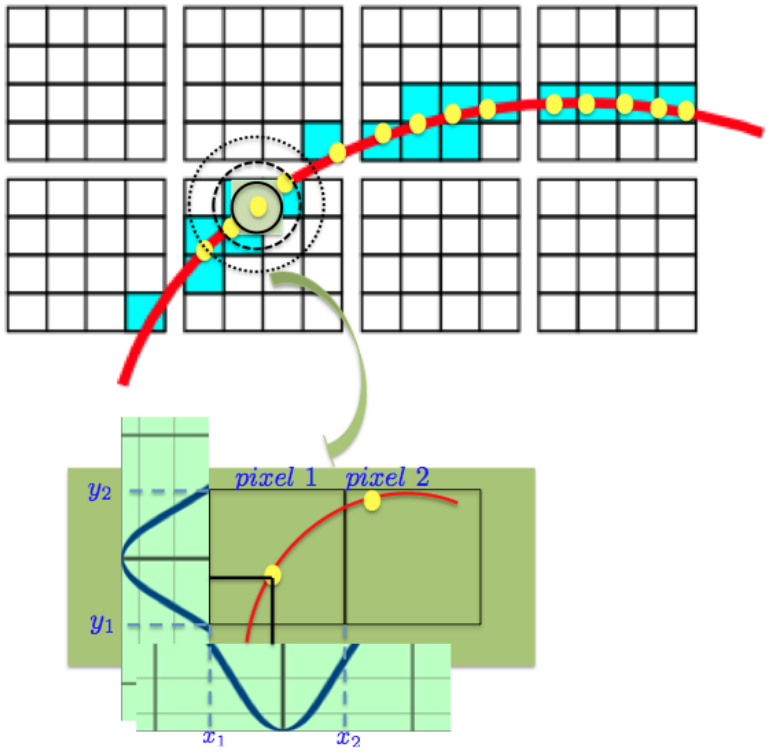

Figure 3.13: Integration of the ring segment points for each each pixel.

Integrated efficiency

The full ring efficiency is easily obtained from adding all pixel contributions and finally inserting the radiator wall efficiency, which results in following expression:

$$\varepsilon^{ring} = \frac{1}{2\pi H_{rad}} < \varepsilon_{PMT} > \sum_j^{N_{pixel}} \sum_i^{N_{seg}} \left(\varepsilon^{Wall}\right)_i \varepsilon_j^{LG} Acc_j \tag{3.35}$$

whereas ε_j^{acc} corresponds to each pixel acceptance, given by

$$Acc_j = R^{n_{refl}} \frac{\sum_i^{N_{seg}} P_{i\,j}}{\sum_{i,j} P_{i\,j}} \equiv R^{n_{refl}} \frac{\sum_i P_{i\,j}}{N_{point}} \tag{3.36}$$

and ε_j^{LG} is LG efficiency.

Integrated efficiency results

In accordance to the new approach to ring evaluation at the matrix, the precision of Cherenkov photon detection is studied at the finest segmentation level: pixel size. This allows to measure with detail the position of photons hitting the PMT matrix, as well as the partial ring signal resulting from pixel activation.

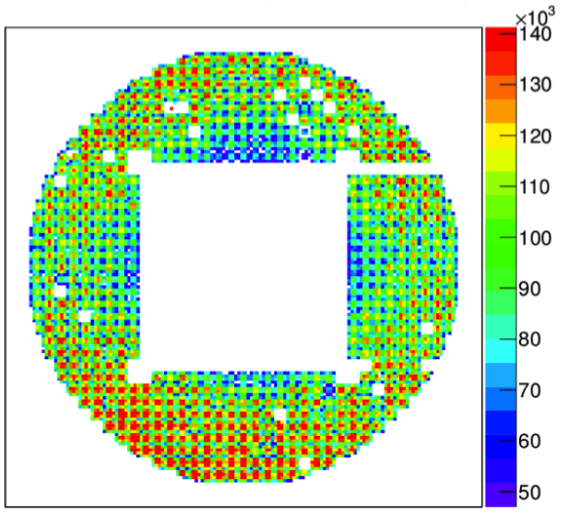

Figure 3.14: Detailed view by pixel shows higher light collection efficiency for central pixels in each light guide.

As a result, one of the upgraded features is acceptance, i.e., the geometric efficiency of RICH detector. For events with higher acceptance (see figure 3.15), there will be a better reconstruction of Cherenkov ring.
On the other hand, the integrated efficiency considering only the radiator will be introduced in each point contribution according to the corresponding photon trajectory. Describing the photon trajectory as function of angular coordinates $(\theta_\gamma, \phi_\gamma)$, it follows that full efficiency will depend of photon angles for each impact point (see equation 3.35).
Figure 3.15(a) shows the distributions of the full detection efficiency for Carbon events. It turns out that aerogel distribution peaks at $\varepsilon \simeq 0.3$, while the NaF distribution has a double peak at $\varepsilon \simeq 0.09$ and $\varepsilon \simeq 0.15$. This means a higher full efficiency for aerogel events, which matches the results shown in figure 3.15(b).

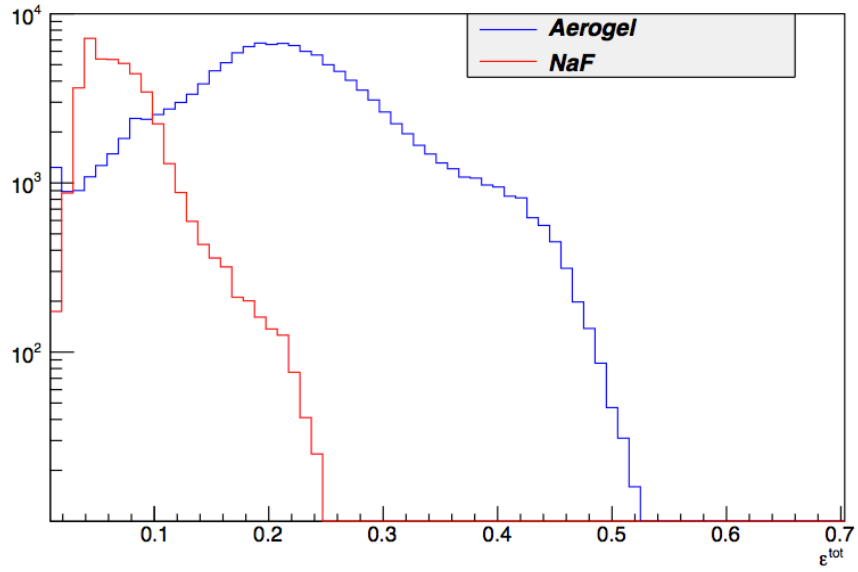

(a)

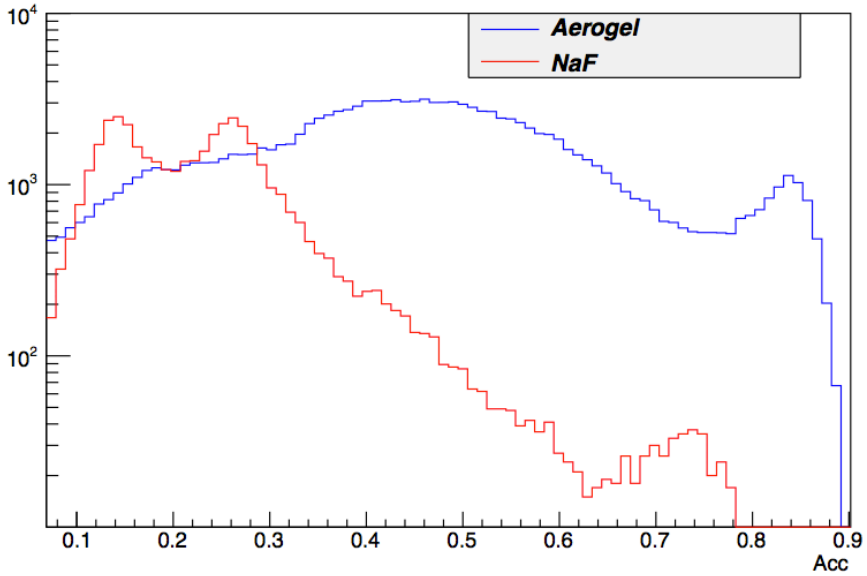

(b)

Figure 3.15: a) Full efficiency for Carbon events. b) Geometrical acceptance evaluation for Carbon events.

4

Monte Carlo simulation of Cherenkov polarization effect

Contents

4.1 Introduction

The propagation of Cherenkov photons in the three main RICH's interfaces will be studied:

- Radiator interface (*dielectric*/air);
- Mirror surface (*metal/air*);
- LG surface entrance (air/dielectric).

Since Cherenkov photon is an electromagnetic-wave, it is described by two following basic properties (see figure 4.1)

- polarization (aligned with electric field $\vec{E}$);
- wave-vector ($\vec{k}$).

Combining the two previous key ideas, it turns out that Cherenkov photon transition between radiator-air will have a non-zero probability of being reflected, depending on the polarization and wave-vector. In other words, since photon's reflectance $\left(R = \left| \frac{\vec{E}_r}{\vec{E}_i} \right|^2 \right)$ crossing a dielectric boundary (radiator interface) is non-zero and therefore there will probably be significant energy losses. In addition, since the mirror is coated with an non-perfect conductor, there will also be a non-100% reflectance in photon reflection.
Therefore, the purpose of this chapter will be the study of the effect of Cherenkov polarization in energy losses for radiator and mirror surfaces. Hence, the following topics will be approached:

- Cherenkov Photon's reflectance/transmittance;
- Evaluation of Cherenkov polarization effect.

4.2 Reflectance and Transmittance

From appendix sections A and B it is obtained the wave-vector and polarization vector for refraction and reflection optics. From this point, the next step towards the final goal, which is the evaluation of polarization effect in energy loss through the RICH's dielectric interfaces, is to study photon *reflectance*/*transmittance* as function of polarization's main feature: the polarization angle α_i for incident, α_r for reflected and α_t transmitted waves.

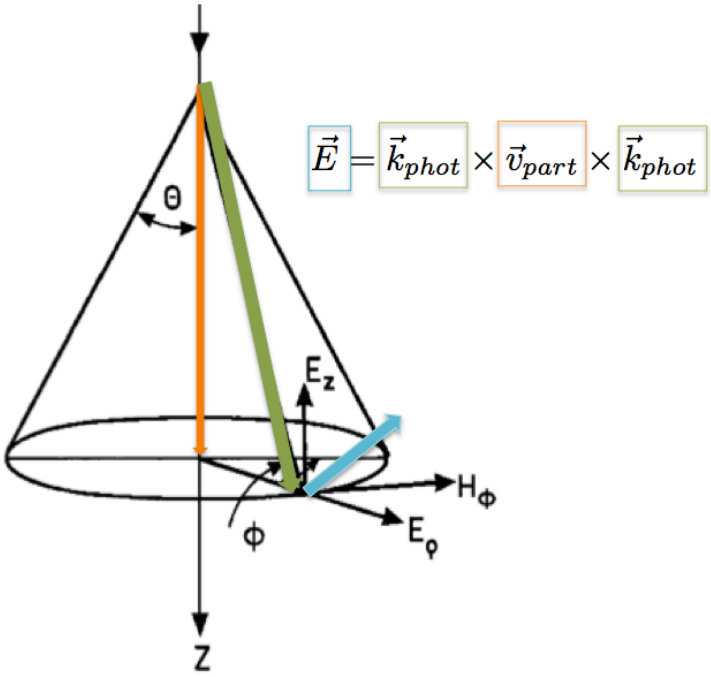

Figure 4.1: Electric field direction of a Cherenkov photon ($\vec{E}$) is defined by its wave-vector ($\vec{k}_{phot}$) and charged particle direction ($\vec{v}_{part}$) [14].

In further detail, *reflectance* is described by the fraction of the total photon energy lost for the initial medium, which can be represented as

$$R = \frac{|\vec{E}_r(\alpha_r)|^2}{|\vec{E}_i(\alpha_i)|^2} \tag{4.1}$$

where α_r is the polarization angle of the reflected wave and α_i is that of incident wave [19]. Similarly, *transmittance* results from the fraction of transmitted photon energy, described by the following expression:

$$T = \frac{|\vec{E}_t(\alpha_t)|^2}{|\vec{E}_i(\alpha_i)|^2} \tag{4.2}$$

R and *T* are quantities that have a range of values from 0 to 1.
In order to introduce the dependence on polarization, it is first necessary to evaluate the energy per unit of area that flows through the interface carried by incident, reflected and transmitted fields, which are denoted by J_i, J_r and J_t, respectively. Hence, it follows that

$$J_{pq} = S_{pq}\cos(\theta_q); \{p = \|, \perp\}; \{q = i, r, t\}[Wm^{-2}] \tag{4.3}$$

where S_{pq} is the absolute value of the Poynting vector, given by

$$S_{pq} = \frac{c}{4\pi}|\vec{E}_{pq} \times \vec{H}_{pq}| = \frac{c}{4\pi}E_{pq}H_{pq} = \frac{c}{4\pi}\sqrt{\frac{\epsilon_q}{\mu_q}}(E_{pq})^2 \tag{4.4}$$

since $\sqrt{\epsilon}_q E_{pq} = \sqrt{\mu}_q H_{pq}$.
Considering the expression 4.3 to obtain irradiance, together with Fresnel reflection coefficients (B.11-B.12), the derivation of *reflectance* for both parallel and perpendicular components results immediately from the following equations:

$$R_{\parallel} = \frac{J_r}{J_i} = \frac{|E_{\parallel r}|^2}{|E_{\parallel i}|^2} = (r_{\parallel})^2 \tag{4.5}$$

$$R_{\perp} = \frac{J_r}{J_i} = \frac{|E_{\perp r}|^2}{|E_{\perp i}|^2} = (r_{\perp})^2 \tag{4.6}$$

Using a similar procedure, *transmittance* is obtained from Fresnel transmission coefficients (B.13-B.14) as follows,

$$T_{\parallel} = \frac{J_{\parallel t}}{J_{\parallel i}} = \frac{n_2}{n_1}\frac{\mu_1}{\mu_2}\frac{\cos(\theta_t)}{\cos(\theta_i)}(t_{\parallel})^2 \tag{4.7}$$

$$T_{\perp} = \frac{J_{\perp t}}{J_{\perp i}} = \frac{n_2}{n_1}\frac{\mu_1}{\mu_2}\frac{\cos(\theta_t)}{\cos(\theta_i)}(t_{\perp})^2 \tag{4.8}$$

From the combination of expression 4.3 with 4.4, a simple expression for total energy flowing in a interface may be written as

$$J_{pi} = \frac{c}{4\pi}|E_{pi}|^2\sqrt{\frac{\epsilon_1}{\mu_1}}\cos(\theta_i) \tag{4.9}$$

which can be separated in parallel and perpendicular components as follows,

$$J_{\parallel i} = \frac{c}{4\pi}|E_{\parallel i}|^2\sqrt{\frac{\epsilon_1}{\mu_1}}\cos(\theta_i) = \frac{c}{4\pi}\sqrt{\frac{\epsilon_1}{\mu_1}}\cos(\theta_i)|E_i|^2\sin^2(\alpha_i) \tag{4.10}$$

$$J_{\perp i} = \frac{c}{4\pi}|E_{\perp i}|^2\sqrt{\frac{\epsilon_1}{\mu_1}}\cos(\theta_i) = \frac{c}{4\pi}\sqrt{\frac{\epsilon_1}{\mu_1}}\cos(\theta_i)|E_i|^2\cos^2(\alpha_i) \tag{4.11}$$

using the expression given by B.7.
Following this path, since the total incident energy flow may be rewritten as

$$J_i = \cos(\theta_i)\frac{c}{4\pi}\sqrt{\frac{\epsilon_1}{\mu_1}}|E_i|^2 \tag{4.12}$$

then 4.10 and 4.11 may have a new representation given by

$$J_{\parallel i} = J_i\sin^2(\alpha_i) \tag{4.13}$$

$$J_{\perp i} = J_i\cos^2(\alpha_i) \tag{4.14}$$

Therefore, it becomes clear that

$$R = \frac{J_r}{J_i} = \frac{J_{\parallel r} + J_{\perp r}}{J_i} = \frac{J_{\parallel r}}{J_{\parallel i}}\sin^2(\alpha_i) + \frac{J_{\perp r}}{J_{\perp i}}\cos^2(\alpha_i) \tag{4.15}$$

which shows that the reflectance dependence on incident polarization angle α_i is more simply described by

$$R(\alpha_i) = R_{\parallel} \sin^2(\alpha_i) + R_{\perp} \cos^2(\alpha_i) \tag{4.16}$$

and conversely transmittance is described by

$$T(\alpha_i) = T_{\parallel} \sin^2(\alpha_i) + T_{\perp} \cos^2(\alpha_i) \tag{4.17}$$

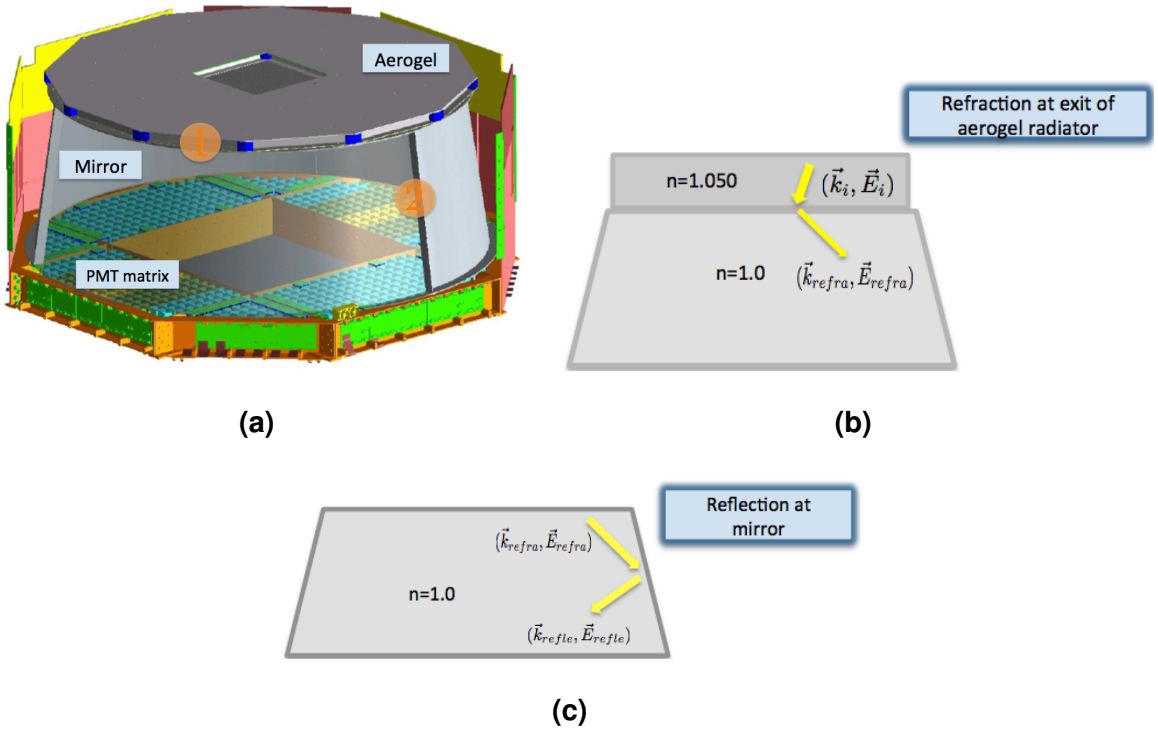

Figure 4.2: a) 3-D scheme of RICH detector. b)2-D scheme of Cherenkov propagation crossing the radiator boundary and being refracted (1). c) 2-D scheme of Cherenkov photon propagation being reflected at mirror (2).

Unpolarized light

For unpolarized light, $\vec{E}$ varies very rapidly in an arbitrary or irregular manner, which means that no particular direction is given preference. Therefore, the overall reflectance $\overline{R}$ comes from averaging over all directions α. Considering that the average value of both $\sin^2(\alpha)$ and $\cos^2(\alpha)$ is $\frac{1}{2}$, it follows from 4.12 that

$$\overline{J}_{\parallel i} = J_i \overline{\cos^2(\alpha_i)} = \overline{J}_{\perp i} = J_i \overline{\sin^2(\alpha_i)} = \frac{1}{2} J_i \tag{4.18}$$

Similarly, the reflected components are given by

$$\overline{J}_{\parallel r} = \frac{\overline{J}_{\parallel r}}{\overline{J}_{\parallel i}}\overline{J}_{\parallel i} = \frac{\overline{J}_{\parallel r}}{\overline{J}_{\parallel i}}\frac{1}{2}J_i = \frac{1}{2}r_{\parallel}^2 J_i \tag{4.19}$$

$$\overline{J}_{\perp r} = \frac{\overline{J}_{\perp r}}{\overline{J}_{\perp i}}\frac{1}{2}J_i = \frac{1}{2}r_{\perp}^2 J_i \tag{4.20}$$

The average reflectance is given by

$$\overline{R} = \frac{\overline{J}_r}{\overline{J}_i} = \frac{\overline{J}_{\parallel r} + \overline{J}_{\perp r}}{\overline{J}_i} = \frac{\overline{J}_{\parallel r}}{2\overline{J}_{\parallel i}} + \frac{\overline{J}_{\perp r}}{2\overline{J}_{\perp i}} = \frac{1}{2}(r_{\parallel}^2 + r_{\perp}^2) \tag{4.21}$$

Similarly, the average transmittance is expressed as

$$\overline{T} = \frac{1}{2}(t_{\parallel}^2 + t_{\perp}^2) \tag{4.22}$$

4.2.1 Mirror reflection

The RICH's mirror is coated with a conductor metal (aluminium) over a substract of silica (SiO_2). Given the material finite conductivity σ there will be energy losses in the media. Since the electromagnetic is considered for simplicity a complex wave function, thereby the photon energy absorption will be mathematically described by a complex refractive index value as follows [18]:

$$n_m = \sqrt{1 + i\left(\frac{\sigma}{\epsilon_0 \omega}\right)} = n_R + i n_I \tag{4.23}$$

$$\implies n_m^2 = 1 + i\left(\frac{\sigma}{\epsilon_0 \omega}\right) = n_R^2 - n_I^2 + i2 n_R n_I \tag{4.24}$$

where n_I is the imaginary part and n_R corresponds to the real part.
Solving for the real and imaginary components, it follows that

$$n_R^2 - n_I^2 = 1 \tag{4.25}$$

$$2 n_R n_I = \frac{\sigma}{\epsilon_0 \omega} \implies n_R = \frac{\sigma}{2\epsilon_0 \omega n_I} \tag{4.26}$$

which leads to

$$n_I^4 - n_I^2 - \left(\frac{\sigma}{2\epsilon_0 \omega}\right)^2 = 0 \tag{4.27}$$

Hence, it can be obtained from the quadratic equation 4.27 that

$$n_I^2 = \frac{1 \pm \sqrt{1 + 4\left(\frac{\sigma}{2\epsilon_0 \omega}\right)^2}}{2} \implies n_I^2 = \frac{1 + \sqrt{1 + 4\left(\frac{\sigma}{2\epsilon_0 \omega}\right)^2}}{2} \tag{4.28}$$

Since n_I is a real number, the positive solution must be chosen.
Inserting the complex refractive index back into the electric field expression given by (4.26), it follows easily that

$$\vec{E}(\vec{x},t) = \vec{E}_0 e^{(\vec{k}\cdot\vec{x}-wt)} \tag{4.29}$$

$$= \vec{E}_0 e^{i(n_R+in_I)\frac{\omega}{c}(\vec{u}_k\cdot\vec{x})-i\omega t} \tag{4.30}$$

$$= \vec{E}_0 \overbrace{e^{i\omega(\frac{n_R}{c}\vec{u}_k\cdot\vec{x}-t)}}^{Oscillatory\ term} \overbrace{e^{-\frac{n_I\omega}{c}\vec{u}_k\cdot\vec{x}}}^{Absorption\ term} \tag{4.31}$$

The first exponential term basically describes an electromagnetic wave that propagates with a velocity of c/n_R.The second one leads to photon absorption in metals due to inducing a current in the medium. As a result, there will be a decline of irradiance (*I* [W/m^2]) as the wave propagates through the medium, i.e., the photon energy lost per unit of area, which is described by following expression:

$$I = \vec{E}\cdot\vec{E}^* = \vec{E}_0\cdot\vec{E}_0^* e^{-\frac{2n_I\omega(\vec{u}_k\cdot\vec{x})}{c}} \tag{4.32}$$

$$= I_0 e^{-\frac{2n_I\omega(\vec{u}_k\cdot\vec{x})}{c}} = I_0 e^{-\delta(\vec{u}_k\cdot\vec{x})} \tag{4.33}$$

whereas the absorption coefficient is defined as

$$\delta = \frac{2n_I\omega}{c} = \frac{4\pi n_I}{\lambda} \tag{4.34}$$

The reflectance from metals comes from the imaginary part n_I of the refractive index, which regards the electromagnetic wave energy losses in the metal. Hence, the global picture comes out when n_m is plugged into the Fresnel reflection coefficients (B.11-B.12) as follows:

$$r_{\perp mirr} = \frac{\cos\theta_i - \sqrt{n_m^2 - \sin^2(\theta_i)}}{\cos\theta_i + \sqrt{n_m^2 - \sin^2(\theta_i)}} \tag{4.35}$$

$$r_{\parallel mirr} = \frac{-n_m^2\cos(\theta_i) + \sqrt{n_m^2 - \sin^2(\theta_i)}}{n_m^2\cos\theta_i + \sqrt{n_m^2 - \sin^2(\theta_i)}} \tag{4.36}$$

Replacing expression (4.24) in (4.35-4.36), the reflection coefficients at mirror are given by

$$r_{\perp mirr} = \frac{\cos\theta_i - \sqrt{(n_R^2 - n_I^2 - \sin^2(\theta_i)) + i(2n_Rn_I)}}{\cos(\theta_i) + \sqrt{(n_R^2 - n_I^2 - \sin^2(\theta_i)) + i(2n_Rn_I)}} \tag{4.37}$$

$$r_{\parallel mirr} = \frac{-((n_R^2 - n_I^2) + i(2n_Rn_I))\cos\theta_i + \sqrt{(n_R^2 - n_I^2 - \sin^2(\theta_i)) + i(2n_Rn_I)}}{((n_R^2 - n_I^2) + i(2n_Rn_I))\cos(\theta_i) + \sqrt{(n_R^2 - n_I^2 - \sin^2(\theta_i)) + i(2n_Rn_I)}} \tag{4.38}$$

From expression (4.41-4.42) follows that Fresnel reflection coefficients will have a complex component.

Therefore, the conventional geometrical interpretation for non-dissipative media, where the reflection coefficients are real. Instead, a new approach should be taken by considering complex component is due to photon energy loss in the boundary interface of the conductor. In further detail, the idea behind the complex refractive index derives from the complex-valued wave vector, e.g., $\vec{k} = \vec{\beta} - i\vec{\alpha}$, which shows that the angle of refraction becomes complex-valued (since $\vec{k} \propto \frac{1}{\lambda}\vec{u}_k$). The physics is thereby obtained through the square absolute value of (4.41-4.42), which basically represents the energy flux ratio of incident and reflected waves. Similarly to expressions (4.5-4.6), it follows

$$R_{\perp mirr} = |r_{\perp mirr}|^2 \tag{4.39}$$

$$R_{\parallel mirr} = |r_{\parallel mirr}|^2 \tag{4.40}$$

where $|r_{\perp mirr}|^2$ and $|r_{\parallel mirr}|^2$ are given by:

$$|r_{\perp mirr}|^2 = \frac{|\cos(\theta_i) - x_R|^2 + |x_I|^2}{|\cos(\theta_i) + x_R|^2 + |x_I|^2} \tag{4.41}$$

$$|r_{\parallel mirr}|^2 = \frac{|(n_I^2 - n_R^2)\cos(\theta_i) + x_R|^2 + |-2n_R n_I \cos(\theta_i) + x_I|^2}{|(n_R^2 - n_I^2)\cos(\theta_i) + x_R|^2 + |-2n_R n_I \cos(\theta_i) + x_I|^2} \tag{4.42}$$

Using the expression (4.16) to determine the polarized reflectance at the mirror, it results that

$$R_{mirr} = |r_{\perp mirr}|^2 \cos^2(\alpha_{mirr}) + |r_{\parallel mirr}|^2 \sin^2(\alpha_{mirr}) \tag{4.43}$$

where α_{mirr} is the angle between the polarization vector of incident photons and the normal to the mirror surface (see Figure B.2). For instance, expression for unpolarized reflectance is given by

$$R_{mirr} = \frac{|r_{\perp mirr}|^2 + |r_{\parallel mirr}|^2}{2} \tag{4.44}$$

In order to apply this procedure to AMS-02 events, it is necessary to find the two key parameters: n_I and n_R. To obtain these results, it is necessary to solve quadratic equation 4.43 in order to obtain n_I and n_R. Following this path, becomes essential to performe an approximation where the photon wavelength has a fixed value at $\lambda = 420$ nm, since reflectance is almost independent of this variable. Following this, the only free parameter is the mirror conductivity σ, which according to the previous basic ideas is evaluated as $\sigma = 1.638.10^7$S/m. From this last statement and from expression (4.28) follows that n_I and n_R are given, respectively, by

$$n_I \simeq 25.46 \tag{4.45}$$

$$n_R \simeq 50.88 \tag{4.46}$$

Finally, regarding results obtained from expressions (4.45-4.46), the functions for unpolarized and polarized reflectance resulting from expressions (4.44) and (4.43), respectively, are plotted as function photon incident angle at the mirror (θ_{mirr}) in figure 4.3.

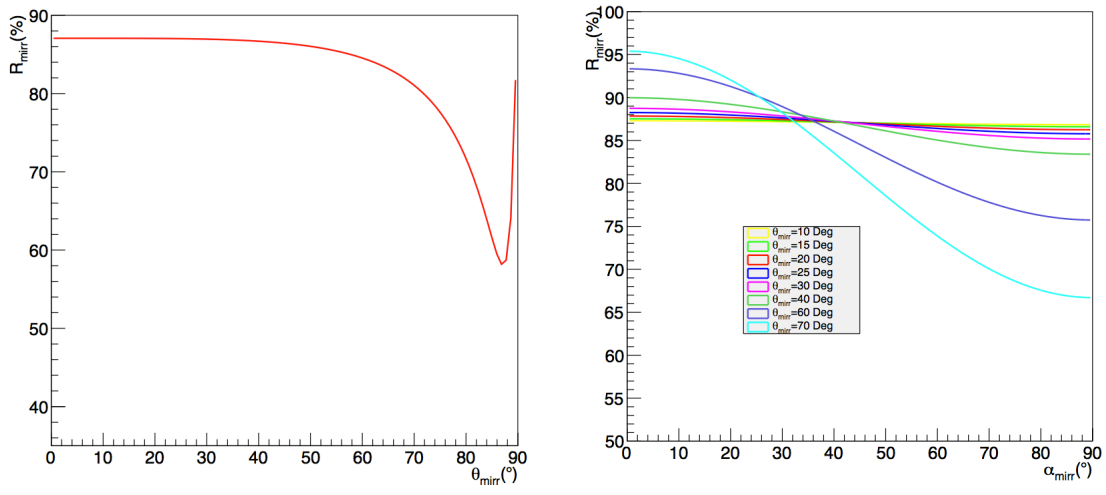

(a) **(b)**

Figure 4.3: a) Dependence of unpolarized reflectance at mirror on incident theta at mirror θ_{mirr}. b)Dependence of polarized reflectance at mirror on incident photon's polarization angle at mirror α_{mirr}[20].

4.3 Implication of Cherenkov polarization on efficiency

In section (4.2), the main processes and features of CK photon energy loss due to polarization effect were described. From this point, the next step is evaluating the effect according to the RICH geometry and material properties such as aerogel/NaF radiators ($n_{index} \in \{1.050, 1.334\}$) or mirror surface.
Following this path, there will be two main photon interactions listed as follows (see figures 4.2(b) and 4.2(c)):

- Refraction at the radiator-air boundary;
- Reflection at the mirror.

Since each interface corresponds to an energy loss factor for each Cherenkov photon (indexed by the letter **i**) according to its polarization, it is necessary to evaluate the size of the effect. Therefore, the *transmittance at radiator* (NaF/aerogel) T_i^{rad} and reflectance at mirror R_i^{mirr} should be evaluated. Putting together both effects,

the expression describing Cherenkov polarization correction factor for each photon follows:

$$\varepsilon_i^{cer} = \frac{T_i^{rad} R_i^{mirr}}{R_{mirr}^0} \tag{4.47}$$

Since the current LIP algorithm only regards a reflectance independent of photon incident and polarization angle at mirror, the CK polarization correction will be applied over the reference value $R_{mirr}^0 = 0.85$.
In addition, another motivation factor to study the Cherenkov polarization effect comes from the photon resolution detection upgrade at PMT matrix through the implementation of a new computational model (this procedure is described in chapter 3).
This new feature allows to deepen the study about photon intrinsic properties such as Cherenkov polarization.
On the other hand, Cherenkov photon's incident angle in the radiator (see appendix section A) depends on the charged particle's incident angle θ_{part} (figure 4.4), which means that polarization angle α will also be modified, leading to T_i^{rad} and R_i^{mirr} transformation (see section 4.2). For this reason, Cherenkov polarization efficiency ε^{cer} may be correlated with θ_{part}.
Therefore, the study of Cherenkov polarization effect will include the following topics:

- ε_i^{cer} dependence on θ_{part} (see figure 4.5(a) and 4.5(b), respectively);
- Study the average Cherenkov efficiency within steps of $\theta_{part} = 1.25^\circ$ (within the RICH acceptance);
- Get the dispersion of Cherenkov factor ($\sigma_{\varepsilon_{cer}}$) for last topic distributions;
- Correlation between $\sigma_{\varepsilon_{cer}}$ and θ_{part} (particle incidence angle distribution is shown in figure 4.4, respectively).

4.3.1 Dependence with the charged particle's incident angle

In order to estimate the Cherenkov polarization effect, a Monte Carlo simulation was developed, where 10^6 charged particles were generated within RICH acceptance. Each particle will generate a Cherenkov ring of 360 equally spaced photons along the azimuthal angle (φ) in its reference frame (i.e., one Cherenkov photon per degree). Adding these facts to the consideration in the beginning of the section, the first step is evaluating the Cherenkov polarization factor (ε_{cer}) dependence on the charged particle's incidence angle (θ_{part}). In further detail, looking at aerogel events (figure 4.5(a)), there are two featured regions ε_{cer} variations, described as follows:

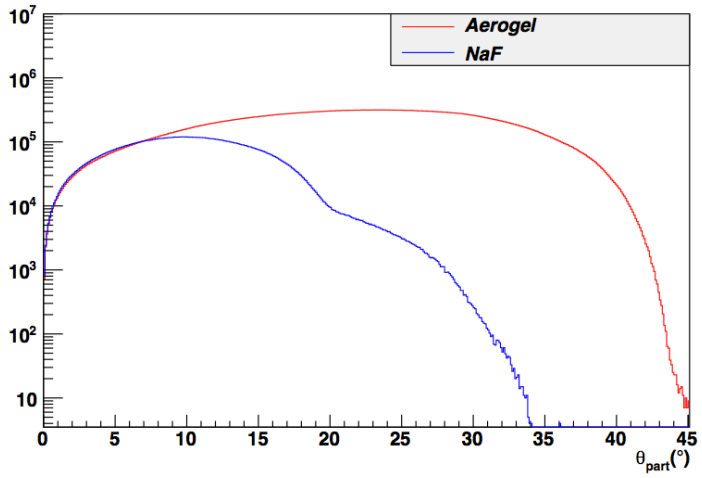

Figure 4.4: Charged particle's incident angle θ_{part} distribution for RICH reconstructed events.

- within the θ_{part} region from 0^0 to 25^0, there is a tail-like curve describing a Cherenkov efficiency variation from ~ 0.82 to ~ 0.98;
- zooming over the region $\varepsilon_{cer} \in [0.86, 0.98]$ (see figures 4.5(a) and 4.5(b)) , a variation through all θ_{part} range can be seen.

On the other hand, in NaF events (figure 4.5(b)), there are three main regions to study, as follows:

- a variation of ε_{cer} following a curve going upwards from 0.6 to 0.98, within the $\theta_{part} \in [1, 5]^0$ region;
- there is also a remarked change of Cherenkov factor from 0.94 to approximetaly 0.97, for $\theta_{part} \in [15, 30]^0$;
- looking at $\theta_{part} \in [5, 35]^0$ there is a second profiled region for Cherenkov factor values between 0.96 and 0.99.

From this point, it is safe to state the following conclusion: Cherenkov polarization factor ε_{cer} depends on incident charged particle angle θ_{part}. The Cherenkov factor should, then, be studied for several different values of θ_{part}. For this purpose, the particle's theta spectrum was divided into $\theta_{part} = 1.25^0$ size slices.
Applying the projection over θ_{part} variable for both NaF and Aerogel events, a profile distribution in ε_{cer} variable is obtained. For instance, choosing a θ_{part} range within the range $[5.00, 6.25]^0$, the resulting projection is given by figure 4.6. Regarding figure (4.6), there are obvious features for both aerogel and NaF events:

- spreading tails;

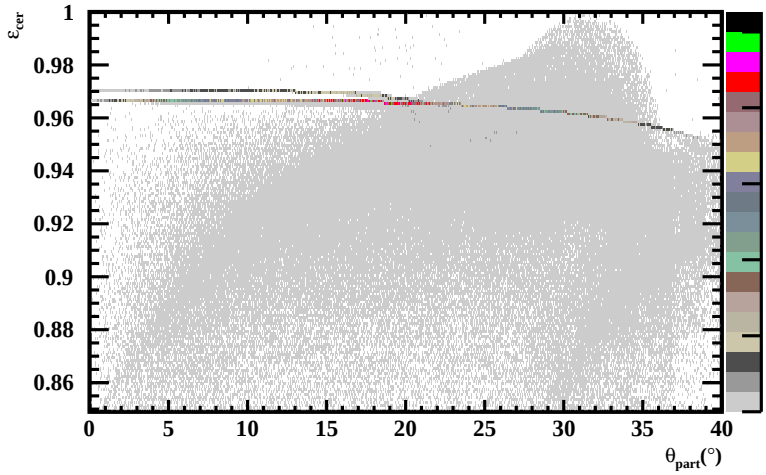

(a)

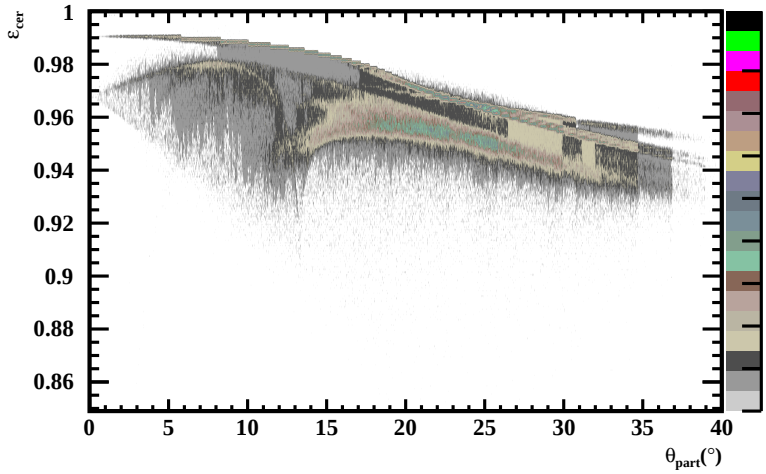

(b)

Figure 4.5: Dependence of ε^{cer} on θ_{part} for aerogel (a) and NaF (b) events.

- double peaks.

The two behaviours described before may be understood by decoupling the mirror and radiator effects. Similarly to total effect factor, reflectance at mirror and transmittance at radiator will have a θ_{part} dependence. Therefore, a $T_{rad}(\theta_{part})$ and $R_{mirr}(\theta_{part})$ projection distribution should be obtained for every θ_{part} slice (figure 4.7(a) and 4.7(b) shows the a projection distribution for $\theta_{part} = [5.00, 6.25]^{\circ}$, respectively). From figures 4.7(a) and 4.7(b), respectively, it follows that R_{Mirr} distribution has a large width for both aerogel and NaF events. Conversely, T_{rad} distribution is narrow for aerogel events and it spreads for NaF events.
Although, in order to have a deep understanding of both effects is necessary to evalu-

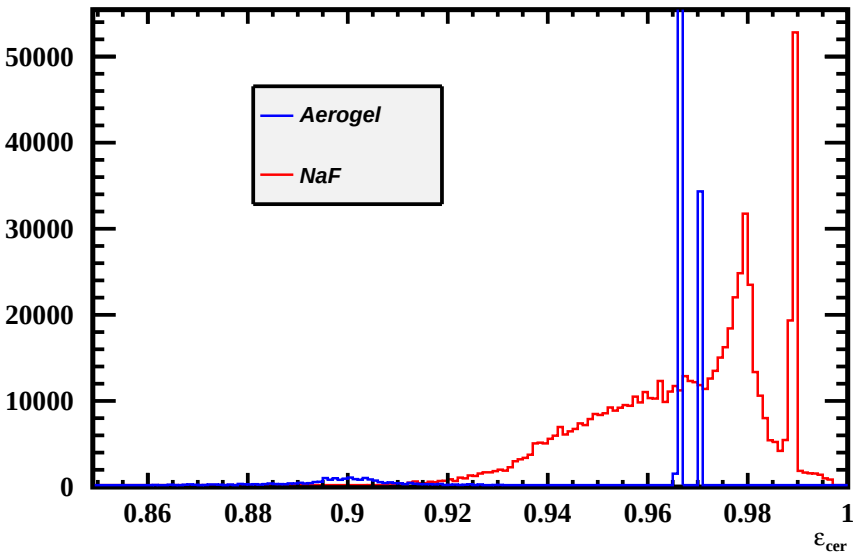

Figure 4.6: ε_{cer} distribution for particles with polar angles in the range $[5, 6.25]^0$ impacting in aerogel and NaF radiators.

ate the following statistical measurements resulting from figures (4.7(b)) and (4.7(a)), respectively:

- Distribution width ($\sigma_{T_{rad}}/\sigma_{R_{mirr}}$);
- Distribution average($< T_{rad} > / < R_{mirr} >$) for every θ_{part}.

The comprehension of reflectance at mirror effect relies on the study of the two following features:

- Ratio of distribution width $\sigma_{R_{Mirr}}(\theta_{part})$ by average mirror reflectance distribution $< R_{Mirror} > \left(\frac{\sigma_{R_{Mirr}}}{<R_{Mirror}>}\right)$;
- Average value $< R_{Mirror} > (\theta_{part})$.

Regarding aerogel events with photons in the mirror, the probability of hitting the mirror increases for larger incident angles at mirror (see figure 2.16), where the photon reflectance suffers a deep variation (see figure 4.3). In addition, reflectance also changes more significantly for larger θ_{mirr} due to the lower aerogel's refractive index value, i.e., the angle resulting from refraction is similar to the incident one ($\theta_i \simeq \theta_{refrac}$).
In further detail, figure 4.8(b) shows the mean reflectance at mirror value per particle's polar angle range center, i.e., for a slice of $\theta_{part} \in [1.25, 2.5]^\circ$ the center is given by $\theta_{part} = \frac{1.25+2.5}{2} \simeq 1.875^\circ$ (for both aerogel and NaF radiators, respectively). For instance, for aerogel events the average R_{Mirr} grows from 0.5 to 0.82 within a particle's

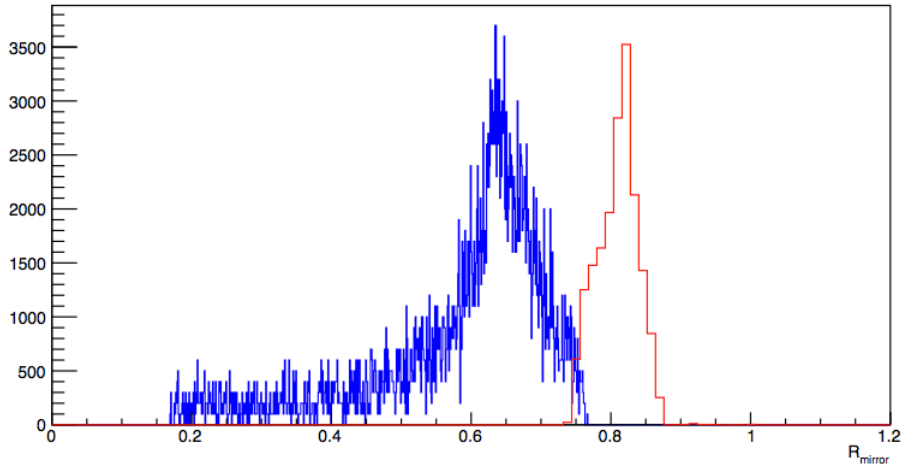

(a)

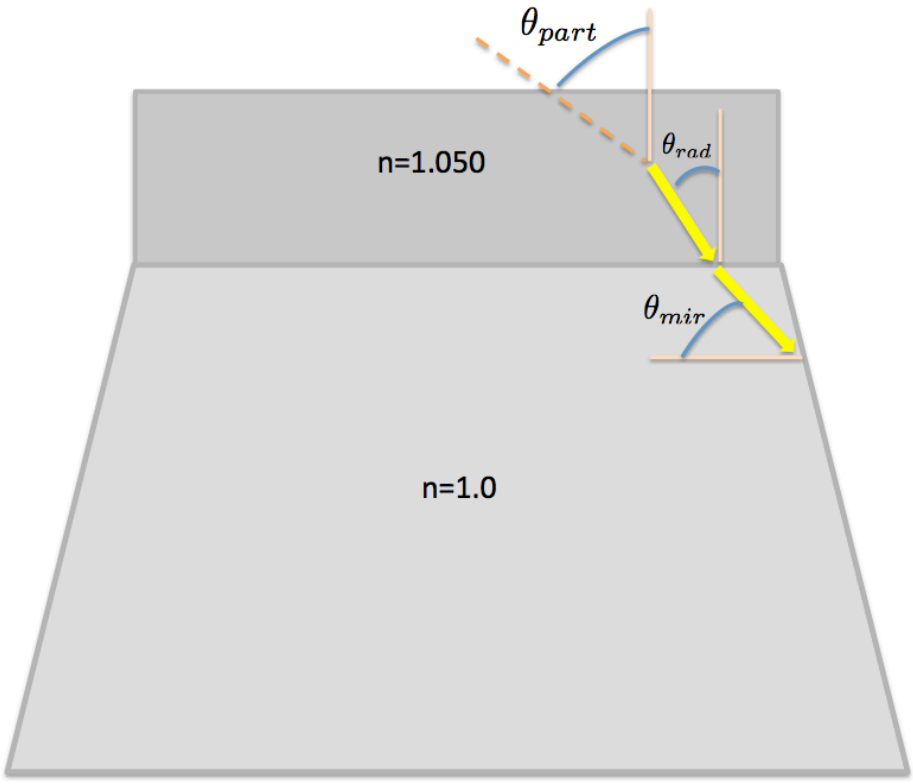

(b)

Figure 4.7: a) Distribution for reflectance at mirror $\theta_{part} \in [5.00, 6.25]^0$. b) Schema of charged particle (dashed line) emission of Cherekov photons (yellow line), which are being propagated to the mirror.

polar angle range $[0, 25]^\circ$, while for NaF events the value is approximately constant and equal to $R_{Mirr} \simeq 0.82$. Although, the final conclusion about *mirror effect* comes from the relative error $\frac{\sigma_{R_{Mirr}}}{<R_{Mirror}>}$ as function of the particle polar angle, described in figure 4.8(a). The figure analysis allows to state:

- Evaluating the aerogel events, the relative error grows linearly with particle's polar angle until 16% ($\theta_{part} \simeq 7.25^\circ$) and decreases to a minimum of 7% at $\theta_{part} \simeq 28.75^\circ$, where it remains constant at $\frac{\sigma_{R_{Mirr}}}{<R_{Mirror}>} = 7\%$ for the rest of θ_{part} range. From this data together with plot 4.8(b) which shows the mirror reflectance as function of the polar angle fir aerogel and NaF simulated events, it is possible to conclude that systematic error is more significant within the following particle's theta range: $\theta_{part} = [2.5, 29]^\circ$. Particle's theta spectrum, shown in figure 4.4 is more populated in the region around 20^0. Furthermore, figures 2.16(a) and 4.3(a) strengthen the idea of great variations in reflectance at mirror for aerogel events.

- Since $< R_{Mirr} > \simeq 82\%$ for all the particle's theta range for NaF events, therefore from figure 4.8(a) is clear the growth of systematic error linearly with particle's theta, for $\theta_{part} < 30^\circ$, to a maximum of $\sim 12\%$.

Similarly to mirror effect study, for the transmittance at radiator factor there are two essential plots to consider: transmittance relative error $\frac{\sigma_{T_{Rad}}}{<T_{Rad}>}(\theta_{part})$ at radiator; mean transmittance at radiator $< T_{Rad}(\theta_{part}) >$. From figure 4.10(b) it can be seen that NaF events have a much larger variation of $< T_{Rad} >$ than aerogel events. Nevertheless, in order to evaluate the size of Cherenkov polarization effect at radiator, the next step is evaluating the relative error $\frac{\sigma_{T_{Rad}}}{<T_{Rad}>}$ as function of the particle's incidence angle θ_{part}.Thus, the observation of figure 4.10(a) gives three additional informations about the radiator effect, described as follows:

- The fluctuation of relative error for aerogel events ($\sim 0.5\%$) has no statistical relevance. In addition, since the average transmittance at aerogel exit is approximately constant through the particle's polar angle spectrum, the systematic error has a small relative importance.

- In NaF events, there is a relative error variation from 3.5% to 1.1% within $\theta_{part} \in [0^\circ, 8^\circ]$, which is an effect of the average transmittance at radiator $< T_{rad}(\theta_{part}) >$ value oscillation. For $\theta_{part} > 18^\circ$ the NaF radiator effect loses the importance with $\frac{\sigma_{T_{Rad}}}{<T_{Rad}>} < 1\%$.

- Figure 4.10(b) shows the radiator transmittance has relevance for NaF events having $\theta_{part} < 18^\circ$.

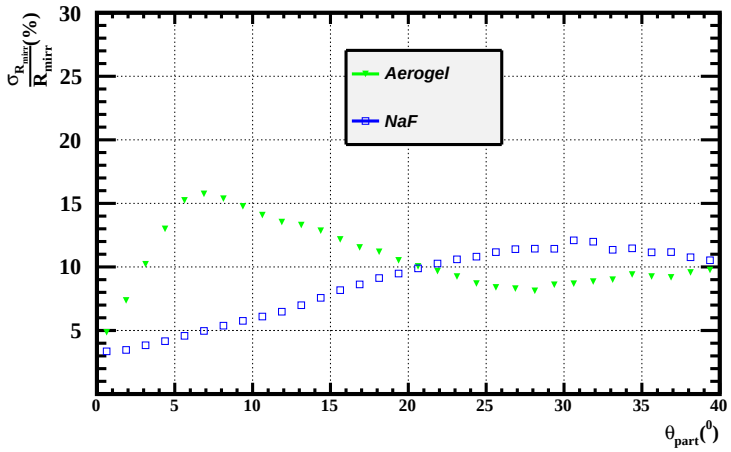

(a)

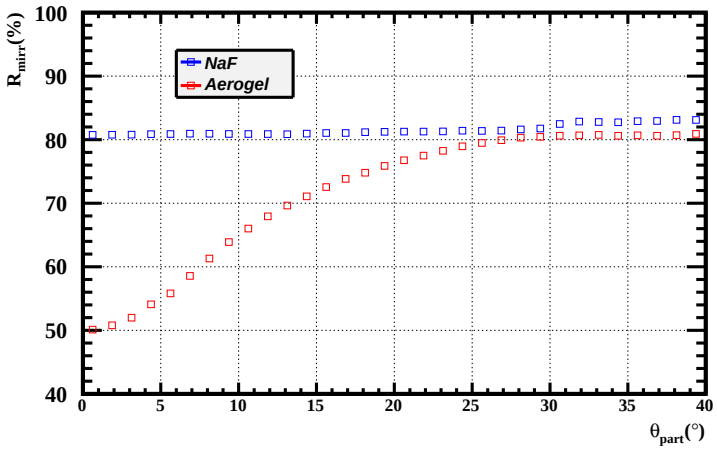

(b)

Figure 4.8: a) $\frac{\sigma_{R_{Mirr}}}{<R_{Mirror}>}$ versus particle polar angle (θ_{part}). b) Mean reflectance $< R_{Mir} >$ versus particle polar angle (θ_{part}).

After studying both radiator and mirror effects separately, the next step is evaluating the behaviour of the integrated result (see expression 4.47) as function of particle incidence angle. Repeating the radiator/mirror effect analysis, figures 4.11(a) and 4.11(b) are obtained, showing an estimation of Cherenkov polarization average effect for aerogel and sodium fluoride events, respectively.

For instance, in the aerogel case, there is now an explanation for the declining of Cherenkov polarization efficiency $< \varepsilon_{cer} >$ for particle polar angle angles greater than $20°$, which results from the variation of reflectance at mirror.

On the other hand, in the NaF case approach to $< \varepsilon_{cer} >$ behaviour is completely different, since the bump within the range $\theta_{part} \in [2.5, 10.0]°$ is due to T_{rad} oscillation.

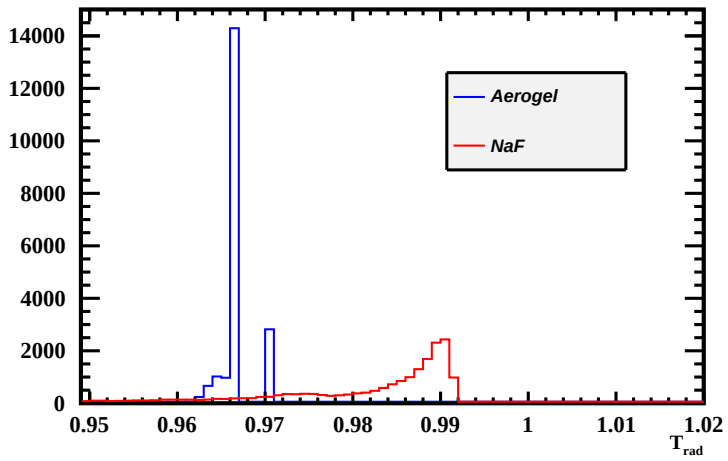

Figure 4.9: Distribution of transmittance at radiator for $\theta_{part} \in [5.00, 6.25]^{\circ}$.

Furthermore, the reduction for $\theta_{part} > 10^{\circ}$ is also due to the reduction in radiator transmittance.

Finally, the evaluation of total polarization effect results from studying the relative systematic error of the Cherenkov polarization factor, i.e., the ratio between $\sigma_{\varepsilon_{cer}}$ and $< \varepsilon_{cer} >$. The Cherenkov polarization effect was only considered just for polarization factor. However, the other two possibilities, described as follows,

- The unpolarized effect (which does not depend on polarization angle) depending on particle polar angle θ_{part} ;
- The expected correction relating efficiency factor for polarization and unpolarized case according to the following expression: $\frac{\varepsilon_{cer}^{POL}}{\varepsilon_{cer}^{UNPOL}}$.

were also studied as an academic purpose. Figure 4.13 describes the relative error $\frac{\sigma_{\varepsilon_{cer}}}{<\varepsilon_{cer}>}$ for both aerogel and NaF events as function of particle polar angle θ_{part}. The magnitude of Cherenkov polarization effect can be obtained from figure 4.13 and three main conclusions follow:

- The relative error for aerogel events is approximately 3% for $\theta_{part} \in [0^{\circ}, 5^{\circ}]$ and $\theta_{part} \in [30, 35]^{\circ}$. For others parts of the particle polar angle θ_{part} spectrum, $\frac{\sigma_{\varepsilon_{cer}}}{<\varepsilon_{cer}>} \simeq 2\%$.
- Regarding relative error for NaF events, the value is nearly constant over all particle's polar angle range and equal to $\sim 2.5\%$.
- The effect will be sizable and about 3% for aerogel events within certain particle polar angle θ_{part} regions (see figure 4.4). On the other hand, for NaF events the effect will also be significant and about 2.5% for the whole θ_{part} domain.

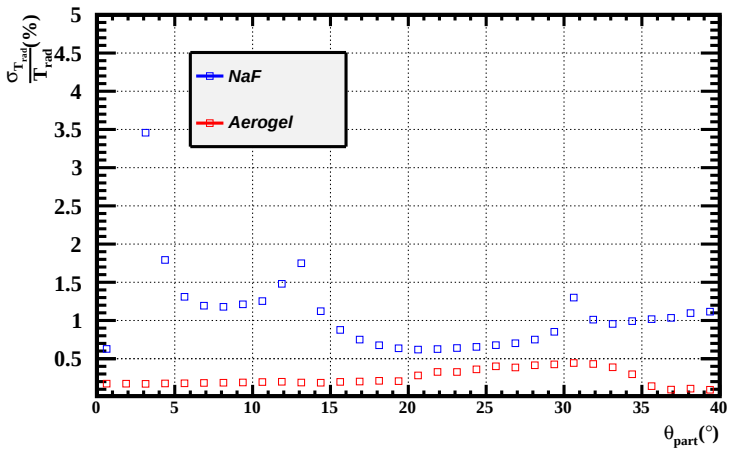

(a)

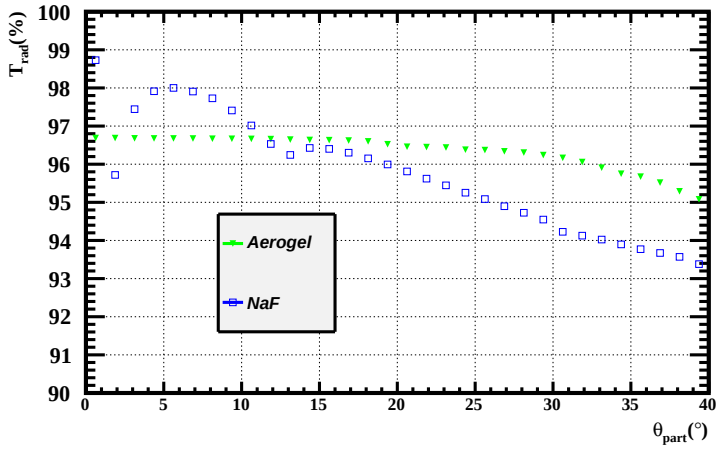

(b)

Figure 4.10: a) $\frac{\sigma_{T_{Rad}}}{<T_{Rad}>}$ versus θ_{part}. b) $< T_{Rad} >$ versus θ_{part}.

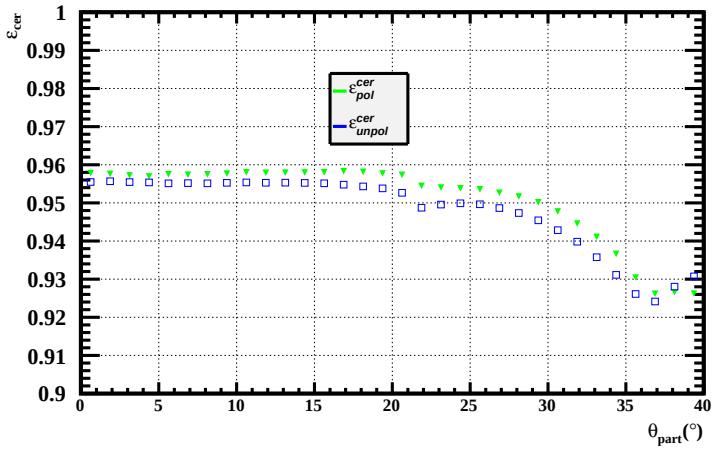

(a)

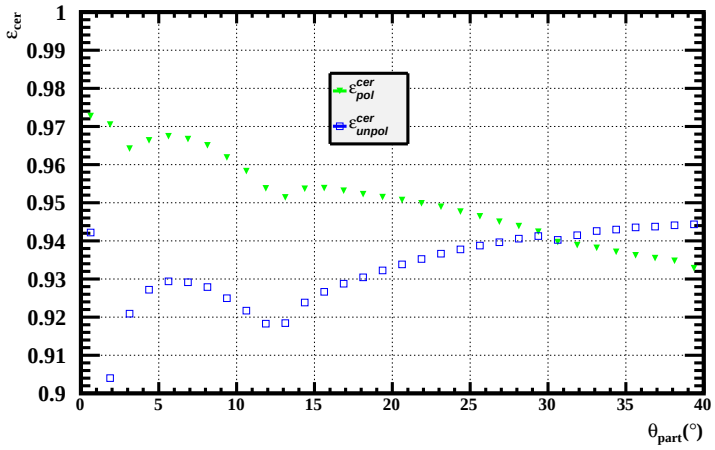

(b)

Figure 4.11: Mean Cherenkov factor value ($< \varepsilon_{cer} >$) as function of charged particle polar angle θ_{part} for aerogel (a) and NaF (b) events.

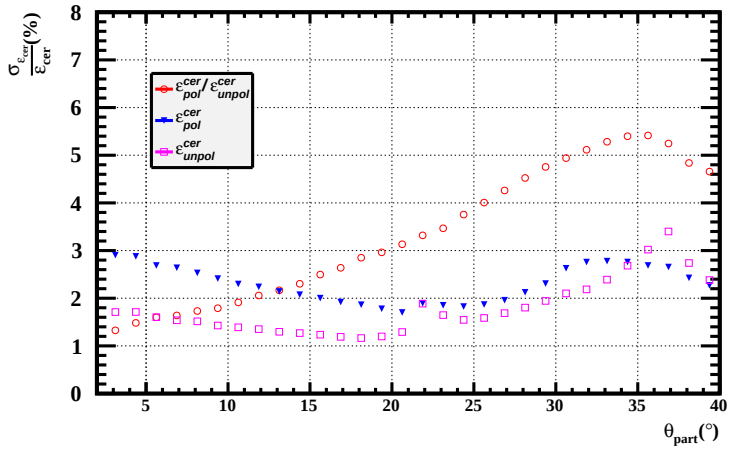

(a)

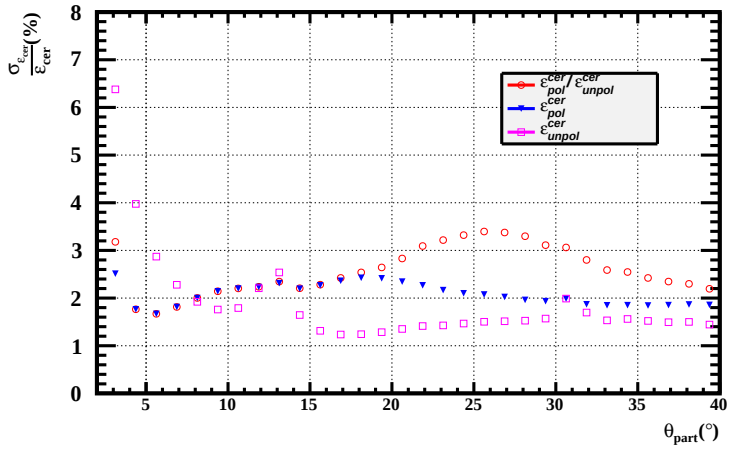

(b)

Figure 4.12: a) Cherenkov polarization factor $\sigma_{\varepsilon_{cer}}$ versus θ_{part} (aerogel events). b) $\sigma_{\varepsilon_{cer}}$ versus θ_{part} (NaF events)

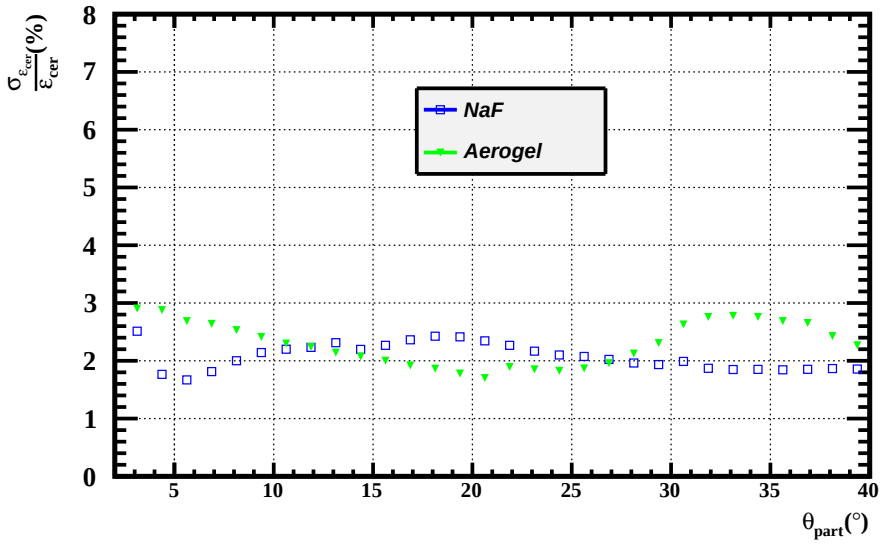

Figure 4.13: $\frac{\sigma_{\varepsilon_{cer}}}{<\varepsilon_{cer}>}$ versus θ_{part} for aerogel and NaF events.

5

Cherenkov polarization bias in RICH charge reconstruction

Contents

5.1 Introduction to Cherenkov polarization effect in RICH ring efficiency

The procedure to insert Cherenkov polarization factor in charge reconstruction follows a similar procedure as refered in section 3.3, whereas the ring efficiency results from the factorization of several effects such as Rayleigh scattering at radiator or LG signal collection. These known effects are described by expression 3.35, which depends on pixel types (see figure 3.8).
On the other hand, as mentioned in section 4.3, the transmittance at radiator and reflectance at mirror, according to the LIP algorithm, are described as follows:

$$T_{Rad}^{(0)} = \begin{cases} 1 & , radiator - air \\ 0 & , otherwise \end{cases} \tag{5.1}$$

$$R_{Mirr}^{(0)} = \begin{cases} 0.85 & , reflected\ photon \\ 1 & , direct\ photon \end{cases} \tag{5.2}$$

This results in a slightly different for ring efficiency, given by:

$$\varepsilon_{(0)}^{ring} = \frac{1}{2\pi H_{rad}} < \varepsilon_{PMT} > T_{Rad}^{(0)} \sum_{j}^{N_{pixel}} \sum_{i}^{N_{seg}} \left(\varepsilon^{LG} \varepsilon_{Wall} \right)_{i} \varepsilon_{j}^{acc} \tag{5.3}$$

Then, in order to add the CK polarization effect, it is just necessary to replace expressions (5.1) and (5.2) by the equations (4.17) and (4.43), respectively. In further detail, the inclusion of the previous terms will be evaluated pixel by pixel, i.e., since each pixel will detect photon with different incident angle, this means the reflectance at mirror and transmittance at radiator will change their value. As a result, the ring efficiency after applying the Cherenkov polarization effect is given by:

$$\varepsilon_{(1)}^{ring} = \frac{1}{2\pi H_{rad}} < \varepsilon_{PMT} > \sum_{j}^{N_{pixel}} \sum_{i}^{N_{point}} \left(\varepsilon^{LG} \varepsilon_{Wall} \right)_{j} \varepsilon_{j}^{acc} T_{Rad\ j}^{(1)} \tag{5.4}$$

where

$$\varepsilon_{j}^{acc} = \frac{\sum_{i}^{N_{seg}} P_{i\ j}}{\sum_{i,j} P_{i\ j}} (R_{Mirr\ j}^{(1)})^{n_{refl}} \equiv R^{n_{refl}} \frac{\sum_{i} P_{i\ j}}{N_{point}} (R_{Mirr\ j}^{(1)})^{n_{refl}} \tag{5.5}$$

and $R_{Mirr\ j}^{(1)} / T_{Rad\ j}^{(1)}$ correspond to the replacements of expressions (5.2) and (5.1), respectively.

5.2 Charge correction by CK polarization factor

In this section, the CKfactor correction on RICH charge reconstruction will be studied. The following topics will be covered:

- Presentation of the following concepts: *Time-Dependent* and *Time-Independent* correction;
- Evaluation of RICH charge (Z) distribution peaks resulting from RICH charge reconstruction;
- Study of charge peak width (σ_Z) and systematic error.

5.2.1 Charge calculation

Given the ring's full efficiency result for the event, the total ring signal as shown in figure 5.1 (i.e. the sum of signals $n_{pe}(k)$ for all *k* hits tagged as being part of the CK ring), the particle's velocity β and its incident angle θ_{part} (which determines the traversed radiator length), the particle charge *Z* is obtained from the following expression:

$$Z^2_{(1)} = \left(\frac{\beta^2 n^2 - 1}{\beta^2 n^2 - \beta^2} \frac{\cos(\theta_{part})}{N_0} \right)^2 \frac{\sum_{k=1}^{N_{hits}} n^{(1)}_{pe}(k)}{\varepsilon^{ring}_{(1)}(event)} \tag{5.6}$$

where $\varepsilon^{ring}_{(1)}$ is the Cherenkov polarization efficiency correction (see equation 5.4) and N_0 is the global charge normalization factor, defined as the expected number of visible photons for an idealized event with perpendicular incidence, $\beta = 1$ and $Z = 1$, having no loss of light from emission to the PMT window and falling on an idealized matrix with no dead areas.
For convenience, expression 5.6 may be rewritten as follows:

$$Z^2_{(1)} = N^2(\beta, \theta_{part}) \frac{\sum_{k=1}^{N_{hits}} n^{(1)}_{pe}(k)}{\varepsilon^{ring}_{(1)}(event)} \tag{5.7}$$

where

$$N(\beta, \theta_{part}) = \frac{\beta^2 n^2 - 1}{\beta^2 n^2 - \beta^2} \frac{\cos(\theta_{part})}{N_0} \tag{5.8}$$

Similarly, the expression describing charge calculation with the current LIP algorithm can be written as

$$Z^2_{(0)} = N^2(\beta, \theta_{part}) \frac{\sum_{k=1}^{N_{hits}} n^{(0)}_{pe}(k)}{\varepsilon^{ring}_{(0)}(event)} \tag{5.9}$$

On the other hand, since the charge is being reconstructed using the RICH detector, it can also be described by the ratio between detected and collected sinal at PMT/pixel matrix as follows:

$$Z^2_{(0)} = \frac{N^{det}_{pe}}{N^{exp(0)}_{pe}} \tag{5.10}$$

$$Z^2_{(1)} = \frac{N^{det}_{pe}}{N^{exp(1)}_{pe}} \tag{5.11}$$

Therefore, comparing 5.7 and 5.9 with 5.11 and 5.10, respectively, the ring signal is now described by the following expressions:

$$N_{pe}^{exp(0)} = N(\beta, \theta_{part})\varepsilon_{(0)}^{ring} \tag{5.12}$$

$$N_{pe}^{exp(1)} = N(\beta, \theta_{part})\varepsilon_{(1)}^{ring} \tag{5.13}$$

Combining expressions 5.12 and 5.13, the RICH charge expression, after applying the Cherenkov polarization factor, is given by:

$$Z_{(1)}^2 = Z_{(0)}^2 \frac{\varepsilon_{(0)}^{ring}}{\varepsilon_{(1)}^{ring}} \tag{5.14}$$

In the next section, charge reconstruction will be performed, using RICH/AMS-02

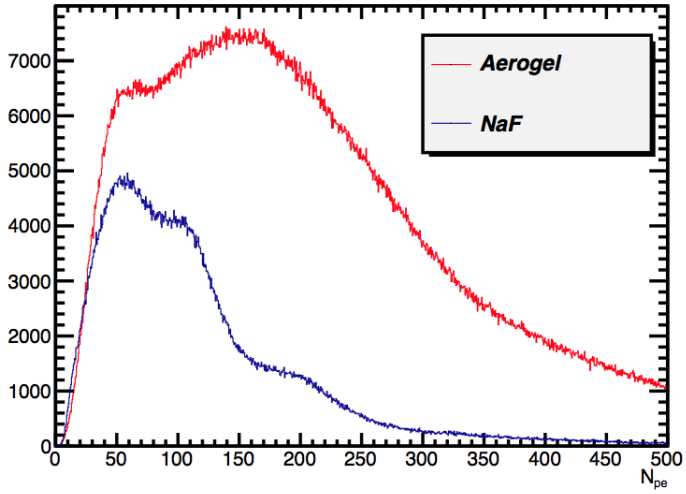

Figure 5.1: Ring signal for aerogel and NaF events.

data. Before taking this step, there are two fundamental concepts about the correction type applied by the LIP algorithm that should be addressed:

- *Time-indepedent corrections*;
- *Time-dependent corrections*.

Time-independent corrections include the following contributions:

- Efficiency and gain correction factor for each PMT;
- LIP efficiency corrections as function of pixel type and of photon incidence angles;
- *Cherenkov polarization correction*.

On the other hand, time-dependent corrections include the following effects:

- Efficiency and gain correction factors for each PMT/run. In further detail, the PMT gain decreases as temperature increases (LIP estimate: ring signal is reduced by 0.8%-0.9% per ^0C).

5.2.2 Charge reconstruction results

From the $\sim 15.8 \times 10^6$ aerogel events in the reconstructed data sample, $\sim 3.74 \times 10^6$ events (23.7%) passed all quality cuts (see appendix C) and were therefore considered for the final data quality evaluation.
From the resulting RICH selected data, it is possible to obtain charge spectrum according to the expression (5.14). Although, in order to study the charge resolution bias resulting from Cherenkov polarization effect, it is required to isolate the charge distribution peaks. However, due to RICH's geometry and design there are some loss factors (see chapter 3), which leads to a larger charge peak and there is a partial overlap for charges greater 1. For this reason, an external charge selection is required to isolate RICH charge peaks and to obtain the RICH's charge resolution.
Since the AMS-02 Tracker sub-detector provides a good charge resolution (from figure 5.2(b) follows that:$\frac{\sigma_{Z_{tracker}}}{Z_{tracker}} \simeq 2\%$), it was choosen to help separating RICH's reconstructed charge peaks.
The next step is, then, obtaining the correlation between $Z_{tracker}$ and RICH's reconstructed charge Z_{RICH} (see figure 5.2(a)). The two dimensional distribution $Z_{tracker} versus Z_{RICH}$ allows to perform a selection of RICH charge peaks (see figure 5.4), using tracker charge within the range $[Z_{tracker} - 0.4, Z_{tracker} + 0.4]$. After obtaining the reconstructed RICH charge peaks, the charge uncertainty measurement, given by the distribution width (σ_Z), should be obtained. The first half of the process includes shifting the charge peak center through a distinct scale factor for aerogel and NaF events (see figure 5.3). Afterwards, a double Gaussian fit was performed for each Z_{RICH} peak distribution for aerogel events (since the charge resolution is better than NaF events), which is illustrated in figure 5.4. On the other hand, the reconstruction of RICH charge algorithm (see chapter 3) has been improving charge resolution, i.e., reduce the systematic error resulting from the detector (in the next subsection there will be a further description of this feature) through several corrections (e.g. LG detection). Adding to this, it follows the final goals of this master thesis: study Cherenkov polarization bias on the LIP/RICH charge reconstruction, as described in subsection 5.2.1.

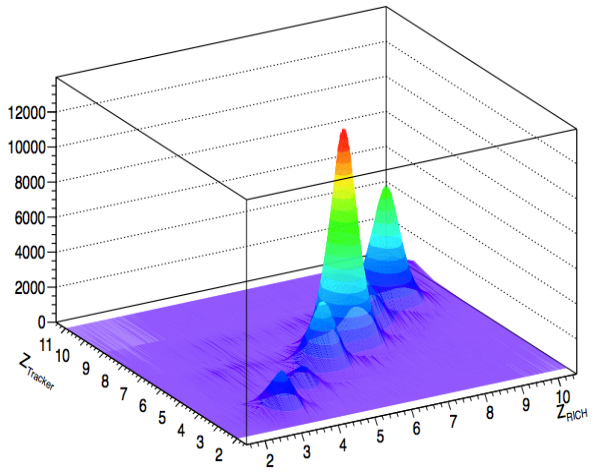

(a)

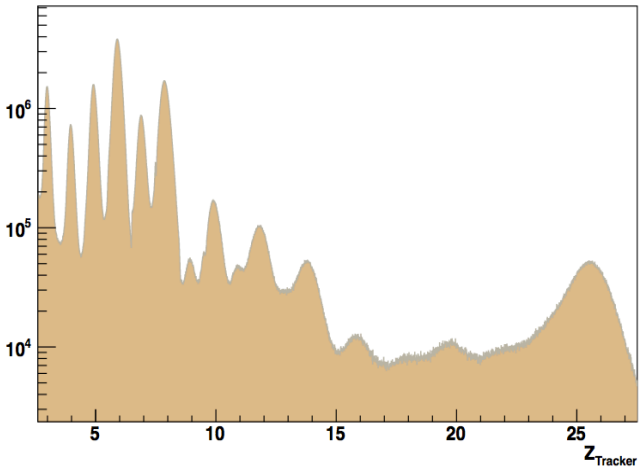

(b)

Figure 5.2: a)Tracker charge ($Z_{tracker}$) Vs RICH reconstructed charge (Z_{RICH}) for aerogel events. b) Charge spectra resulting from AMS-02/Tracker sub-detector.

5.2.3 Charge reconstruction results: fitting parameters

Since the σ_Z can already be obtained, the next step is finding the dependence on the particle's expected charge. In further detail, if there were any energy losses or absorption during the Cherenkov photons propagation through RICH detector, then the total charge error σ_Z would be only constrainted by the fraction of photons being detected, i.e., it would be a statistical problem ($\sigma_Z \simeq \sigma_Z^{stat}$). Although, the RICH detector, as any other Cherenkov radiation detector, it has some uncertainties, which will constrain the charge Z measurements (so-called systematic errors), described as follows:

- non-uniformities at the radiator level from spatial variations in the refractive

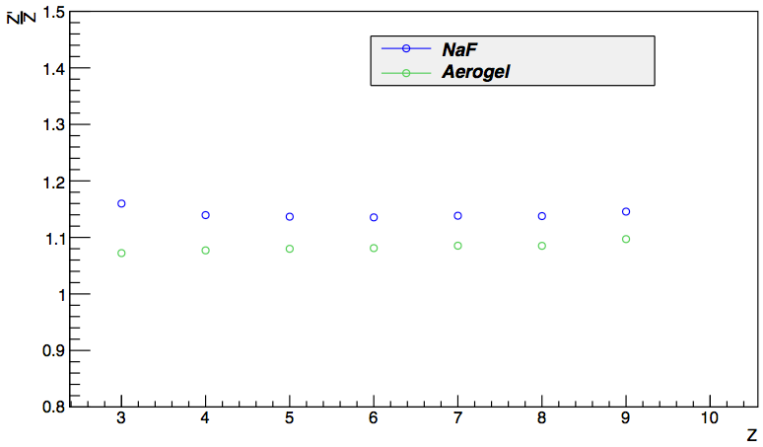

Figure 5.3: Ratio between mean charge value for each RICH charge peak (Z') and expected charge Z.

index, tile thickness and clarity;

- non-uniformity in photon detection efficiency, which is represented as a global factor evaluated mainly by the PMT gain variation due to temperature effects.
- non-uniformity in the LG properties (e.g: material, geometry, etc) and the optical coupling between LG and PMT;
- non-uniformity in the mirror coating that leads to different reflectivities from point to point;
- intrinsic photon properties (e.g. Cherenkov polarization).

Therefore, the charge measurement total error σ_Z is described by two distinct terms:

- the statistical term which is independent of the electric charge and depends essentially on the Cherenkov signal detected for singly charged particles (N_0) and on the resolution of the single photo-electron σ_{pe};
- the systematic which term increases with Z and dominates for higher charges.

Thereby, expanding the total error σ_Z in statistical (σ_Z^{stat}) and systematic error (σ_Z^{sys}), it follows then [13]:

$$\sigma_Z = \frac{1}{2}\sqrt{(\sigma_Z^{stat})^2 + (\sigma_Z^{sys})^2 Z^2} \tag{5.15}$$

In further detail, expression 5.15 can be written as [13]:

$$\sigma_Z = \frac{1}{2}\sqrt{\frac{1+\sigma_{pe}}{N_0} + \left(\frac{\delta N}{N}\right)^2 Z^2} \tag{5.16}$$

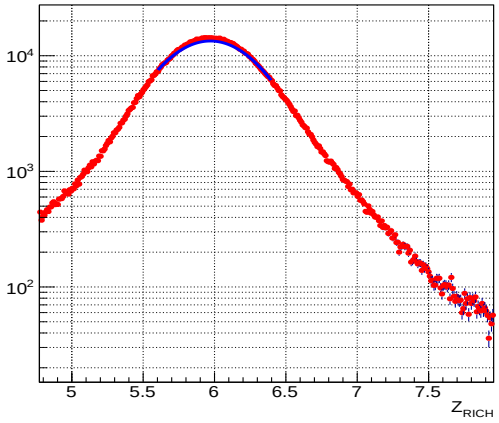

(a)

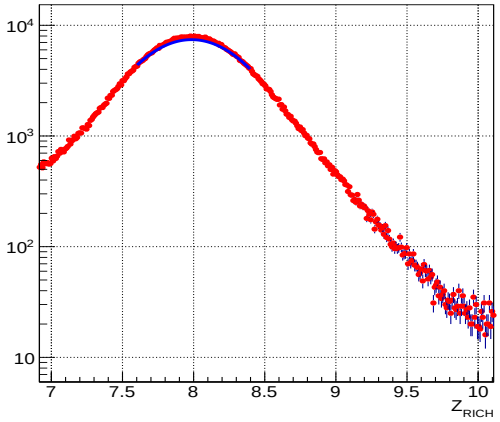

(b)

Figure 5.4: a) Distribution of RICH $Z = 6$ (carbon) charge peak for aerogel events. b) Distribution of RICH $Z = 8$ (oxygen) charge peak for aerogel events.

From the expression (5.16), the fit function is obtained for Aerogel and NaF events, respectively. The resulting parameters describe the *systematic error* and *statistical error*, as follows from tables extracted from reconstructed events generated in aerogel and in NaF with geometrical a geometrical acceptance greater than 0.4 and than 0.7 (5.1-5.4). Since the statistical error is easily minimized by the AMS statistic, the core of the RICH charge study will rely on *systematic error*. From this guideline, the analysis of systematic error for aerogel events can be described as follows:

- For the current LIP algorithm, geometrical acceptance is greater than 40%. Regarding this acceptance range, the systematic error, after applying the Cherenkov polarization effect, will suffer a small variation (see table 5.1), i.e., it is within

the range covered by the parameter error.

- On one hand, this could result from the contamination by low acceptance rings. On the other hand, the Cherenkov polarization effect increases with the number of photons per ring.

- The table 5.2 shows precisely a relative systematic error reduction $\sim 2\%$, for a geometrical acceptance greater than 70%.

From the previous considerations, one obvious conclusion can be extrapolated: the Cherenkov polarization effect is small in AMS charge data. The major variation was observed in NaF events for acceptance greater than 70%: $\sigma_Z^{sys} = 4.064\%$. Hence, these results do not match with the estimated effect using the Monte Carlo simulation.
The unexpected sm,all relevance of Cherenkov polarization in RICH charge reconstruction may be explained for the absorption by larger effects (e.g. ligh-guide losses). In further detail, the new light-efficiency calculation at pixel level may already be including inadvertently the Cherenkov polarization effect. In order to corroborate this hypothesis, a study about correlation between light-guide and Cherenkov polarization should be performed.

	Initial correction	Polarization correction	Final
σ_Z^{stat}	0.2864 ± 0.0013	0.2869 ± 0.0013	0.2869 ± 0.0013
σ_Z^{sys}(%)	2.503 ± 0.038	2.502 ± 0.040	2.502 ± 0.040

Table 5.1: Extrapolation of fitting parameters from $\sigma_Z(Z)$ plot (see figure 5.5(a)) for a geometrical acceptance > 0.40 (aerogel events).

	Initial correction	Polarization correction	Final
σ_Z^{stat}	0.2795 ± 0.0014	0.2792 ± 0.0015	0.2792 ± 0.0015
σ_Z^{sys}(%)	2.371 ± 0.045	2.323 ± 0.046	2.323 ± 0.046

Table 5.2: Extrapolation of fitting parameters from $\sigma_Z(Z)$ plot (see figure 5.6(a)) for a geometrical acceptance > 0.70 (aerogel events).

	Initial correction	Polarization correction	Final
σ_Z^{stat}	0.3734 ± 0.0078	0.3748 ± 0.0076	0.3748 ± 0.0076
σ_Z^{sys}(%)	4.197 ± 0.1723	4.070 ± 0.179	4.070 ± 0.179

Table 5.3: Extrapolation of fitting parameters from $\sigma_Z(Z)$ plot (see figure 5.5(b)) for a geometrical acceptance > 0.40 (NaF events).

	Initial correction	Polarization correction	Final
σ_Z^{stat}	0.3714 ± 0.0076	0.3749 ± 0.0075	0.3749 ± 0.0075
σ_Z^{sys}(%)	4.164 ± 0.176	4.064 ± 0.176	4.064 ± 0.176

Table 5.4: Extrapolation of fitting parameters from $\sigma_Z(Z)$ plot (see figure 5.6(b)) for a geometrical acceptance > 0.70 (NaF events).

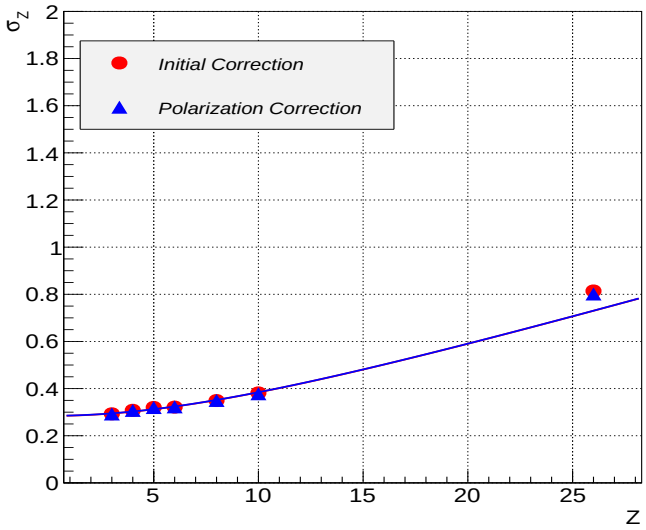

(a)

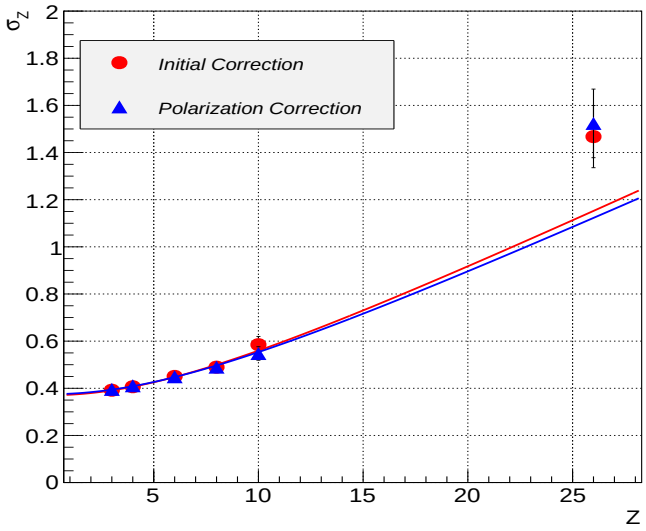

(b)

Figure 5.5: Results obtained for charge resolution σ_Z as function of particle charge Z before and after applying Cherenkov polarization. For aerogel events (a), points for $Z = 3, 4, 5, 6, 8, 10, 26$ were obtained. However, for NaF events (b) , only points $Z = 3, 4, 5, 6, 8, 10$ were obtained, since the resolution for $Z = 26$ has not a good performance. These results were obtained for a geometrical acceptance greater than 40%.

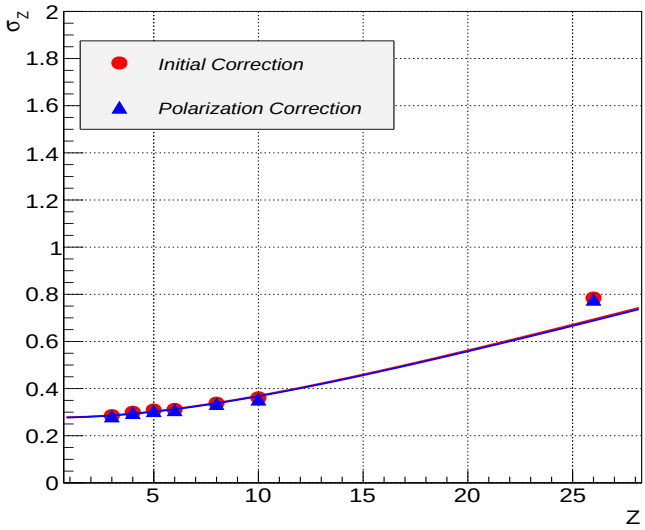

(a)

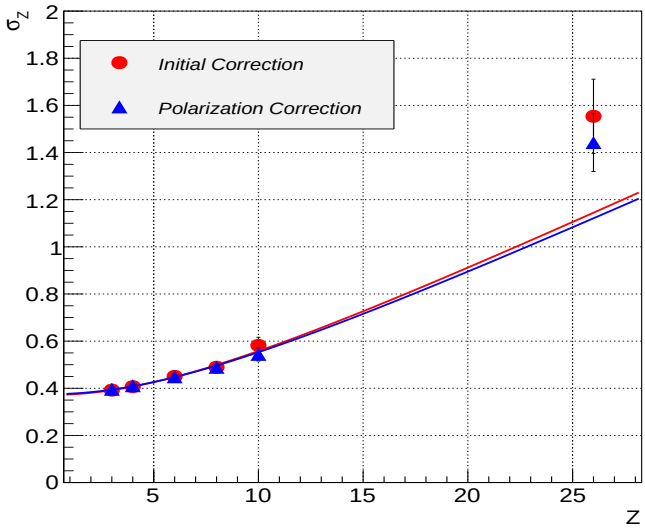

(b)

Figure 5.6: Results obtained for charge resolution σ_Z as function of particle charge Z before and after applying Cherenkov polarization. For aerogel events (a), points for $Z = 3, 4, 5, 6, 8, 10, 26$ were obtained. However, for NaF events (b) , only points $Z = 3, 4, 5, 6, 8, 10$ were obtained, since the resolution for $Z = 26$ has not a good performance. These results were obtained for a geometrical acceptance greater than 70%.

Bibliography

[1] T. Stanev, High Energy Cosmic Rays, Springer-Verlag (2004).

[2] M. S. Longhair, High Energy Astrophysics, Cambridge University Press (2011).

[3] Luísa Arruda,PhD Thesis:Charge and velocity reconstruction with the RICH detector of the AMS experiment (2008).

[4] M. Kachelrieß, Lecture Notes on High Energy Cosmic Rays, http://arxiv.org/abs/0801.4376v1 (2007).

[5] http://www.ams02.org/multimedia/

[6] Rui Pereira, PhD Thesis:Reconstruction methods and tests of the AMS RICH detector: Sensitivity to light isotope measurements and dark matter searches (2010)

[7] Elisa Lanciotti, Charge reconstruction with AMS-RICH, Internal Note- 2003-06.

[8] Rui Pereira, The RICH detector of the AMS-02 experiment: status and physics prospects, ICATPP (2007)

[9] Diego Casadei, PhD Thesis:Direct measurement of galactic cosmic ray fluxes with the orbital detector AMS-02 (2003)

[10] João Borges, Master Thesis:Velocity Reconstruction with the RICH detector of the AMS experiment (2003) IST

[11] Rui Pereira, Electric charge measurement with the AMS-02 RICH detector: reconstruction method and correction of systematics, Internal Note-2013-06.

[12] http://mathworld.wolfram.com

[13] Luísa Arruda, Fernando Barão and Rui Pereira, In-beam aerogel light yield characterization for the AMS RICH detector, Internal Note-2008-03.

[14] J.L. Contreras, I. de la Calle, J. Cortina, A study of the polarization of Cherenkov Radiation in Extensive Air Showers of Energy around 1 TeV.

[15] David J. Griffiths, Introduction to Electrodynamics,Prentice Hall (1999).

[16] Grant R. Fowles, Introduction to Modern Optics, Second Edition, Holt, Rinehart and Winston, Inc., pp. 164-168, 1975.

[17] Andrew S. Glassner, An Introduction to Ray Tracing , Academic Press Inc (1991).

[18] http://xray1.physics.sunysb.edu/ jacobsen/phy300f2008/l16.pdf

[19] Eugene Hecht, Optics, Third Edition, Addison Wesley (2002).

[20] http://www.graphics.cornell.edu/ westin/misc/fresnel.html

A

Cherenkov photon: Wave vector

Reflected wave

Figure A.1 shows a photon arriving at a planar interface and bouncing off.
The angle between the surface normal, marked $\vec{N}$, and the direction of the incident ray, marked $\vec{I}$, is called the *angle of incidence*, which is here denoted by θ_i. Given $\vec{N}$ and $\vec{I}$ the reflected ray $\vec{R}$ will easily follow.
There are two key physical laws that will be useful to find $\vec{R}$. The first is that the incident ray, the interface normal, and the reflected ray all lie in the same plane; thus the reflected ray is a linear combination of the incident ray and the normal. The second principle is that the angle of incidence is equal to the angle of reflection.
From these two laws, the following mathematical expressions can be written:

$$\vec{R} = \alpha_1 \vec{I} + \alpha_2 \vec{N} \tag{A.1}$$

$$\theta_i = \theta_r \tag{A.2}$$

From the observation of figure A.1 it is clear that $\cos(\theta_i) = -\vec{I} \cdot \vec{N}$. Regarding this, the relation $\cos(\theta_r) = \vec{N} \cdot \vec{R}$ is trivial. Rewriting the expression A.1 as:

$$\cos(\theta_i) = \cos(\theta_r) \tag{A.3}$$

$$-\vec{I} \cdot \vec{N} = \vec{N} \cdot (\alpha_1 \vec{I} + \alpha_2 \vec{N}) \tag{A.4}$$

$$= \alpha_1 \vec{N} \cdot \vec{I} + \alpha_2 \vec{N} \cdot \vec{N} \tag{A.5}$$

$$= \alpha_1 \vec{N} \cdot \vec{I} + \alpha_2 \tag{A.6}$$

The last expression results from $|\vec{N}|$=1 ($\vec{N} \cdot \vec{N} = 1$). Since the parameter α_1 can be chosen arbitrarily as 1, then it follows that

$$\beta = -2(\vec{N} \cdot \vec{I}) \tag{A.7}$$

Thus the complete formula for the direction of reflected ray is

$$\vec{R} = \vec{I} - 2(\vec{N} \cdot \vec{I}) \tag{A.8}$$

where

- $\vec{I}$ is the incident ray;
- $\vec{N}$ is the surface normal;
- $\vec{R}$ is the reflected ray.

In order to check that $\vec{R}$ is a unitary vector, it is necessary to confirm that $\vec{R} \cdot \vec{R} = 1$. Then,

$$\vec{R} \cdot \vec{R} = (\alpha_1 \vec{I} + \alpha_2 \vec{N}) \cdot (\alpha_1 \vec{I} + \alpha_2 \vec{N}) \tag{A.9}$$

$$= \alpha_1^2 + 2\alpha_1 \alpha_2 (\vec{I} \cdot \vec{N}) + \alpha_2^2 \tag{A.10}$$

$$= 1 + 2[-2(\vec{N} \cdot \vec{I})(\vec{N} \cdot \vec{I})] + [-2\vec{N} \cdot \vec{I}]^2 \tag{A.11}$$

$$= 1 \tag{A.12}$$

Finally, it is always necessary to check if incident and normal vectors $\vec{I}$ and $\vec{N}$ are normalized.

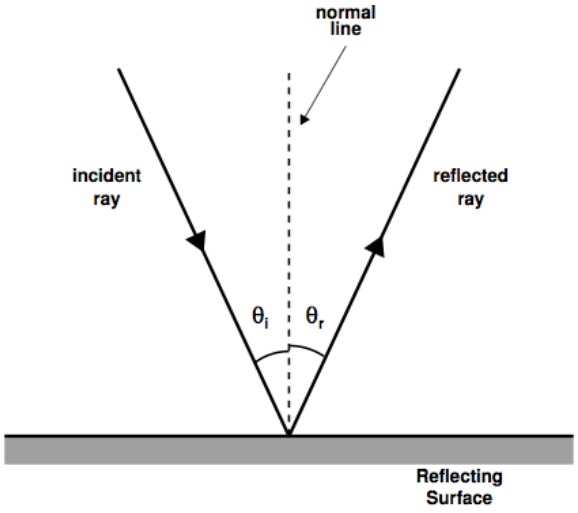

Figure A.1: The geometry of reflection.

Refracted wave

The formula for the transmitted ray can be derived with the help of figure A.2.

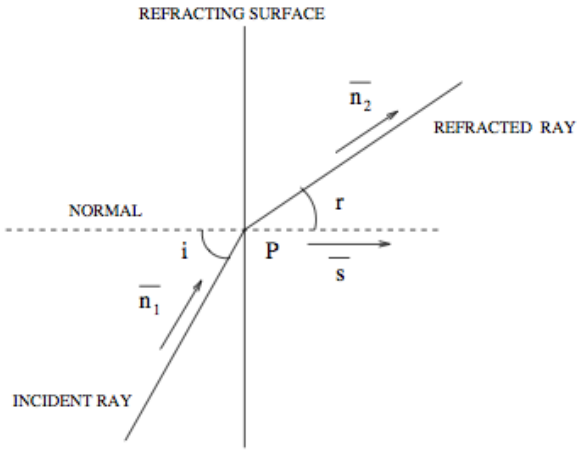

Figure A.2: The geometry of photon transmission.

The two underlying physical laws are that the transmitted ray is coplanar with the incident ray and the normal and Snell's Law.These laws are mathematically described respectively by:

$$\vec{T} = \beta_1 \vec{I} + \beta_2 \vec{N} \tag{A.13}$$

$$\frac{\sin\theta_t}{\sin\theta_i} = \frac{n_i}{n_t} \tag{A.14}$$

From expressions (A.13-A.14) and considering that $\vec{I}$ and $\vec{N}$ are unitary, it follows that

$$\vec{I}\cdot\vec{T} = \beta_1 + \beta_2(\vec{N}\cdot\vec{I}) \implies \cos(\theta_t - \theta i) = \beta_1 + \beta_2\cos(\pi - \theta_i) \tag{A.15}$$

$$\vec{T}\cdot\vec{N} = \beta_1(\vec{I}\cdot\vec{N}) + \beta_2 \implies \cos(\pi - \theta_t) = \beta_1\cos(\pi - \theta_i) + \beta_2 \tag{A.16}$$

Solving equations (A.15-A.16) for variables β_1 and β_2, it follows that

$$\beta_1 = \frac{\sin(\theta_t)}{\sin(\theta_i)} \tag{A.17}$$

$$\beta_2 = \frac{\sin(\theta_t - \theta_i)}{\sin(\theta_i)} \tag{A.18}$$

$$\tag{A.19}$$

Thus the final formula for $\vec{T}$ is

$$\vec{T} = \left[\frac{\sin(\theta_t)}{\sin(\theta_i)}\right]\vec{I} + \left[\frac{\sin(\theta_t - \theta_i)}{\sin(\theta_i)}\right]\vec{N} \tag{A.20}$$

B

Cherenkov polarization and Fresnel equations

Polarization

CK radiation is a plane electromagnetic wave, which means that both electric field $\vec{E}$ and magnetic field $\vec{B}$ are normal to the propagation direction $\vec{k}$. The CK

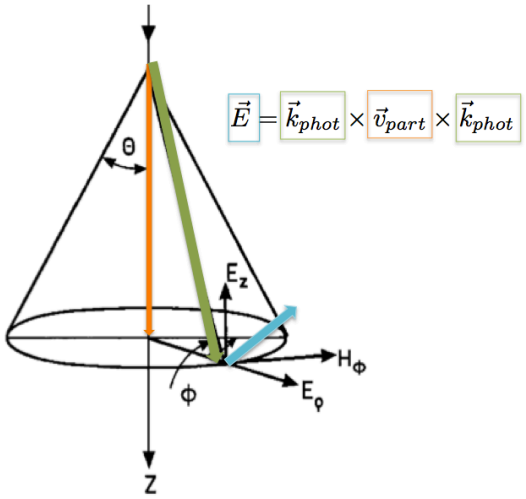

Figure B.1: CK light polarization vector. The electric vector $\vec{E}$ lies in the plane defined by the particle direction and the photon direction.

polarization vector is cointained in the plane defined by the particle's momentum vector and photon wave vector, as shown in figure B.2.
Even though there is a constraint in electric field direction, it can always be depicted more easily in a parallel ($\parallel$) and perpendicular ($\perp$) form, for which components are given by,

- $\vec{E}_\parallel$: electric field projection onto the plane of incidence
- $\vec{E}_\perp$: electric field projection onto the normal to the plane of incidence.

where it is implied that

$$\vec{E} = \vec{E}_\parallel + \vec{E}_\perp \tag{B.1}$$

On the other hand, following the conditions imposed by Maxwell's equations, electromagnetic fields can be described as scalar plane waves. Hence, the general expression for an electromagnetic wave follows

$$\vec{E}(\vec{x}, t) = \vec{E}_0 e^{(\vec{k}\cdot\vec{x} - wt)} \tag{B.2}$$

with the understanding that the true fields are the real parts of these complex expressions.
Therefore, using expression B.2 for the photon's incident, reflected and transmitted

electric fields terminology, it may be globally represented as,

$$\vec{E}_{\parallel}(\vec{x},t) = E_0 e^{(\vec{k}\cdot\vec{x}-wt)}\vec{e}_{\parallel} \tag{B.3}$$

$$\vec{E}_{\perp}(\vec{x},t) = E_0 e^{(\vec{k}\cdot\vec{x}-wt)}\vec{e}_{\perp} \tag{B.4}$$

These unitary vectors $\vec{e}_{\perp}$ and $\vec{e}_{\parallel}$ result from

$$\vec{e}_{\perp} = \vec{n}_{inter} \times \vec{k}_q \tag{B.5}$$

$$\vec{e}_{\parallel} = \vec{k}_q \times \vec{e}_{\perp} \tag{B.6}$$

where n_{inter} is a unitary vector normal to the dieletric interface and, k_q (q=reflected, refracted wave vector) is the photon's wave vector.
On the other hand, let the angle between $\vec{E}_q$ (q=incident, reflected, refracted wave vector) and the plane of incidence described by its surface normal (see equation B.5) be α_q. The polarization vector may then be rewritten as:

$$\vec{E}_q = E_q \sin(\alpha_q)\vec{e}_{\parallel} + E_q \cos(\alpha_q)\vec{e}_{\perp} \tag{B.7}$$

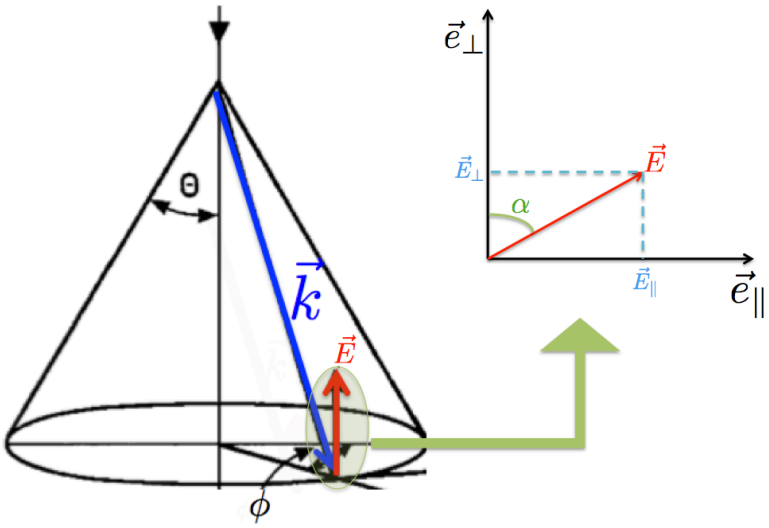

Figure B.2: Representation of Cherenkov polarization angle (α).

Fresnel equations

The continuity of the tangential electric field component through the dielectric boundary between the two media implies for all time *t* and photon intersection point

coordinates $\vec{r}$ that

$$\vec{n} \times \vec{E}_i + \vec{n} \times \vec{E}_r = \vec{n} \times \vec{E}_t \tag{B.8}$$

$$\implies \vec{n} \times \vec{E}_{0i} e^{(\vec{k}_i \cdot \vec{x} - wt)} + \vec{n} \times \vec{E}_{0r} e^{(\vec{k}_r \cdot \vec{x} - wt)} = \vec{n} \times \vec{E}_{0t} e^{(\vec{k}_t \cdot \vec{x} - wt)} \tag{B.9}$$

Assuming that wave amplitudes are constant and taking into account that expression B.9 is true over the entire surface and for all *t*, it follows that:

$$(\vec{k}_i \cdot \vec{x} - wt) = (\vec{k}_r \cdot \vec{x} - wt) = (\vec{k}_t \cdot \vec{x} - wt) \tag{B.10}$$

Applying the boundary conditions at the interface, whereas the components of both $\vec{E}$ and $\vec{B}$ are equal on both sides of the interface, the Fresnel coefficients for reflection and transmission follow:

$$r_{\parallel} \equiv \frac{E_{r\parallel}}{E_{i\parallel}} = \frac{n_2 \cos(\theta_i) - n_1 \cos(\theta_t)}{n_2 \cos(\theta_i) + n_1 \cos(\theta_t)} \tag{B.11}$$

$$r_{\perp} \equiv \frac{E_{r\perp}}{E_{i\perp}} = \frac{n_1 \cos(\theta_i) - n_2 \cos(\theta_t)}{n_1 \cos(\theta_i) + n_2 \cos(\theta_t)} \tag{B.12}$$

$$t_{\parallel} \equiv \frac{E_{t\parallel}}{E_{i\parallel}} = \frac{2n_1 \cos(\theta_i)}{n_2 \cos(\theta_i) + n_1 \cos(\theta_t)} \tag{B.13}$$

$$t_{\perp} \equiv \frac{E_{t\perp}}{E_{i\perp}} = \frac{2n_1 \cos(\theta_i)}{n_1 \cos(\theta_i) + n_2 \cos(\theta_t)} \tag{B.14}$$

C

Quality cuts

The main reason of quality cuts application over the events is a low systematic error. In further detail, having a clean data sample leads for some reason to exclusion of events linked with bad reconstructions. Under this assumption, the priority must be sample purity, not the total statistics.
Relying on previous studies, the quality cuts featured in this data sample are:

- Poor tracking paths reconstruction:
  The Cherenkov cone's axis depends on particle direction. Therefore, Cherenkov angle will also change according to particle direction. As a result, an inaccurate reconstruction of particle direction lead to an error increasing on RICH reconstruction.

- Limited ring visibility:
  A fraction of events falls outside the active area of detection matrix. This means that the detected portion of Cherenkov ring may be mistaken by noisy events (the signal of both are similar). There is not enough information to perform a good reconstruction.

- Clusters in RICH matrix:
  A basic physics phenomena resulting from the RICH matrix interaction with the charged particle leads to a strong signal. For instance, this problem happens either for high-Z events either several particles crossing the matrix. As a result, their strong signals will mislead the LIP velocity reconstruction, since it will hide the correct Cherenkov ring signal. In addition, when crossing particle 's signal is superimposed to the Cherenkov ring one, the charge reconstruction will be completely changed. On the other hand, the velocity reconstruction is well evaluated by LIP algorithm.

- Noisy pixels:
  Both bad calibration or malfunction in electronics are plausible reasons to noisy pixels. This results in unusual high signal of some isolated pixels. Lastly, the ring reconstruction will be affected (e.g. clusters), although in a minor scale.

- Shadow of poron walls:
  Particle hitting the radiator the edge of aerogel radiator tiles, emits the Cherenkov photon ring whereas a fraction of Cherenkov light will be lost due to the existance of opaque poron walls separation from its neighbours. As a consequence, the total collected signal will be reduced and the estimated charge will have a lower value.

Several quality cuts were applied to aerogel data samples in order to exclude bad reconstruction. In addition, their application was implemented only for charges $Z > 2$. There are also other selection cuts regarding geometry-base principles given by:

- **Ring Acceptance**
  Firstly, the accepted rings must have at least a 40% visible fraction. In further detail, this fraction was evaluated according to the fraction of Cherenkov photons falling inside the detection matrix area. This result may be weighted by a factor of 0.5, corresponding to the mirror reflection.
  On the other hand, a clear separation should be made between the following two concepts: eff_{acc} and acceptance. While eff_{acc} does not account the gaps between light-guides, acceptance is evaluated using the full area. As a result, a linear correlation could be performed over these two quantities as follows: $eff_{acc} \simeq (34/37)Acc$.

- **Distance of tile border**
  The LIP reconstruction method includes a radiator wall efficiency (eff_{wall}). Although, the difficulty to describe accurately the effect of poron walls lead to the following criteria construction: *exclude events with an estimated radiator impact point at a distancer smaller than 1 cm tile edge* (see figure C.2).

- **Kolmogorov probability for ring hits**
  Generally, Kolmogorov test: quantifies a distance between the empirical distribution function of the sample and the cumulative distribution function of the reference distribution, or between the empirical distribution functions of two samples.
  For instance, Kolmogorov test was applied to azimuthal distribution of ring hits by comparing with a uniform distribution (measured in the Cherenkov cone's frame of reference). Every event's position will be described by a P_{kolm} within a range between 0 and 1. Conversely, events with localized noise in the form of clusters will a concentration of similar hits, leading to $P_{kolm} = 0.1$. As a result, this cut is useful to exclude bad reconstruction due to clusters, with a criteria defined by: $P_{kolm} < 0.2$.

- **Barycentre distance**
  The supporting principle to apply this cust regards a non-uniformity in the position of Cherenkov ring signal barycentre. Normally, RICH ring have an elliptical shape or a crescent shape (if both direct and reflected components are significant). Therefore, barycenter distance (d_{bary}) is defined by the distance ring

barycentre and highest PMT signal ring hits (see figure C.5).
Consequently, a well reconstructed event by LIP algorithm contain the Cherenkov ring's barycenter falling well inside the ring perimeter (and far from ring hits (except for crescent ring hits). Conversely, rings dominated by a strong cluster signal will have their barycenter pushed towards their cluster, leading to unusually small barycentre distances (as shown in figure C.1).
From this considerations it was defined the following criteria: *excluding events with* $d_{bary} < 5cm$.

- **Cluster signal distribution assymetry**
  Despite of collected ring signal geographical arrangement, a self-sustained evidence is the unusual collected signal of Cherenkov ring hits by PMT. An excellent criteria is evaluating the asymmetry cluster's signal distribution within the ring (a_{clust}). More explicitly, this a quantity within a range from 0 to 1 and it is basically defined by the following expression:

$$a_{clust} = max(\Delta_1, \Delta_2, ..., \Delta_{N_{clust}}) \tag{C.1}$$

  where

$$\Delta_k = \frac{k}{N_{clust}} - \sum_{k=1}^{N_{clust}} n_{pe}^{PMT}(k) \tag{C.2}$$

  and clusters are numbered in ascending order of their signals, i.e., $n_{pe}^{PMT}(1) < n_{pe}^{PMT}(2) < ... < n_{pe}^{PMT}(N_{clust})$. This estimator is illustrated in figure C.3. For instance, the unusual high values of a_{clust} shows the existence of strong clusters. In conclusion, a typical range of a_{clust} paramter for well reconstructed events (for high Z values) is given by: $0.15 < a_{clust} < 0.50$.

- **Hit signal distribution asymmetry**
  Similarly to signal asymmetry estimator for PMTs, one could also be made at a pixel level as follows:

$$a_{hit} = max(\delta_1, \delta_2, ..., \delta_{N_{hits}}) \tag{C.3}$$

  where

$$\delta_k = \frac{k}{N_{hits}} - \sum_{k=1}^{N_{hits}} n_{pe}(k) \tag{C.4}$$

  and ring hits are also sorted: $n_{pe}(1) < n_{pe}(2) < ... < n_{pe}(N_{hits})$. This second estimator is illustrated in figure C.4. Although a_{hit} is close related with the previous one for PMTs, there are some specific features for each one. For instance, strong PMTs signal is a more efficient evidence about cluster-base estimator,

since it shows a clear high value even if pixel's signal doesn't tell it explicitly.
Therefore, the hit-type estimator is more suitable to describe noisy hits individually. Since estimator a_{hit} is more sensitive to smaller variations in hit-signal, some effects such delta-rays are more likely to be separated from photons ring signal.
Both cluster and hit asymmetry estimators are charge-dependent, increasing with particle charge.
Finally, from this careful study of the hit signal asymmetry estimator led to the choice of the following acceptable range: $0.30 < a_{hit} < 0.50$.

- Clusterization coefficient
  A new parameter will be introduced to measure, the clusterization factor *c* , so that the ring signal arrangement in clusters within a typical size of a PMT. However, the simple evidence of that noise existence is enough to discard the event.
  This new estimator will regard the number of clusters present in the ring. Although, it may occur that the number of clusters are distributed in a balanced way,which means the barycentre is in a "good" position.
  Furthermore, regarding that each cell size in the RICH matrix is 34X34 mm, this means that hits inside the same PMT are as far as a few cm. As a result, a given is part of a continuous ring from a high-Z particle or may be part of an isolated cluster, whereas it also surround by other similar hits (see figure C.6). There is, although, a difference between the two previous situations for larger distances:

  – In the first one, an isolated cluster will be surround by a number of others in its proximity, but a few for further distances;
  – Meanwhile, in the second situation there will be many more hits surrounding the ring;
  – This last feature helps to define the clusterization coefficient as ratio of total "observed" ring signal by ring hits to distances within a range [3,6] cm:

$$c = \frac{\sum\limits_{i,j(i\neq j, d_{ij}<3\,\mathrm{cm})}^{N_{hits}} n_{pe}(i)\, n_{pe}(j)}{\sum\limits_{i,j(i\neq j, d_{ij}<6\,\mathrm{cm})}^{N_{hits}} n_{pe}(i)\, n_{pe}(j)} \tag{C.5}$$

  Since the denominator may be zero, it was considered for computational reasons that c=-0.1 in those situations.

Considering an idealised good ring (a thin ring with uniform signal distribution), the signal will increase linearly with distance at first and a little faster as ring curvatures changes. Upon this, a typical average value of *c* should be therefore close to $0.5 = 3cm/6cm$ or a little lower, depending on two main source of fluctuations given by: statistical fluctuation component decreasing with Z; residual intrinsic fluctuation due to variations in event topology.
On the other hand, in events with isolated clusters only a small signal will be added when the association range increases from 3 cm to 6 cm, leading to values of *c* closer to 1. Conversely, if the matrix is very noisy (the ring is part of a more and less uniform "sea" of hits), the clusterization factor will increase quadratically, leading to a value closer to $0.25 = (3cm/6cm)^2$.
The analysis shows that, for good reconstructions, clusterization factor tends to fall in an increasily narrow interval centred at 0.5 as particle charge increases. In order to include a wide range of particle charges, the following range was selected: $0.30 < c < 0.60$

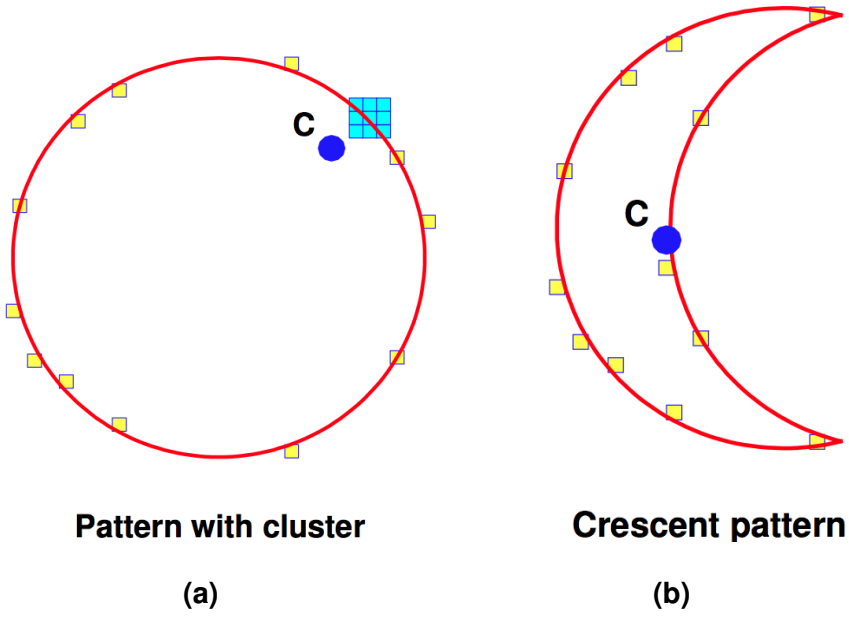

Figure C.1: Two types of events with barycentre C near the ring: noisy (bad) and crescent-shaped (good).

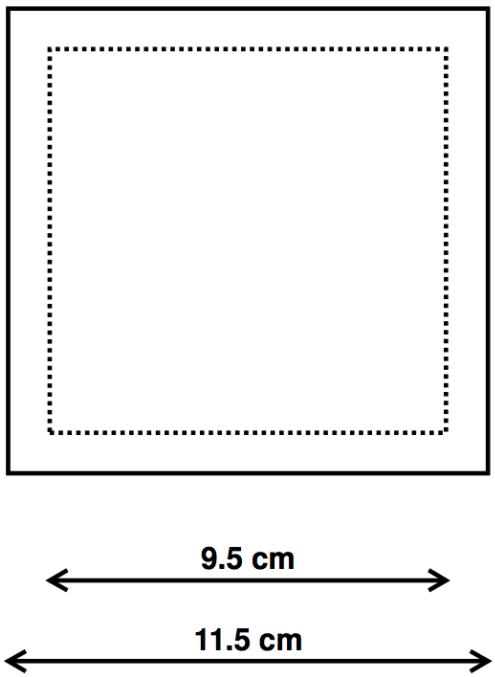

Figure C.2: Fiducial region (dashed square) used for aerogel tiles.

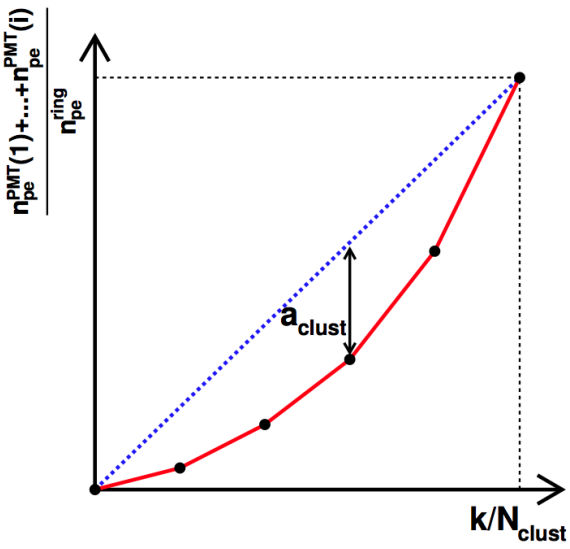

Figure C.3: Cluster signal distribution asymmetry.

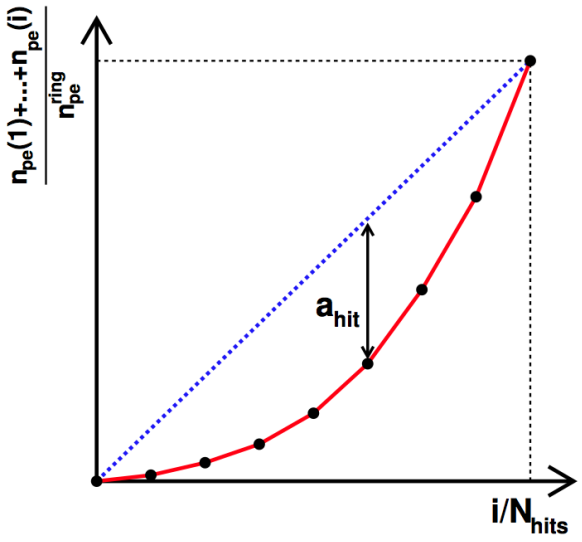

Figure C.4: Hit signal distribution asymmetry.

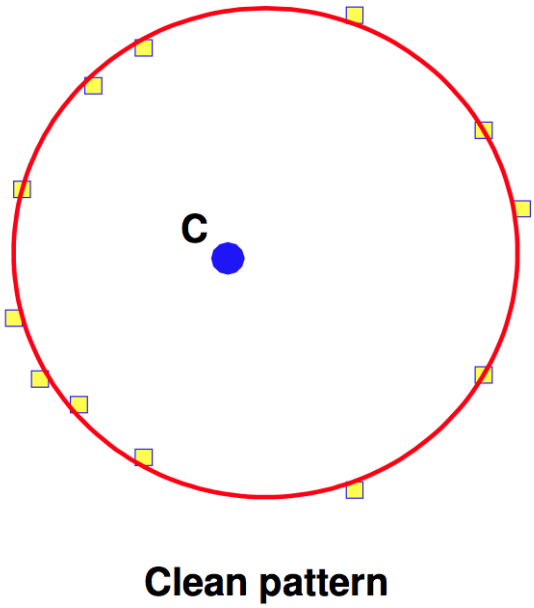

Figure C.5: Typical pattern for a good event with low Z: the signal's barycentre C is far from the ring.

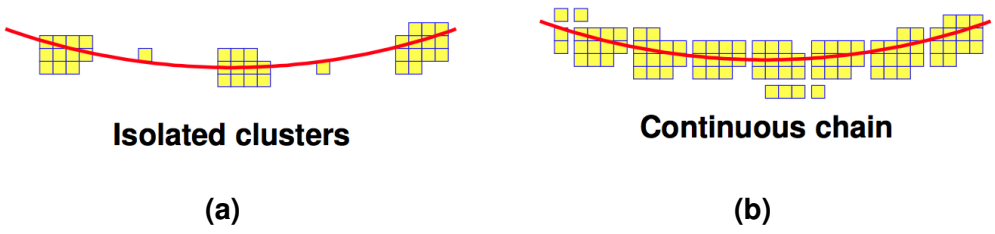

Figure C.6: Signal clusters in two contexts: isolated (noisy event) and grouped (good event with high charge).